**Recent Research on the Optimization of Interfacial Structure and Interfacial Interaction Mechanisms of Metal Matrix Composites: A Review**

*Zheng Zhong*[a,b], *Xiaosong Jiang*[a,b*], *Hongliang Sun*[a,b], *Zixuan Wu*[c], *Liu Yang*[d], *Adriana Matamoros-Veloza*[e*]

[a]Key Laboratory of Advanced Technologies of Materials, Ministry of Education, Chengdu 610031, China

[b]School of Materials Science and Engineering, Southwest Jiaotong University, Chengdu Sichuan 610031, China

[c]School of Engineering and Materials Science, Queen Mary University of London, London E1 4NS, United Kingdom

[d]Institute for Applied Materials (IAM-WK), Karlsruhe Institute of Technology (KIT), Karlsruhe 76131, Germany

[e]Faculty of Engineering and Physical Sciences, University of Leeds, Leeds, LS2 9JT, United Kingdom

*Corresponding author: xsjiang@swjtu.edu.cn (X.S. Jiang), Tel./Fax: +86-28-87634177; OR A.MatamorosVeloza@leeds.ac.uk (A. Matamoros-Veloza).

**Abstract**

Interfaces in metal matrix composites (MMCs) are crucial in determining the mechanical properties and functionality of MMCs. This paper reviews recent scientific advances and issues related to MMCs interfaces from four different perspectives: interfacial structural design, interfacial defect control, thermodynamics and kinetics of interfacial reactions, and interfacial microstructure-properties based numerical simulation. The influence of interfacial microstructural features on interfacial strength-toughness trade-offs and their functionality is given special attention. The interfacial problem is still one

of the main challenges to be solved in the composite system, which is mainly reflected in the following aspects: interfacial microstructure-deformation mechanisms in complex systems, precise control of interfacial defects and interfacial reaction products, and the efficient and cost-effective application of numerical simulation techniques. The integrated computation and intelligent design (artificial intelligence) of composites through multi-scale computational simulation with the guidance of "interface design-property prediction" will be the key area of MMCs interface research in the future.

**Keywords:** metal matrix composites, interface, numerical analysis, microstructural analysis

## 1. Introduction

Metal matrix composites (MMCs) are composites made of metals and their alloys that are artificially combined with one or several metallic or non-metallic reinforcing phases. They have a wide range of applications in aerospace, medical and other industrial fields.[1-6] Interfaces in MMCs are crucial in determining the mechanical properties and functionality of MMCs. Web of science Core Collection was selected as the data source, and the index was chosen as Science Citation Index Expanded (SCI-EXPANDED), and the indexed topics were “metal matrix composites” and “interface”, and the time span was the last 5 years, and a total of 701 journal articles were retrieved. The keyword visualization of the retrieved journal papers was carried out using VOSviewer (**Figure 1**),[7] and it was found that the main clusters included “metal matrix composites”, “mechanical properties”, “microstructure” and “interface”. In the research on interfaces of MMCs, the microstructure-mechanical properties relationship is still the main research direction, but the strategies for adjusting the microstructure are very different, and there is a lack of systematic collation of the latest advances (interfacial defect control, interfacial reaction thermodynamics/kinetics and numerical simulation techniques, etc.) in the interfacial research of MMCs.

The results of the above literature survey demonstrate the necessity and innovative nature of writing this review: both a summary review of recent advances in the classical research directions (microstructure-property relationships) of MMCs, and an overview and outlook of advances in novel research directions (e.g., multiscale numerical simulation and artificial intelligence, etc.).

The interface is not a simple geometrical surface but rather a transition region, so-called interfacial phase or the interfacial layer. This region is characterized by three main types of bonding; mechanical, infiltration and chemical bonding, making this region determinant for the mechanical properties and functionality of MMCs (**Figure 2**(a-c)).[8-10] Typically, these composites are designed to enhance the efficiency of load transfer, thermal and electrical transport,[11, 12] and for these purposes, several strategies need to be considered;[1, 13, 14] (1) inhibiting crack propagation,[15-17] (2) promoting the proliferation and annihilation of dislocations,[18] and (3) preventing localized stress concentration to reduce interfacial residual stresses.[6] Interfaces are critical in shaping the plastic deformation mechanisms of composites. These interfaces act as initiation points for various plastic deformation vectors such as dislocations, phase transition regions, twinning, and shear zones. They impede the movement of these vectors, and serve as prime locations for the accumulation, restructuring, and interaction of interfacial defects.[19] Interfaces with appropriate properties can significantly enhance the ability to absorb and eliminate defects,[20, 21] reducing the accumulation of damage during service (e.g., high temperature, high irradiation, high strain and other extreme environments).

One of the biggest drawbacks of conventional MMCs is the saturation of dislocation and stacking at the ceramic-metal interface which will lead to high stress concentration and plastic deformation instability. A well-designed interface structure can improve load transfer efficiency and eliminate stress

concentration. Recent studies have reported the development of MMCs with the incorporation of bimodal grains,[22, 23] nanotwins,[20, 24] gradient nanograins,[25, 26] lamellar structures,[19, 21, 27] and stacking faults[28, 29] to construct novel interfacial structures such as heterogeneous interfaces, core-shell interfaces, etc. This optimization of the interface structure improves the work-hardening rate and promotes stable and uniform plastic deformation of the material, which is also a common strategy to convert brittle materials into organic combined systems with superior strength-toughness balance.

Material mechanical behavior reflects underlying microstructural processes governed by crystalline defect activities. These include point defects, e.g., atomic vacancies and interstitials, line defects, e.g., slip dislocations, and planar defects, e.g., grain and interphase boundaries, stacking faults.[30] Interfaces can act as (1) sources of defects, (2) sinks for absorbing and annihilating defects, (3) barriers to defects, and (4) storage sites for defects.[31] When the material deforms, the initiation and interaction of these defects will greatly determine the mechanical properties of the material; therefore, the method design to improve material strengthening (e.g., controlling the generation of internal defects and their interaction) must be considered.

Effective load transfer in advanced MMCs requires high interfacial bonding strength. Interfacial bonding is usually influenced by three factors: interfacial chemistry, roughness, and residual stresses.[32-34] A technique to engineer interfacial chemistries consists in incorporating a secondary phase at the junction between the reinforcement and the matrix (Figure 2(d)), via interfacial reactions, to effectively transform weak Van der Waals interactions into robust chemical covalent or metallic bonds. However, excessive interfacial reaction produces numerous brittle phases, which directly damage or even severely deplete the reinforcement, leading to deterioration of the interfacial stability.[35] Equilibrium thermodynamics give us

a qualitative assessment of the directionality of interfacial reactions, the strength of the driving forces, and the speed of the transitions. Kinetics, on the other hand, delineate the rate of interfacial reactions influenced by physicochemical factors demonstrating the highly scientific and theoretical foundation required to design MMCs interfaces.

To gain deeper insights into the macroscopic mechanical properties of composites, quantification of the distribution of stress and strain at the interfacial scale is crucial. Interfacial microstructural features (e.g., composition, orientation, defects, and strain states, etc.) determine the properties of this region; however, they are extreme difficult to investigate using traditional experimental methods given their complexity. Density functional theory (DFT),[36-40] molecular dynamics (MD),[5, 18, 41-43] phase-field modeling (PFM),[44-47] finite element analysis (FEA),[48-51] deep learning (DL) [52-58] among other methods, help us to understand the fine microstructure and behavior at the interface region, efficiently and inexpensively.[59] Furthermore, these computational methods help us to improve the components of materials and processing techniques based on simulation predictions.

This paper will review the influence of complex interfacial microstructural features on MMCs strength-toughness trade-off and functionality from four perspectives; (1) interfacial structure design, (2) interfacial defect control, (3) interfacial reaction thermodynamics and kinetics, and (4) interfacial numerical simulation techniques. At the end this review, we summarized the latest progress of the research related to the optimization of interfacial structures and interfacial interaction mechanisms, and provided corresponding outlooks.

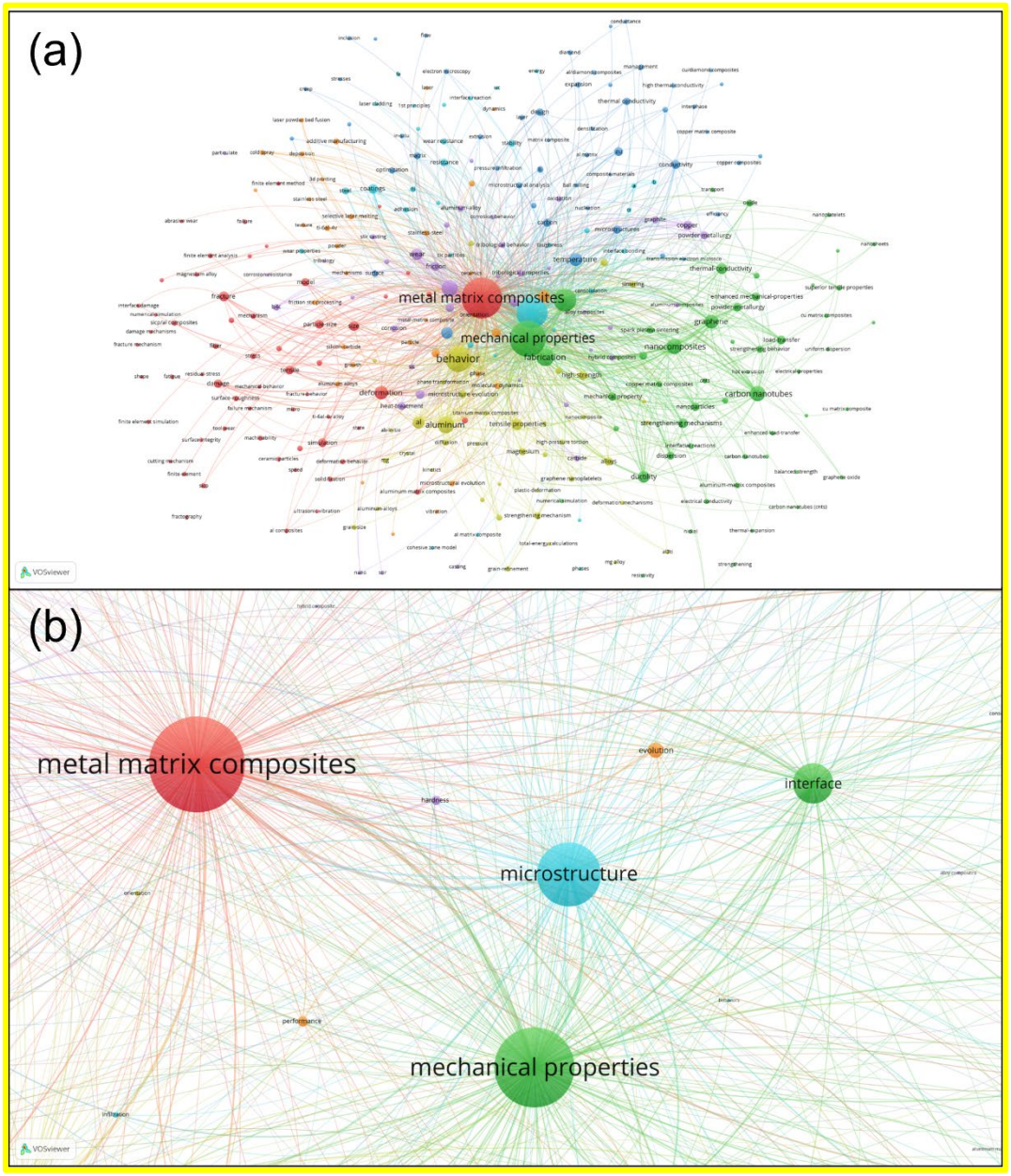


**Figure 1.** Keywords visualization of interfacial studies of MMCs.

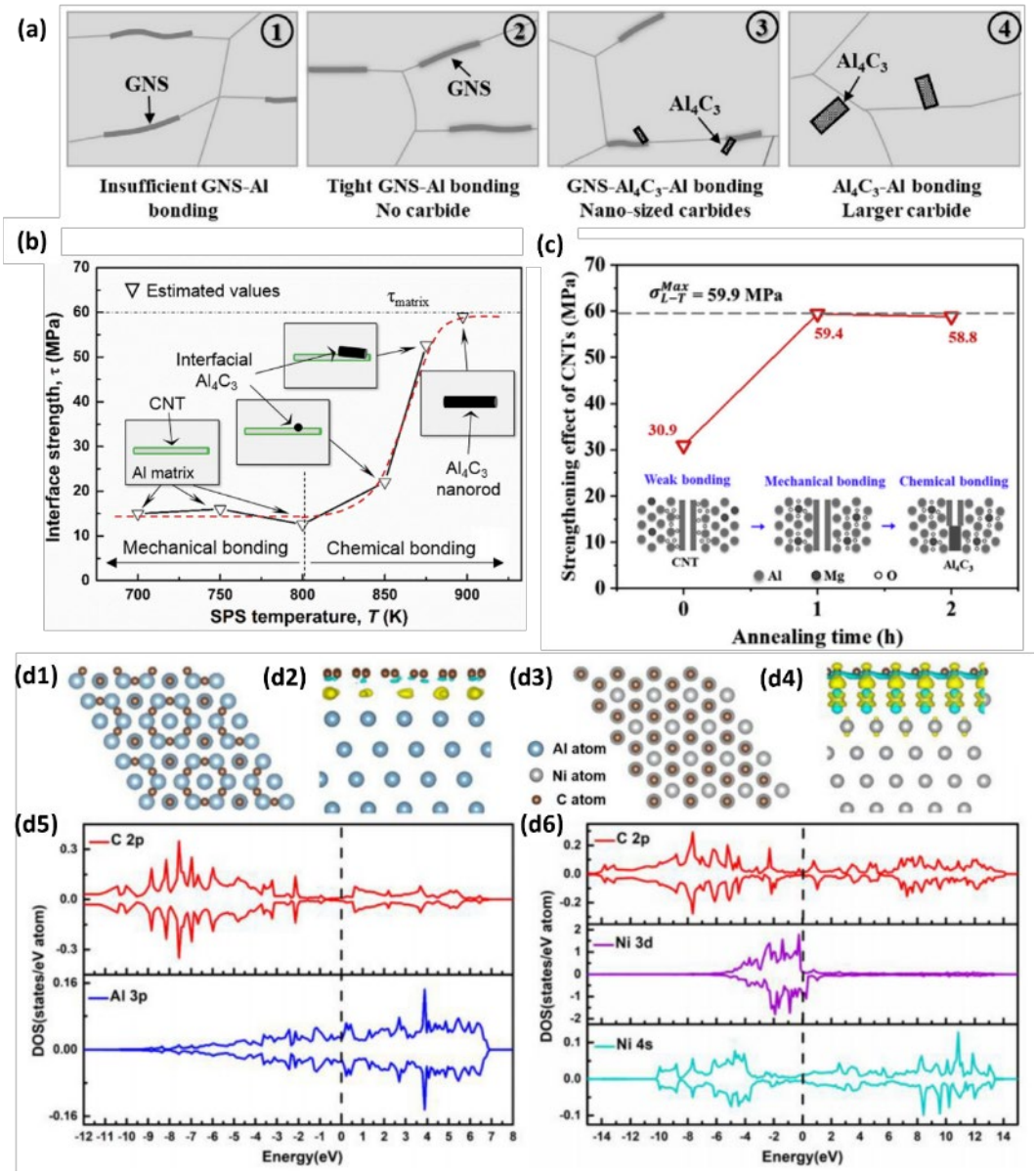


**Figure 2.** (a) Illustration of various interface states with interfacial reaction proceeding. Reproduced with permission.[8] Copyright 2020, Elsevier. (b) Dependence of interfacial strength on interfacial characteristics at various SPS temperatures. Reproduced with permission.[9] Copyright 2017, Elsevier. (c) Schematic diagram showing the evolution of CNT strengthening effect with different CNT/Al interfacial bonding conditions. Reproduced with permission.[10] Copyright 2019, Elsevier. (d) The top view with reference to energy minimized structures of (d1) Al-GN, (d3) Ni-GN; the differential charge density for interfaces of (d2) Al-GN and (d4) Ni- GN from the side view; the density of states of (d5) and (d6) for interfaces of Al-GN and Ni-GN, respectively. Reproduced with permission.[60] Copyright 2021, Elsevier.

## 2. Structural design

Failure initiation is a localized phenomenon. Primary failure mechanisms in MMCs encompass debonding at the reinforcement-matrix interface, void formation and strain localization within the matrix, and failure of the reinforcement itself.[61] Inclusions (e.g., particles, fibers, etc.) in the metal matrix are likely nucleation sites of microstructural damage. The aggregation of geometrically necessary dislocations (GNDs) near the interface can also have an impact on the failure process.[62] By designing novel interfacial structures like heterogeneous structure,[4, 26, 62, 63] multilayer structure,[5, 64, 65] stacking faults-assisted structure[6] et al. and modulating the interfacial deformation behavior, i.e., failure mechanism, in composites one can effectively improve the combined mechanical properties-functionality trade-off of MMCs.

### 2.1. Interface-mediated deformation behavior

#### 2.1.1. Flow strength

The flow strength of materials is defined by the stress needed to sustain nucleation, accretion, and extension of plastic deformation carriers, at a given strain rate, including dislocations and twins in crystalline materials, and shear transition zones in amorphous materials.[62] It is widely recognized that the flow stress in a material under loading (flow stress $\sigma_{flow}$ ) is divisible into two parts; (1) effective stress ($\sigma_{eff}$ ) and (2) back stress ($\sigma_b$ ).[19, 66-68] The contribution of back stress and dislocation hardening to the flow stress $\sigma_{flow}$ can be estimated by performing loading-unloading-reloading tests, known as the Bauschinger effect[66] (**Figure 3**). An in-depth understanding of stress evolution can help to characterize the intrinsic behavior of MMCs under deformation, such as the slip behavior of dislocations.[19]

The effective stress refers to the non-directional stress necessary for dislocations to overcome short-range barriers, such as lattice friction and dislocation forest, which can be expressed as:[67, 68]

$$\sigma_{eff} = \frac{(\sigma_{flow} - \sigma_u)}{2} + \frac{\sigma^*}{2} \quad (2\text{-}1)$$

where $\sigma_u$ denotes the unloaded yield stress, and $\sigma^*$ denotes the thermal part of the flow stress. Dislocation forests refer to dislocations on the secondary slip system that intersect the primary slip system which can be interpreted as another dislocation forests that cut through the primary slip surface. The presence of a dislocation forest can impede the motion of a dislocation, but if the stress is high enough, the sliding dislocations will cut through the dislocation forest and continue to move forward.[19] The process of dislocations cutting each other is so-called dislocation cross-cutting.

The back stress arises from the directional long-range internal stresses generated when GNDs are blocked by the domain boundary and stacked up.[68] This phenomenon has two main origins; intragranular, due to uneven distribution of dislocations manifesting as dislocation cells and walls; and intergranular, stemming from the differential plastic strain between hard and soft domains across heterogeneous interfaces, such as bimodal grain structures or the boundary between reinforcement and matrix, often linked to the Bauschinger effect.[62] The back stress $\sigma_b$ can be expressed as:[67, 68]

$$\sigma_b = \sigma_{flow} - \sigma_u \quad (2\text{-}2)$$

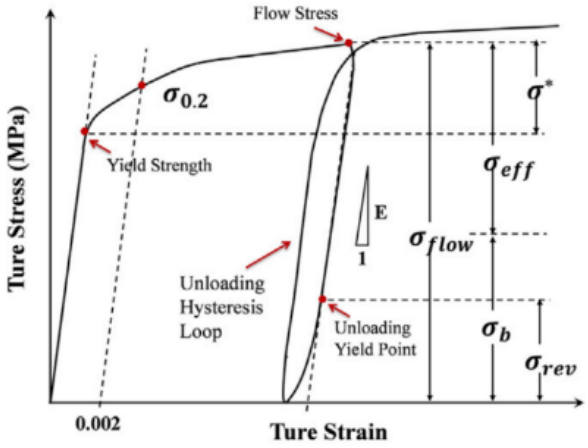


**Figure 3.** Schematic of hysteresis loops for characterizing the Bauschinger effect. Reproduced with permission.[66] Copyright 2019, Elsevier.

2.1.2. Strain hardening

During plastic deformation, the interaction between the interface and a multitude of dislocations plays a pivotal role. These dislocations may be accumulated at the interface, neutralized there, or travel across it. When dislocations travel across the interface, the discrepancy between the Burgers vectors of the incoming and outgoing dislocations results in the accumulation of residual dislocations at the interface.[6] Thus, dislocation-interface interaction can increase the density of external dislocations stored in the interface where the strain is applied. The persistence of this augmented external dislocation density might compromise the capacity of the interface to absorb future dislocations. It is conceivable that such a higher density could either impede the movement of subsequent dislocations, thereby obstructing their transit, or it could enhance the shear strength at the interface, thereby aiding the transfer of strain.[69-71] The mechanism of interfacial shear involves the initiation and movement of dislocations along the interface, a process determined by the atomic configuration of the lattice interface, which remains unaffected by the strength of interfacial shear. It has been shown that plasticity is limited by mutually

activated slip systems at 2D interfaces and leads to higher potential barriers associated with dislocation transport.[72] Through atomic-level simulations, it has been suggested that dislocations, resulting from lattice slips are trapped at weak interfaces due to shear forces and the broadening of dislocation cores within the interface (**Figure 4**).[69, 73] To shrinking these expanded cores and facilitate slip movement, it requires a reverse shear action. The weakness of an interface directly amplifies the expansion of dislocation cores, thus intensifying the obstruction to slip movement. This strain at two-dimensional interfaces makes them susceptible to crack formation, which triggers interface failure.[70] Such limitations give rise to stress accumulation and localized material flow within the composite, culminating in shear banding and restricting the capacity of the material for deformation.

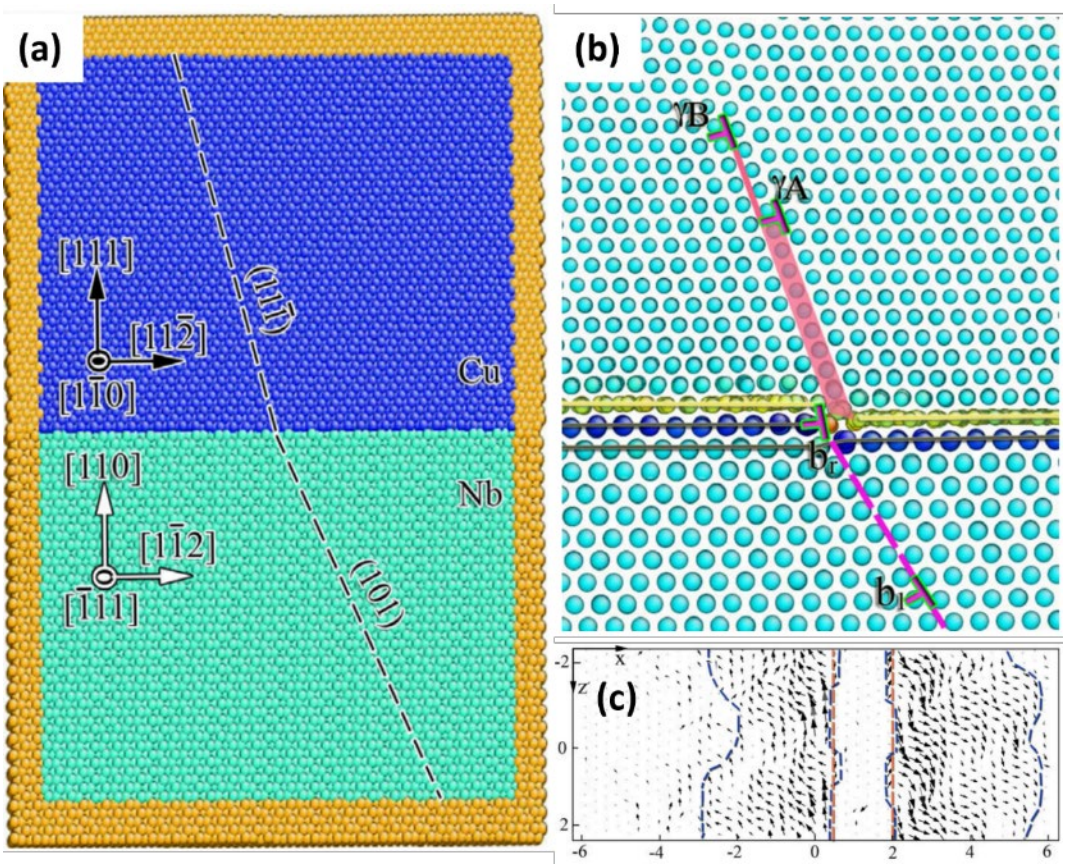


**Figure 4.** Atomistic modeling of the interaction of glide dislocations with "weak" interfaces. (a) Simulation cell of the rectangle bilayer. (b) Dissociation of a mixed dislocation in the Nb crystal (blue

atoms below) into the Cu crystal (cyan atoms above). (c) Patterns in the vector field plots of disregistry across the interface plane, showing core spreading when two identical edge Shockley partial dislocations with a separation of 1.55 nm enter the KS1 interface. Reproduced with permission.[73] Copyright 2008, Elsevier.

To deform a material, stress must be increased beyond the yield point, but the ability of the material to resist deformation increases after this point, a physical phenomenon known as strain hardening. High rates of work-hardening are essential for superior ductility. This facilitates uniform stretch by postponing local thinning (necking) under tensile stress. Strain hardening results from defects within the crystal structure, including dislocations, twinning, stacking faults, and in-between grains. These defect interactions significantly impact the microstructural evolution of the material under deformation. When the material is subjected to external forces, these crystal defects will deform increasing the deformation resistance of composites. **Figure 5** illustrates the impact of the graphene nanosheet GNS-Al interface on the deformation of GNS-Al composites via forest hardening and back stress hardening.[74] The storage process of dislocations at the GNS-Al interface induces forest hardening and back stress hardening.[62, 68] Forest hardening stems from non-directional, localized interactions among moving dislocations and the dislocation forest, impeding the progress of other dislocations along the operative slip planes; known as effective resistance. In contrast, back stress hardening is characterized by a directional extensive interaction between advancing dislocations and dislocations within the forest. This interaction prevents the original dislocation source from generating further dislocations by sharing identical Burgers vectors.[62] Collectively, both forest and back stress hardening mechanisms play pivotal roles in the process of strain hardening.

Under conditions of restricted plastic deformation, the escalation in dislocation density significantly

contributes to strain hardening. This phenomenon, known as dislocation strengthening, is quantified using Taylor's formula:[75]

$$\sigma = \alpha MGb\sqrt{\rho} \tag{2-3}$$

According to the Considère criterion, necking instability arises when the strain hardening rate falls beneath the true flow stress; therefore, enhancing the ductility of the material, requires a sufficiently high strain hardening rate to avert localized instability. The formula for calculating the strain hardening rate is provided below:[76]

$$\frac{d\sigma}{d\varepsilon} = \alpha MGb\frac{d\sqrt{\rho}}{d\varepsilon} \tag{2-4}$$

where $\rho = \rho_s + \rho_G$ is the total dislocation density, $\rho_s$ is the statistical storage dislocation density, $\rho_G$ is the GNDs density, $\alpha$ is a constant, $M$ is the Taylor factor, $G$ is the shear modulus, and $b$ is the magnitude of the Burgers vector. Hence, the rate at which materials undergo strain hardening is directly influenced by how fast dislocations accumulate during plastic deformation. Importantly, the rate of strain hardening is determined by the pace at which the dislocation density grows with increasing strain, rather than by the absolute dislocation density. In other words, a high dislocation density does not automatically translate to a high rate of strain hardening. High dislocation density at the beginning of deformation is harmful to the plasticity of composites. A typical example is that although cold-worked metals have high dislocation densities due to the existence of a saturating concentration of dislocation densities, lower rates of dislocation accumulation result in a tendency to lower work-hardening rates and plasticity.

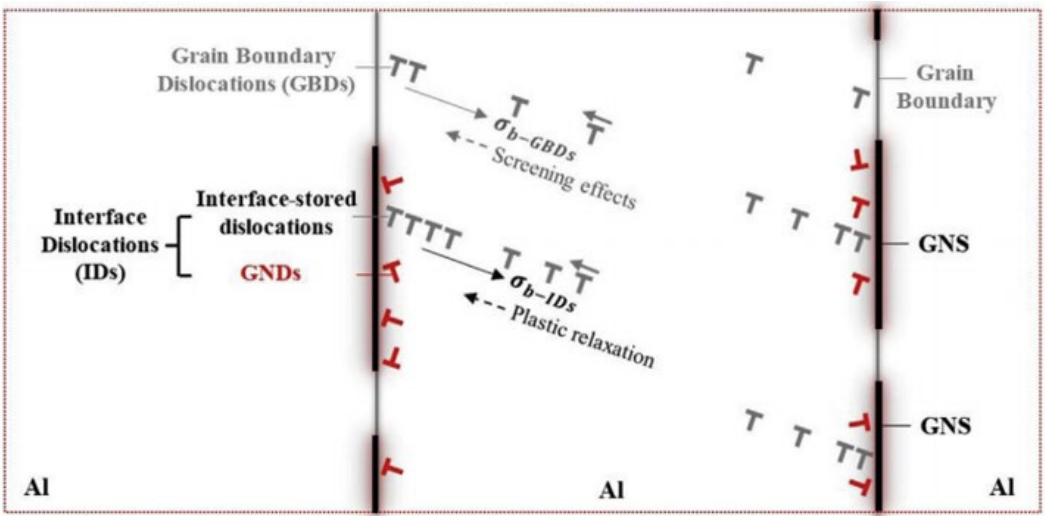


**Figure 5.** Illustration of the origin of forest hardening and back stress hardening induced by GNS-Al interface in GNS/Al composites. Reproduced with permission.[74] Copyright 2019, Elsevier.

2.2. Interface coherency

Interfaces are classified into coherent, semi-coherent, and incoherent types, depending on the level of the alignment in the atomic arrangement across the interface. A significant link exists between the strength of an interface and its coherency level, with coherent and semi-coherent interfaces having lower interfacial free energies and stronger interfacial bonding due to fewer bond breaks.[77] The B-terminal $Mg(Zn_{1.5}Cu_{0.5})/TiB_2$ interface has the highest $W_{ad}$ (3.8412 J/m$^2$) after the first-principle calculation[65] (**Figure 6**(a1-a3)). Although the calculated $W_{ad}$ depends on the type of interface end-face, the general trend is that the higher the coherency degree of interface, the higher the strength of interface. When the Cu atoms are polarized at the $Al/TiB_2$ interface to form the $Al/Mg(Zn_{1.5}Cu_{0.5})/TiB_2$ interface with higher coherency degree, it enhances the interfacial strength. The comparison of the TiC/Al and $TiB_2$/Al interfacial $W_{ad}$ is shown in Figure 6(b1), the average of the TiC/Al interface $W_{ad}$ (1.61 J/m$^2$) is significantly lower than that of the $TiB_2$/Al interface (2.77 J/m$^2$).[78] Enhanced interfacial compatibility, continuity, and greater work of adhesion contribute positively to the bond strength and stability

enhancement of the composite materials (Figure 6(b2)). The interfacial coherency degree affects the interfacial phonon-electron transport efficiency, and thus, the thermoelectric properties of the composites.[12] The coherent $\mathrm{Gr}/\{111\}_{\mathrm{Cu}}$ interface reduces lattice mismatch dislocations improving conductivity when compared to the semi-coherent $\mathrm{Gr}/\{100\}_{\mathrm{Cu}}$ interface[79] (Figure 6(c1-c3)).

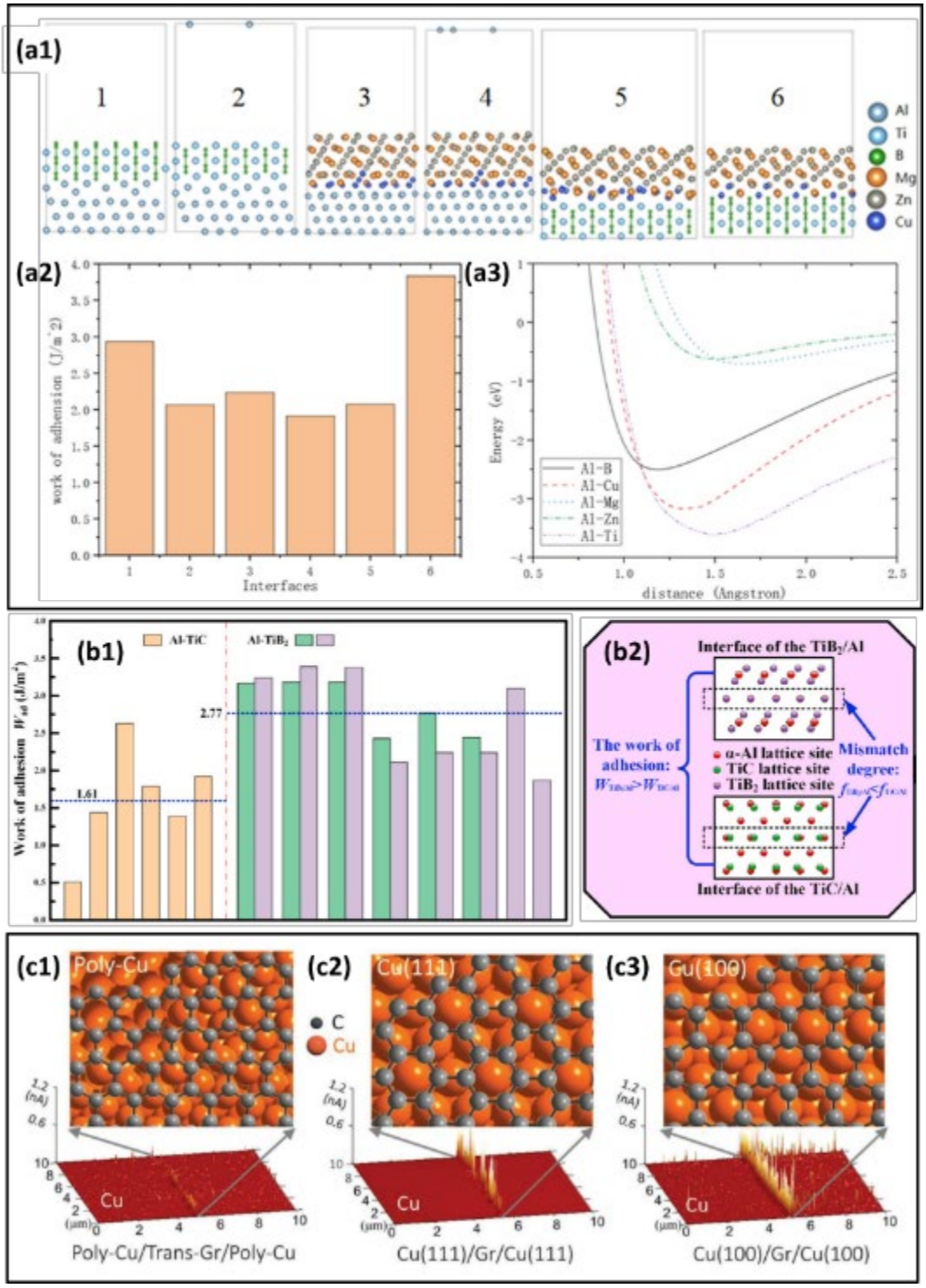


**Figure 6.** (a1) DFT relaxed interface models of the different $TiB_2$/Al and $TiB_2$/IP/Al interfaces (Case No. 1-6); (a2) calculated work of adhesion ($W_{ad}$) of case No. 1-6, and (a3) interaction between Al-X dimers. Reproduced with permission.[65] Copyright 2023, Elsevier. (b1) comparison of the adhesion work for the Al/TiC interfaces and the Al/$TiB_2$ interfaces;[78, 80-83] (b2) schematic diagram of interface bonding of the

TiC/Al and the $TiB_2$/Al. Reproduced with permission.[78] Copyright 2021, Elsevier. (c) A comparison of current flow along the interface area in Gr/Cu composites with different matrices. Reproduced with permission.[79] Copyright 2019, Wiley.

The mechanism of dislocation transport through the interface varies depending on the interface type (**Figure 7**[19]).[6, 30, 65, 84-86] Interfaces with higher mismatches exhibit lower interfacial atomic interactions and shear resistance than those with lower mismatches because the intersection of the mismatched dislocation can serve as a preferential location for interfacial dislocation loop formation. Consequently, the interface will shear in response to the stress field of adjacent lattice dislocations, thus attracting dislocations to the interface.[73, 87] Due to the inherent discontinuity in dislocation slip across a semi-coherent interface, after the incoming dislocations have been absorbed and expanded their cores within the interface, they can be transferred to other grains. Slip transport will involve dislocation re-nucleation and exit into the efferent slip system process, which is often difficult to occur because of the thermal activation required for this process.[19, 85] The core extension width increases with decreasing interfacial shear strength, and a weak shear interface with high mismatch will hinder dislocation transport across the interface. Dislocation slip systems have geometrical discontinuities at the interface due to lattice mismatches, and thus, the interface can hinder cross-interface transport of dislocations on both sides, which can have a strengthening effect.[4]

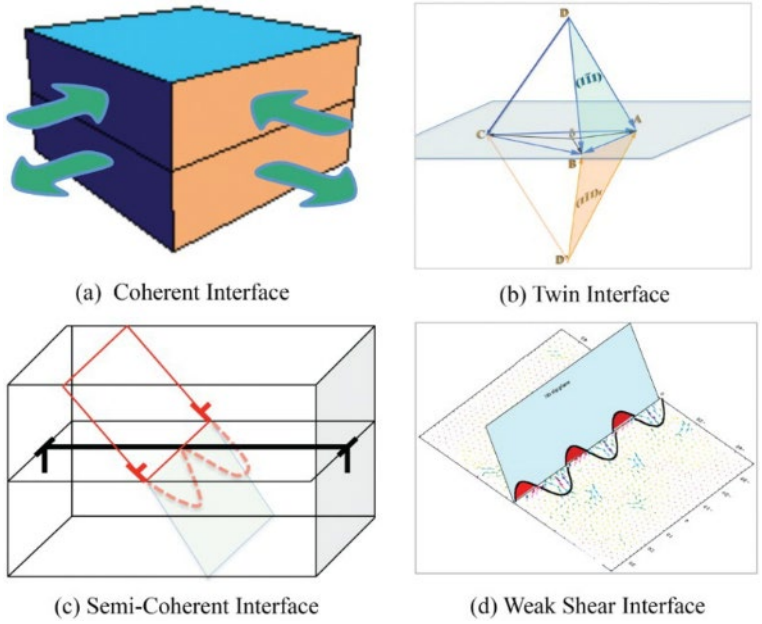


**Figure 7.** Schematic of key strengthening mechanisms in nanolaminates: (a) coherency stresses associated with lattice-matched nanolayers, (b) discontinuity of slip across twin interface, (c) glide dislocations pinned by grid of misfit dislocations at a semi-coherent interface, and (d) cross-slip of lattice dislocation in the weak shear interface. Reproduced under terms of the CC-BY license.[19] Copyright 2016, J. Wang, Q. Zhou, S. Shao, A. Misra, published by Taylor & Francis.

Peng et al.[88] argued that the ability of heterogeneous interfaces with a good coherency to coordinate plastic deformation by releasing dislocations, increases with the transverse size of the interface. This is attributed to the small amount of strain required to trigger dislocation nucleation. Zhang et al.[6] found that due to the high coherency at the MAX/Cu interface and the relatively low critical resolved shear stress (CRSS), favoring the formation of basal slip and SFs, the semi-coherent structure of the MAX/Cu interface combined with the pliable characteristics of MAX nanosheets facilitate the dislocation nucleation at the interface under shear strength induced by plastic deformation. This process also leads to the emergence of lattice defects, like partial dislocations alleviating the mismatch strains near the interface. Consequently, differing from traditional rigid ceramic reinforcements such as $Al_2O_3$ and $SiO_2$, the flexibility of MAX-phase nanocrystals results in a swift dislocation-relaxation around the interface

instead of generating a high density induced GNDs elsewhere.

Although weak shear interfaces with high mismatch tend to impede the trans-interface transport of dislocations causing dislocation stacking, if there are suitable slip coefficients at the two sides of the interface, the same can facilitate the re-nucleation and transport of dislocations. For example, Liu et al.[4] found that although $Ti_2AlC(1\bar{1}0\bar{3})$/TiAl$(111)$ semi-coherent interface hinders dislocation-expansion between $Ti_2AlC$ and TiAl substrates, due to the presence of $Ti_2AlC(0001)\langle 1\bar{1}00\rangle$ and TiAl$\{\bar{1}1\bar{1}\}\langle\bar{1}12\rangle$ slip systems on both sides of the interface, once dislocations nucleate in the mismatched region of the interface, they easily expand along these two slip systems. This helps to achieve the co-plastic deformation between the $Ti_2AlC$ and TiAl matrix. Therefore, different interfacial coherency will have different effects on dislocation storage and transport, and the same interfacial coherency (e.g., semi-coherent interface) will have different effects in different interfacial systems.

### 2.3. Heterogeneous structure

Due to the high brittleness, irregular shape of ceramic particles, and the incompatibility of the ceramic-metal interface, sliding dislocations are easily captured by ceramic nanoparticles during plastic deformation and build up at the high-mismatch interface.[19] Since these stacked dislocations will not be recovered and are difficult to move, the dislocations at the interface will saturate rapidly resulting in stress concentrations. The rise of novel nanocrystalline materials has provided new ideas to address the trade-off between strength and plasticity in MMCs, and some successful strategies have been applied in the synthesis of MMCs. Nanocrystalline materials used in the preparation of MMCs include bimodal grains,[22, 23] gradient nanograins,[25, 26] lamellar structures[19, 21, 27] (**Figure 8**), etc. They are used to increase the work-hardening rate as they yield heterogeneous interfaces, which leads to a stable and uniform plastic deformation of the material. It is worth noting that the heterogeneous interfaces here are not simply interfaces between two phases with different microstructures (e.g., ceramic-metal interfaces in

conventional particle reinforced MMCs (PRMMCs)), but interfaces capable of generating significant heterogeneous deformation-induced (HDI) stresses during deformation to produce HDI strengthening and strain hardening.[62]

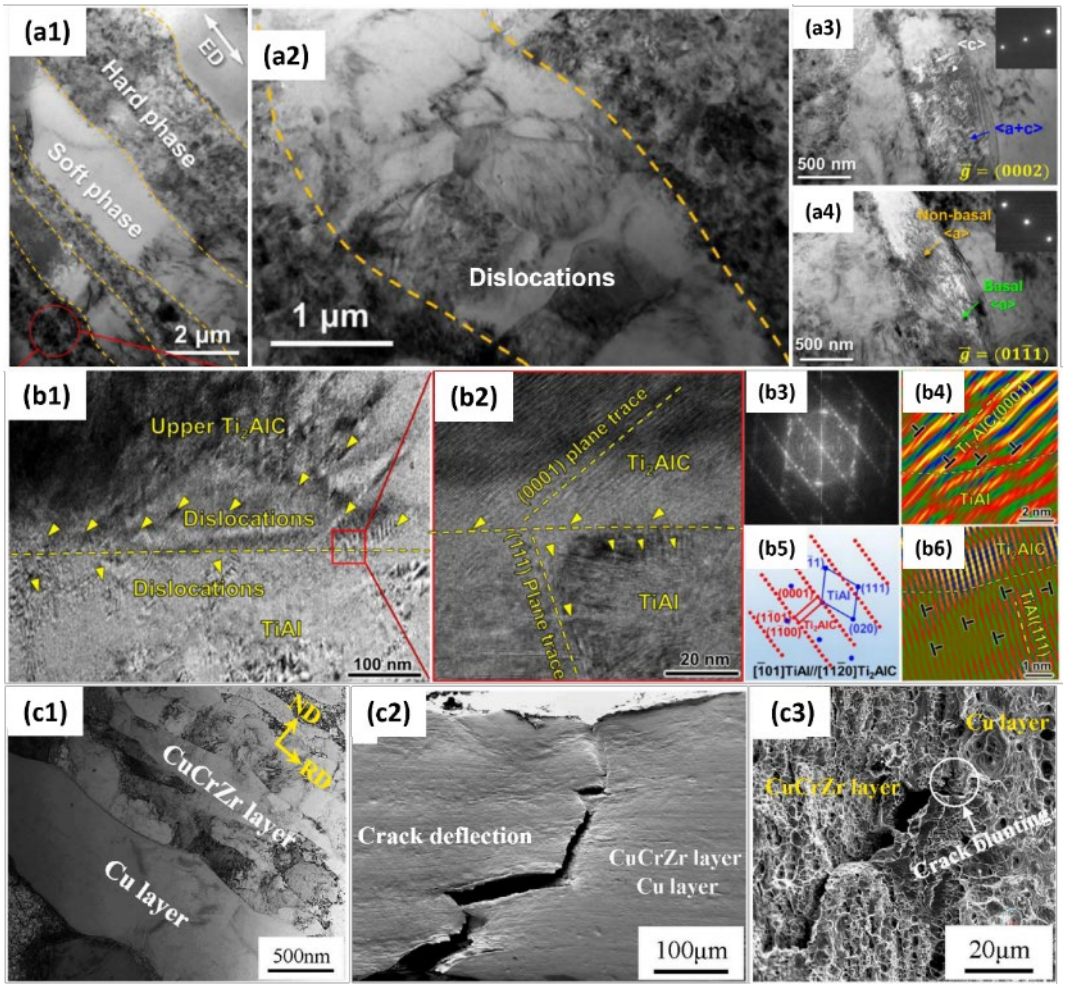


**Figure 8.** Some typical heterogeneous interfaces in MMCs. (a1) Representative TEM image showing a heterogeneous grain structure in an inverse nacre structured magnesium matrix nanocomposite; (a2) A high density of dislocations inside soft phase grains; (a3, a4) Non-basal <a> and pyramidal <c + a> dislocations were sufficiently activated in the soft phase. Reproduced with permission.[16] Copyright 2022, Elsevier. (b1) Heterogeneous interface in $Ti_2AlC$/TiAl composite; (b2) HRTEM image of interface; (b3-b6) Supplementary information for Figure 7(b2). Reproduced with permission.[4] Copyright 2023, Elsevier. (c1) Gradient heterogeneous interface in CuCrZr/Cu composites; (c2) Tensile fracture cross section of layered CuCrZr/Cu composites; (c3) Tensile fracture morphology at the gradient heterogeneous interface. Reproduced with permission.[26] Copyright 2023, Elsevier.

In MMCs with heterogeneous structures, the stacking of dislocations with the same Burgers vector at the heterogeneous interfaces leads to the superposition of stress fields on each other. This prevents the release of further dislocations from the (Frank-Read dislocation) source showing a gradient distribution of GNDs near the heterogeneous interfaces (**Figure 9**). The gradient distribution of dislocation density plays a role in regulating the strain gradient, since plastic deformation needs to occur by a dislocation slip,[89] thus effectively avoiding the stress concentration at the heterogeneous interface. In addition to this, as a typical class of two-dimensional defects, heterogeneous interfaces in metals have been used to improve interfacial stability in extreme environments,[21] thermal/electrical conductivity[21, 90] and coercivity[91] etc.

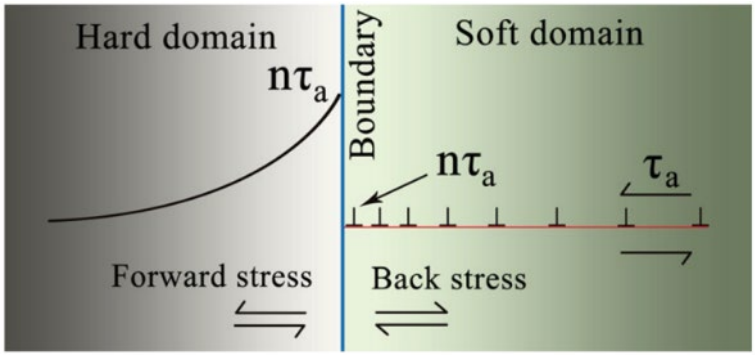


**Figure 9.** Schematics of a GND pile-up, inducing back stress in the soft domain, which in turn induces forward stress in the hard domain. Reproduced under terms of the CC-BY license.[89] Copyright 2019, Y. Zhu, X. Wu, published by Taylor & Francis.

### 2.3.1. Coordinating deformation

Non-uniform deformation in MMCs, caused by significant differences in flow stresses, leads to the accumulation of GNDs near the heterogeneous interface in the softer region. This accumulation generates a back stress in the softer zone and a corresponding forward stress in the harder zone. The interaction between these two stresses forms high-density GNDs. HDI strengthening contributes to an increase in yield strength, whereas HDI strain hardening aids in preserving and potentially enhancing the ductility of

the material.[25, 62] Since the presence of positive stresses weakens the hard zone to a certain extent, the nature of the hard zone greatly affects the strengthening effect of heterogeneous interfaces. If the hard zone is weaker than the soft zone, their interface is similar to a conventional homogeneous interface. Contrary, if the hard zone is stronger than the soft zone, their interface is similar to a conventional ceramic-metal interface (e.g., the $B_4C$/Al interface). The HDI strengthening effect can be achieved only if the hard zone is both strong enough and deformable enough attaining the right strength-toughness balance.

To avoid low work-hardening rates caused by the dislocation build up at the high-mismatch interface between the reinforcements and the matrix, the addition of novel deformable reinforcements such as MAX phase,[6] intermediate phases[65] and core-shell particles[64] in PRMMCs is necessary. They are capable of (1) modulate the interaction between the matrix and the reinforcement dislocation, (2) promote the proliferation and annihilation of heterogeneous interfacial dislocations, and (3) coordinate interfacial deformation to improve strain delocalization. Zhang et al.[6] found that the $Ti_3Al(Cu)C_2$ (2D MAX phase)/Cu interface is able to form a Lommer-Cottrel (LC) lock through sliding and interactions. The cross-slip of dislocations is impeded by the $Ti_3Al(Cu)C_2$/Cu heterostructured interface and the LC lock at high strain levels, resulting in significant forest hardening. To address strain localization caused by deformation incompatibility in homogeneous $Ti_2AlC$/TiAl composites, Liu et al.[4] attempted to promote strain distribution by introducing a high density of $Ti_2AlC$/TiAl heterogeneous interface. The strength difference between $Ti_2AlC$ and TiAl led to a heterogeneous deformation and load transfer. This triggered the redistribution of stress states from uniaxial to multiaxial stresses along the lamellar structure, resulting in significant HDI strengthening. **Figure 10** demonstrates the effect of the $Ti_2AlC(1\bar{1}0\bar{3})$/TiAl$(111)$ heterogeneous interface under different compressive strains with the evolution of defect structure and

strain distribution. The $Ti_2AlC(1\bar{1}0\bar{3})$/TiAl(111) interface is not only the main obstacle to dislocation expansion between $Ti_2AlC$ and TiAl, but also the source of dislocation nucleation in $Ti_2AlC$ and TiAl, which undoubtedly help to avoid strain localization at heterogeneous interfaces and promote uniform distribution of shear strain at the interface.

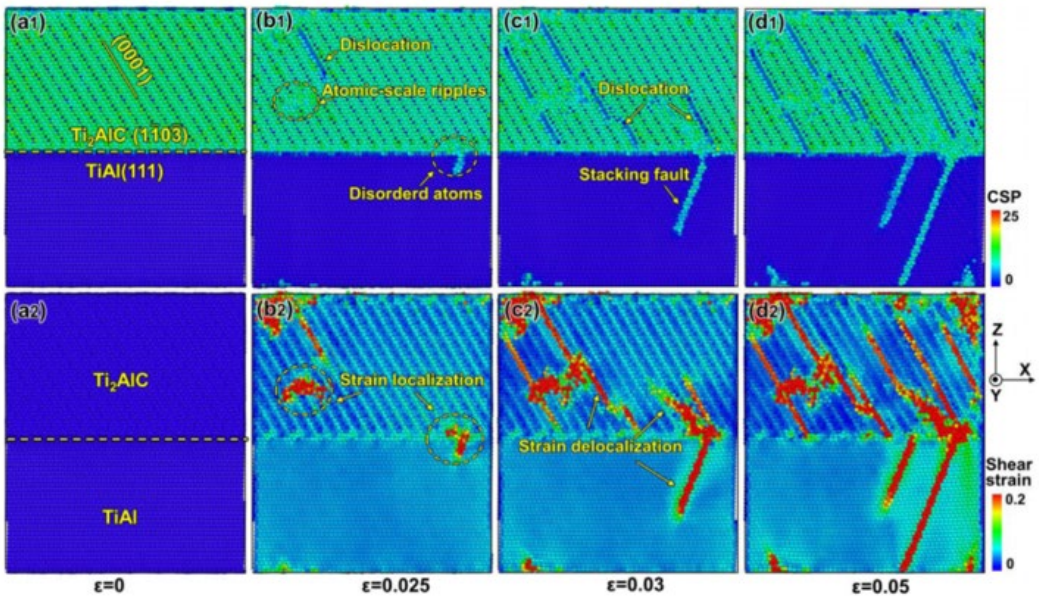


**Figure 10.** Defect structure and strain partitioning for $Ti_2AlC$ $(1\bar{1}0\bar{3})$/TiAl (111) interfacial model at different strain. (a1, a2) ε=0; (b1, b2) ε=0.025; (c1, c2) ε=0.03; (d1, d2) ε=0.05. Reproduced with permission.[4] Copyright 2023, Elsevier.

In metallic nanolayered composites (MNCs), diminishing the layer thickness to nanoscale levels significantly increases the interface proportion and dramatically reduces the density of mobile dislocations. Consequently, the interface acts as a primary source of plastic deformation[92] and the interfacial plasticity becomes key to enhance the mechanical properties of these composites. Misra et al.[93] systematically investigated the effect of the scale (from nano to micron) on the mechanical properties of copper-based MNCs, and concluded the dislocation mechanism for the strength of MNCs at different layer thicknesses: as the layer thickness increases, the dislocations shift from crossing the interface to tending to accumulate at the interface (**Figure 11**).

Interfacial strengthening is highly dependent on the interfacial structure at atomic scale, and although many heterogeneous interfaces are capable of hindering dislocation motion, their strengthening efficiencies and the intrinsic strengthening-hardening mechanisms associated with them are not exactly the same.[19, 92] For example, in pearlite steels consisting of submicron brittle cementite and ductile ferrite phases, the ferrite-cementite interface becomes a potential source of dislocations due to the drastic reduction in the number of intragranular dislocation sources.[94] Ohashi et al.[95] found that controlling the dislocation slip system associated with a ferrite-cementite interface, increased the strain hardening rate of the ferrite phase, resulting in higher plasticity of tensile pearlite steels. As shown in **Figure 12**, the spacing of the interfacial dislocations accommodates the mismatch strain between the ferrite and cementite phases and determines the corresponding forces and interfacial dislocation structure in the nanolayer composite model (Figure 12(b)).[18] Thus, by tailoring the interfacial atomic and dislocation structures, one can steer the evolution of interface dislocations that subsequently influence the yield and damage mechanisms in MNCs.

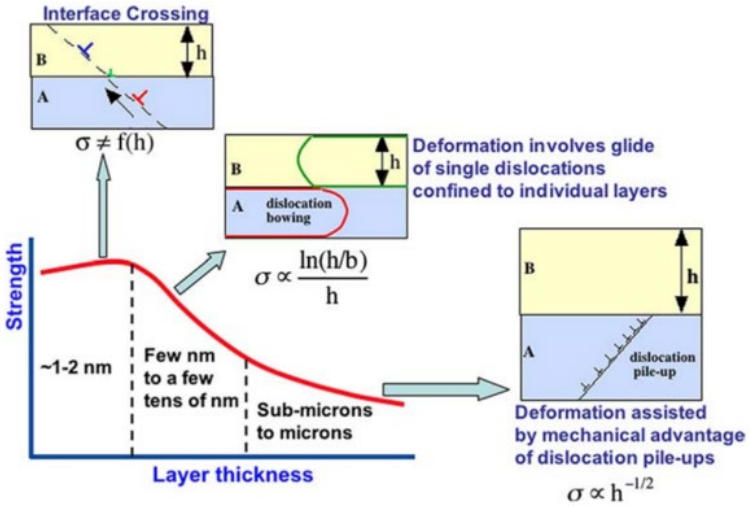


**Figure 11.** Schematic illustration of the dislocation mechanisms of multilayer strength operative at different length scale. Reproduced with permission.[93] Copyright 2005, Elsevier.

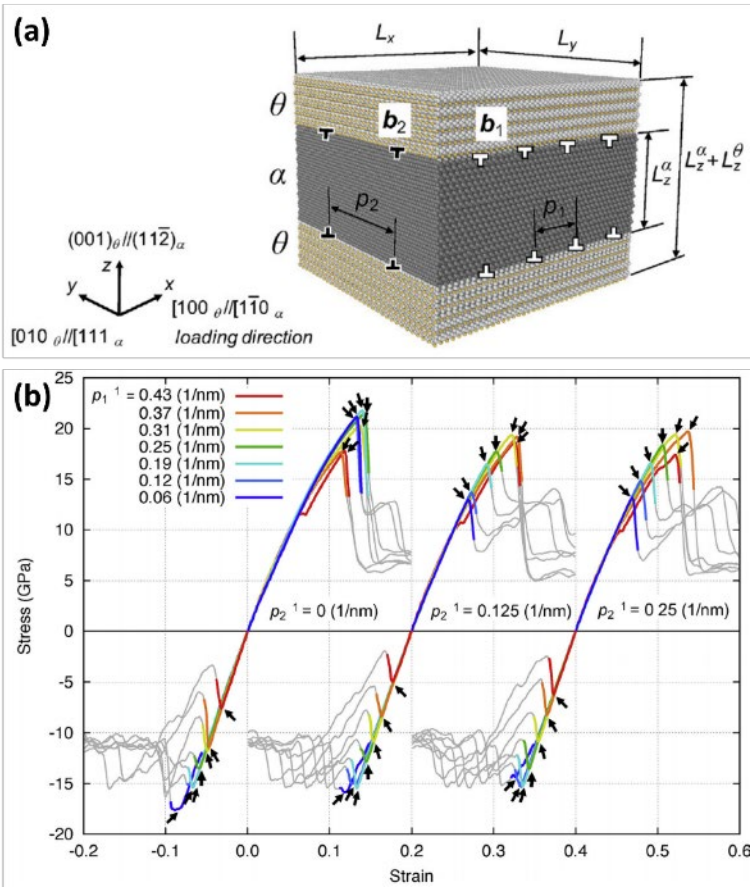


**Figure 12.** (a) Analysis model of a pearlite microstructure with the Bagaryatsky relationship. (b) Stress-strain curves of pearlite microstructures with various interfacial dislocation spacings $p_1$ and $p_2$ under x directional tensile/compressive deformation at T = 1 K. Black arrows show the occurrences of the initial inelastic deformations. Reproduced under terms of the CC-BY license.[18] Copyright 2019, T. Shimokawa, T. Niiyama, M. Okabe, J. Sawakoshi, published by Elsevier.

### 2.3.2. Hampering cracks

Heterogeneous interfaces inducing HDI strengthening and strain hardening play a key role in hindering crack initiation and extension. There are several ways to achieve that; for example, impeding crack initiation, altering crack extension paths, influencing the stress field at the crack tip, and bridging and closing microscopic cracks. HDI strengthening and strain hardening effects are capable of inducing a highly non-uniform microstructural state in the material, which significantly affects the dislocation

distribution, microcracks, and the formation of other defects and evolution.[62] Luo et al.[16] developed nanocomposites with inverse pearl layer structure using pure Mg as the soft phase, and SiC nanoparticle reinforced Mg as the hard phase. These nanocomposites showed high strength and tensile elongation. The locally hardened regions encountered during the crack initiation stage can effectively resist crack formation and extension due to the large strain gradient in the localized region. The structure utilizes the hard phase to bear the main load enhancing the strength, and the soft phase to stabilize the microcrack extension that improves the ductility. Staggered microcracks shift the local stress of the soft phase from tension to shear. Fragmentation of the hard phase results in shearing of the soft phase through the tensile-shear chain mechanism facilitated by a basal plane orientation.[96] This alignment allows Mg particles within the soft phase to undergo shear loading parallel to the basal plane, activating the basal plane slip system.

### 2.3.3. Absorbing defects

MNCs consisting of alternating layers of different metals have gained significant interest due to exceptional strength, hardness, thermal stability, corrosion and impact resistance.[97] The superior characteristics of MNCs stem from dense, stable heterogeneous interfaces formed through repeated rolling. In these composites, dynamic dislocation recovery is common, with material interfaces or free surfaces serving as defect (dislocation) sinks. Notably, metallic/amorphous nanolayered composites, such as Cu/CuZr, exhibit near-elastic tensile properties. MD simulations have demonstrated that the interface between crystalline and amorphous layers in nanolaminates acts as an effective dislocation sink.[98] Under some extreme service conditions (e.g., nuclear radiation environments), the single-phase organization is

susceptible to coarsening by short-range diffusion due to the low atomic packing density and high atomic mobility at grain boundaries (GBs).[99] To tackle these issues, the use of phase boundaries made of mismatched elements can boost thermal stability and resistance to radiation in composites. Gao et al.[21] used LAMMPS for MD simulations to investigate how radiation affects interfaces and how helium bubbles form. Their research indicates that adjusting the structure at the interface can directly affect the behavior of helium.

**Figure 13** illustrates that sharp interfaces facilitate helium atom or cluster accumulation, attributed to its two-dimensional diffusion behavior. Conversely, regions with interfacial transitions and amorphous characteristics markedly impede the development of sizable helium clusters. This is because three-dimensional interfaces have extra free volume with high capacity for helium absorption promoting the initial formation of clusters yet restrict their expansion.[100] The stability of stacking fault tetrahedra (SFTs) and interfacial voids in irradiated Cu/Ag nanolayered composites was investigated by TEM.[100] Atomistic simulations showed that heterogeneous interfaces can directly facilitate transition vacancies to SFTs. This is due to the nonuniform stress field generated by mismatched dislocations on the semi-coherent interfaces reduces the activation barrier of the interfacial phase transition. SFTs initially emerge and expand at the interface underlying layer. The underlying layer of SFTs first forms and grows at the interface, and dislocation nucleation is more favorable when newly released dislocations react with the SFT and destroy it, thus returning the interface to its planar original state.

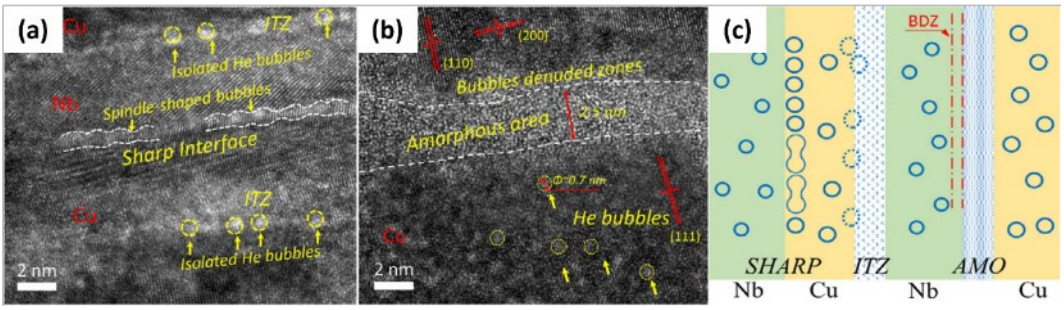


**Figure 13.** HRTEM images of He bubble morphology in (a) sharp interfaces and interfacial transition zones, and (b) the amorphous area. (c) Schematic of helium bubble evolution as the function of interfacial structures according to the experimental observation, where BDZ stands for bubble denuded zone. Reproduced with permission.[21] Copyright 2020, Elsevier.

2.4. Other structures

Recently, the introduction of intermediate phases by interfacial reactions or other means (e.g., precipitation[65]) to design novel interfacial structures has become an increasingly common interfacial design strategy. Some examples of novel interfacial structure design are shown in **Figure 14**(a-d), including core-shell structure,[64] precipitation-assisted structure,[65] disordered structure,[101] and 3D interlocking structure.[5]

The core-shell structure is characterized by an intermetallic compound shell, rather than using singular particle reinforcement. The intermetallic shell thinness restricts crack size, while the ductile metal core impedes crack propagation. This configuration of CS particles offers benefits in curbing crack initiation and growth,[102] thus enhancing both strength and plasticity of PRMMCs. Since cracks are inclined to emerge in the intermetallic compound hard shell of CS-reinforced particles,[103] shell properties such as shell thickness, homogeneity, densification, interfacial compatibility of CS-reinforced particles with the metal matrix, and interfacial bond strength, play a key role in crack initiation. Zhang[64] addressed the A356 aluminum alloy matrix PRMMC's challenge of reconciling strength with plasticity by developing novel in situ synthesized reinforcing particles featuring a unique CS structure with a bilayer

shell (Figure 14 (a)). This structure enhances stress resistance and toughness, with the nanoparticle outer layer impeding crack progression, thereby significantly postponing crack initiation. Yang[101] designed a disordered interface by introducing an ultrathin amorphous layer in the Cu/Nb multilayers. Compared to the sharp interface, the disordered interface can smear the impinging dislocation with relaxing the in-plane and out-of-plane Burgers vectors, thus inducing a remarkable hardening in the Cu/Nb multilayers (Figure 14(c)). Liu[5] constructed 3D nanostructured interfaces based on TiB nanowhiskers by utilizing the time-dependent reaction of BNNSs/Ti system, and the nano-interlocking effect brought by the 3D structure increased the dislocation density under loading and improved the interfacial shear strength (Figure 14(d)).

The common design feature of these novel interfacial structures is to promote a more homogeneous stress-strain distribution in the interfacial region by improving the physical/chemical compatibility of the original interfaces, facilitating the obstruction of crack development/crack deflection, and promoting the proliferation and transport of dislocations at the interfaces, which ultimately enhances the strain-hardening capacity of MMCs. **Table 1** summarized the improvement in the performance of MMCs by some novel interface structure designs.

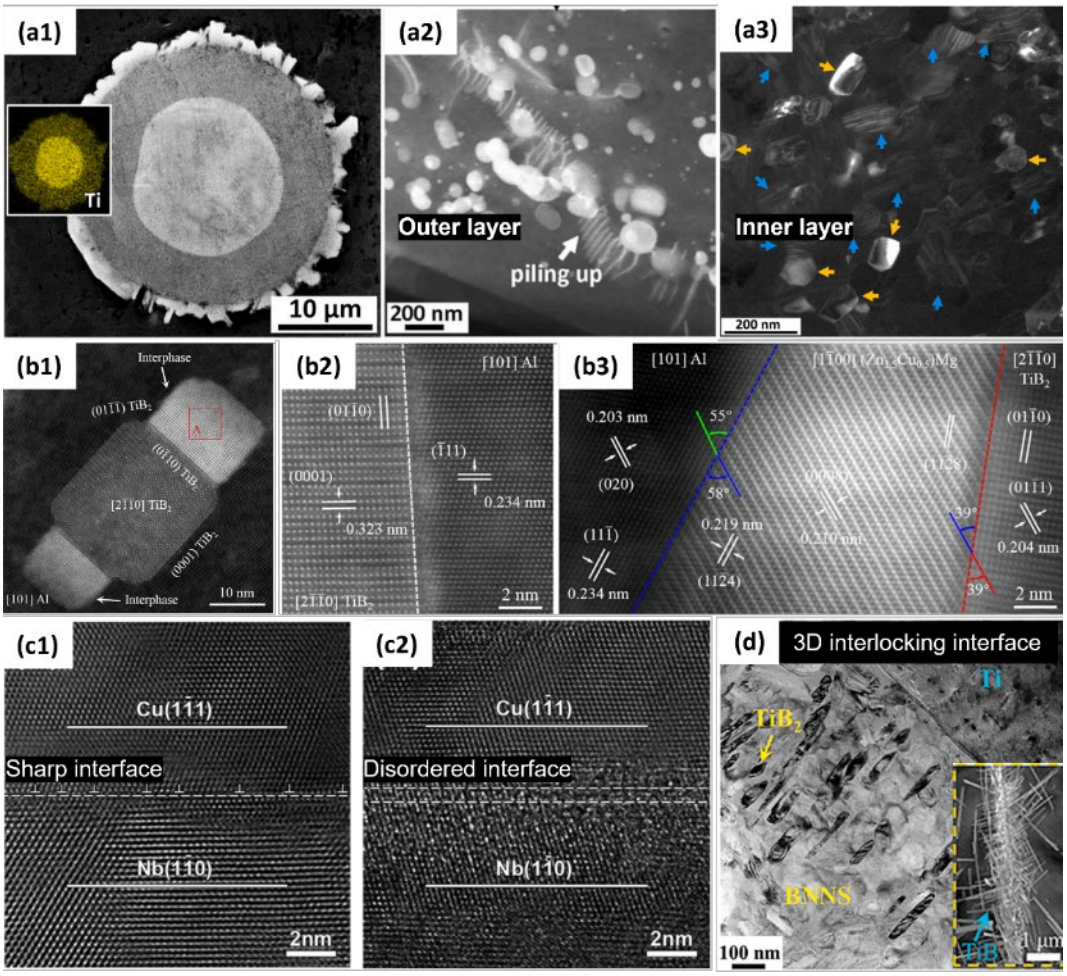


**Figure 14.** Some novel interfacial structures in MMCs. (a) Core-shell structure interface. Reproduced with permission.[64] Copyright 2021, Elsevier. (b) Precipitation-assisted interface. Reproduced with permission.[65] Copyright 2023, Elsevier. (c) Disordered interface. Reproduced with permission.[101] Copyright 2021, Elsevier. (d) 3D interlocking interface. Reproduced with permission.[5] Copyright 2023, Elsevier.

**Table 1.** The list of performance comparison of MMCs by some novel interface structure designs.

| Composites | Interface structure | Strengthening mechanism | Mechanical properties | | | | Ref. |
|---|---|---|---|---|---|---|---|
| | | | Yield strength (MPa) | Tensile strength (MPa) | Compressive strength (MPa) | Elongation to fracture (%) | |
| 5 vol.% SiC/Mg | Inverse nacre structure | HDI strengthening and strain hardening, impeding crack initiation and propagation | 255 ± 9 | 284 ± 8 | - | 15.1 ± 1.7 | [104] |
| | - | | 278 ± 6 | 315 ± 12 | - | 2.9 ± 0.4 | |
| Cu-0.74 wt.% Cr-0.044 wt.% Zr/Cu | Gradient structure | | 432 | 494 | - | 16.9 | [26] |
| | - | | 436 | 500 | - | 8.3 | |
| 20 wt.% $Ti_3AlC_2$/Cu-1000°C | Gradient structure | | - | - | 348 | 57.1 | [105] |
| 20 wt.% $Ti_3AlC_2$/Cu-760°C | - | | - | - | 230 | 53.1 | |
| $Ti_2AlC$/TiAl | Heterogeneous structure | | - | - | 2065 ± 5 | 27.4± 1 | [4] |
| | - | | - | - | 1590 ± 3 | 18.4 ± 1 | |
| $(Al,Si)_3Ti$/A356 | Core-shell structure | impeding crack initiation and propagation, TRIP | 268±7.9 | 373±8.8 | - | 8.3±0.8 | [64] |
| | - | | 284 | 381 | - | 3.1 | |
| Fe50Mn30Co10Cr10 | Core-shell structure | | 960±16 | 1228±14 | - | 12.4±0.4 | [106] |
| | - | | 477±6 | 731±7 | - | 16.6±0.5 | |
| 2.2 vol.% $TiB_2$/7075Al-peak aging | Precipitation-assisted structure | precipitation-assisted interface tailoring, improving the coherency and strength of interface | 610.5 ± 6.4 | 676.4 ± 5.8 | - | 11.5 ± 0.2 | [65] |
| 2.2 vol.% $TiB_2$/7075Al-water quenching | - | | 277.0 ± 35.4 | 506.8 ± 4.7 | - | 23.1 ± 2.9 | |
| $SiO_2$@$Al_2O_3$-1h/Al | 3D interlocking structure | Enhancing load transfer efficiency, impeding crack initiation and propagation | 188 ± 2 | 250 ± 2 | - | 16.2 ± 0.3 | [34] |
| $Al_2O_3$/Al | - | | 169 ± 3 | 230 ± 1 | - | 14.8 ± 0.2 | |
| BN nanosheet -TiB/TC4 | 3D interlocking structure | | - | 1140.5 ± 5.1 | - | 1.52 ± 0.2 | [5] |
| BN nanosheet/TC4 | - | | - | 953.1 ± 8.3 | - | 10.54 ± 0.2 | |
| 0.5 wt.% Ni nanoparticles@GNPs/Al | 3D interlocking structure | | 154 | 177 | - | 18.4 | [60] |
| 0.5 wt.% Ni nanoparticles@RGO/Al | - | | 120 | 148 | - | 14.4 | |
| 0.3 wt.% $Ti_3Al(Cu)C_2$/Cu | Stacking faults-assisted structure | LC lock, TWIP | 300 | 319 | - | 37 | [6] |
| 0.1 wt.% $Ti_3Al(Cu)C_2$/Cu | | | 228 | 242 | - | 31 | |

## 3. Defect control

The fundamentals of crystallography have led to the realization that even at 0 K, not all atoms in actual crystals have a strict periodic arrangement because there are tiny regions in the crystal in which the periodicity of the atomic arrangement is disrupted when passing within or through such regions, and such regions are called crystal defects.[107] The mismatch in coefficient of thermal expansion (CTE) and elastic modulus (EM) between the reinforcement and metal matrix in MMCs, leads to the formation of

thermal residual stresses and defects at heterogeneous interfaces when cooling at room temperature.[108] Furthermore, the actual preparation of MMCs will also inevitably introduce numerous interfacial defects. Severe plastic deformation of a metallic material induces the formation of high-density crystalline defects. Examples of the plastic deformation include mechanical alloying (MA),[109, 110] high-pressure torsion (HPT)[111, 112] and accumulated rolling (ARB)[31] etc. For nanocarbon reinforcements, nano-defect engineering was introduced to expose more prismatic surfaces and to increase the number of interfacial reaction sites (**Figure 14**).[113] Common strategies to achieve nano-defect engineering include chemical treatments,[114, 115] particle irradiation,[113] and mechanical damage[9, 116] etc. As shown in Figure 14(a), Chu[113] produced a finite number of structural defects on the surface of graphene oxide by plasma treatment of graphene oxide for a certain duration. As shown in Figure 14(b), Guo et al.[114] could generate specific types and numbers of defects on the surface of carbon nanotubes by etching and oxidising carbon nanotubes using different mixed solutions ($NH_4OH$-$H_2O_2$, $H_2SO_4$-$H_2O_2$, $HNO_3$-$H_2SO_4$), and different types and numbers of nanodefects would have different effects on the interfacial bonding of Al-CNTs. different effects on the interfacial bonding of Al-CNTs. As shown in Figure 14(c), Dong et al.[116] can finely regulate the defect density and sp2 cluster size of dense graphene blocks by controlling the ball milling time.

Interfacial defects can affect mechanical strength. The presence of interfacial defects may weaken interfacial bonding, which either leads to insufficient load transfer and reduces the mechanical strength of the composite, or it increases the interfacial bonding strength (e.g., vacancies on graphene promote the formation of C-Al chemical bonds).[117] Interfacial defects also affect the thermal properties, e.g., increasing the interfacial vacancy density[12] increasing dislocation density near the interface[11, 118] introducing additional phonon scattering; this is in turn which increases the interfacial thermal resistance of Gr/Cu composites.[11, 97] Furthermore, interfacial defects affect the thermal diffusion behavior[119], segregation and precipitation of solute or impurity atoms[120] and recovery of radiation-induced defects etc. [20] The interfacial structure and properties of composites are crucial in determining whether the

reinforcing effect of the matrix reinforcement can be fully utilized. The development of high-performance MMCs through interfacial defect engineering can only be explored with a full understanding of the mechanisms of formation, evolution, and structural characteristics of interfacial defects at the reinforcement-matrix interface.

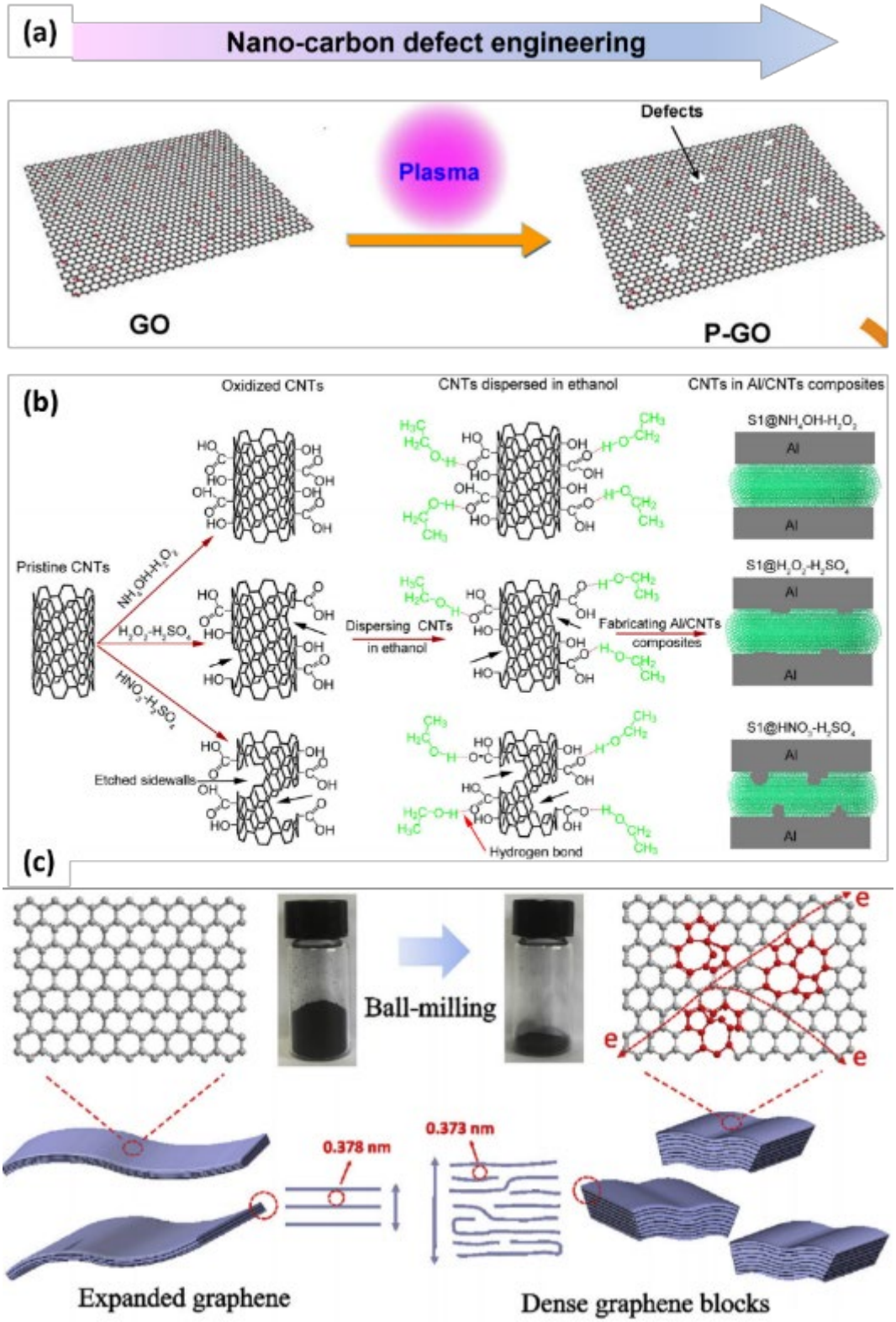


**Figure 15.** Several types of defect engineering strategies applied to nano-carbon: (a) Plasma treatment. Reproduced with permission.[113] Copyright 2018, Elsevier. (b) Chemical treatment. Reproduced with permission.[114] Copyright 2018, Elsevier. (c) Mechanical treatment. Reproduced with permission.[116]

### 3.1. Vacancy defect

Vacancies at the reinforcement/metal matrix interface region in metal MMCs include intrinsic vacancies (e.g., C vacancies on structurally damaged CNTs and equilibrium vacancies in the matrix-metal lattice) and vacancies due to the interactions between matrix atoms and reinforcing-phase atoms during preparation (e.g., Kirkendall's effect due to the mutual diffusion coefficient). The number of vacancies, type and distribution will significantly affect the atomic reconstruction and electron transfer at the interface.[121, 122] For example, different effect a vacancy close to or far from the interface on the side of the metal matrix or reinforcement.).[123] Likewise for single, double, tetrahedral, and octahedral vacancies, etc.).[117] Vacancy characteristics will in turn affect interfacial properties such as density of states (DOSs) and interfacial adhesion energy. According to statistical thermodynamics,[107] a certain number of vacancies always exist in crystals at thermal equilibrium above absolute zero. This concentration is called equilibrium concentration of point defects in the crystal at this temperature $c_v$ , which can be expressed as:

$$c_v = \frac{n_e}{N} = \exp\left\{-\frac{\Delta E_V}{kT} + \frac{\Delta S_V}{k}\right\} = A \cdot \exp\left\{-\frac{\Delta E_V}{kT}\right\} \tag{3-1}$$

where $n_e$ denotes the number of equilibrium vacancies, and $N$ denotes the total number of formation sites, $\Delta E_V$ denotes the change in formation energy for each additional vacancy, $\Delta S_V$ denotes the corresponding vibrational entropy change, $k$ is the Boltzmann constant, and $A$ denotes the coefficient determined by the vibrational entropy. Obviously, the higher the temperature, the larger the equilibrium concentration of vacancies. The vacancy formation energy can be expressed by the following equation:[124]

$$E_{V\,f} = E_{defect} - E_{pure} + E_{matrix} \tag{3-2}$$

where $E_{V\,f}$ denotes the total energy of the supercell model of the matrix atom with one vacancy, $E_{pure}$

denotes the total energy of a perfect matrix atom cell without a vacancy, $E_{matrix}$ denotes the energy of a matrix atom. Due to different elements or positions, the vacancy formation energy $E_{V\,f}$ may vary considerably. For example, in the Al(111)/6H-SiC(0001) interface,[123] the second Al atomic layer near the interface has the smallest $E_{V\,f}$ i.e., it is most prone to Al vacancies, whereas vacancies are difficult to appear in SiC. This may be attributed to the strong bonding between SiC and Al atoms that makes the outermost Al atoms tend to shift to the SiC side, thus weakening the effect on sub-energetic Al.

### 3.1.1. Interfacial bonding strength

The presence of interfacial vacancies affects the interfacial atomic bonding, which in turn affects the reinforcement-metal matrix interfacial bonding strength.[36, 37, 123] Graphene, a hexagonal honeycomb lattice of carbon atoms forming a single-atom layer, exhibits key functional characteristics, including high electrical and thermal conductivity, remarkable strength, optical transparency, and chemical inertness.[121, 125, 126] Various structural defects are inevitably introduced during the production of graphene[127] such as single vacancy (SV) defects,[128] multi-vacancy defects,[129] Stone-Wales(S-W) defects,[122] complex graphene defects, edge defects and one-dimensional defects, etc.[130] Defects in graphene significantly influence the efficacy of graphene-based photovoltaic and thermoelectric composites with their performance hinged on the graphene-metal interface qualities at contact electrodes. Understanding how prevalent defects affect these interfacial properties are affected by in graphene is crucial for tailoring graphene-metal interfaces through interfacial defect engineering.[121, 122]

Changes in the number, type and position of interfacial vacancies affect the interfacial bonding strength in three different ways. First, as the number of interfacial vacancies changes, the electron density

difference (EDD) at the C-metal interface also changes. Mei et al.[117] explored the effect of the number of interfacial vacancies on the graphene-Al interfacial bonding with the help of first principles. No chemical bonding is formed at the graphene-Al interface when graphene has no vacancy defects. When a single vacancy is introduced in graphene, the graphene wrinkles and some of the C atoms start to approach the Al atomic layer, but the chemical bond formed is weak and insignificant. With the increase of vacancies, new chemical bonds formed at the C-Al interface. Second, the effect on the nature of the interface will be different depending on the type of vacancies. **Figure 16**(a) shows the pristine graphene-Al (111) interface, S-W defect graphene-Al (111) interface, SV graphene/Al (111) interface, and DV graphene/Al (111) interface in equilibrium configuration.[131] For the pristine graphene-Al (111) interface, the relative positions between the Al and C atoms are almost unchanged from the top view; however, for S-W defect graphene-Al (111) interface and SV graphene-Al (111) interface, a significant buckling of the C-atom layer at the graphene defect and the Al-atom layer underneath was observed. The significant reduction of the equilibrium layer spacing $d_{C-Al}$ confirms that S-W defects and SV defects indeed improve the graphene/Al interfacial bond strength. Variations in charge density indicate that the formation of strong Al-C covalent bonds at defects primarily enhances the mechanical performance of graphene/aluminum composites. Third, the location of vacancies modifies the electronic structure and bonding strength at the interface. Figure 16(b1, b2) show the tensile fracture position models of the C-terminated and Si-terminated interfaces with different points of vacancies and the corresponding $W_{ad}$ respectively.[123] Fracture in the Al/SiC composite occurs not at the Al/SiC interface but within the aluminum layer close to it. This is due to the interaction with SiC at the interface, where a minor portion of aluminum free electrons are drawn towards the SiC, resulting in fewer free electrons for the aluminum atoms adjacent to

the interface. Consequently, this electron depletion weakens the metallic bonds among these aluminum atoms in agreement with a previous work.[120]

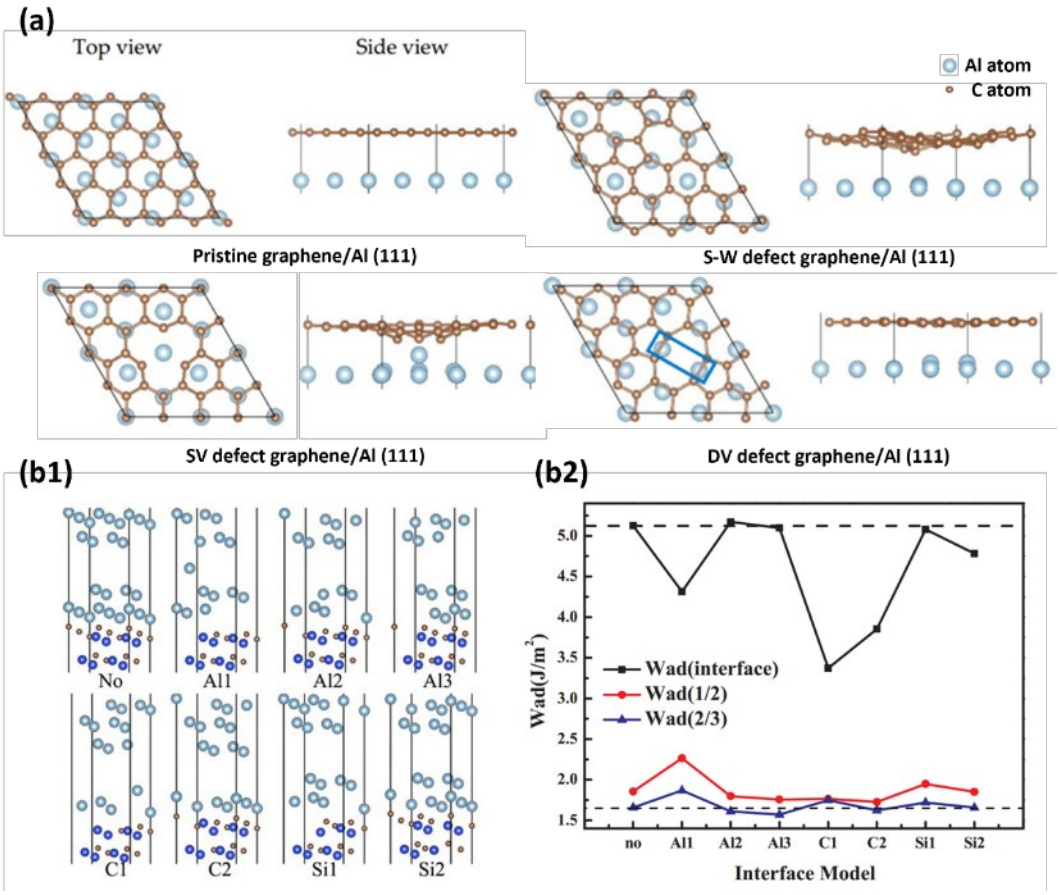


**Figure 16.** (a) Top views and side views of the pristine graphene, the S-W defect graphene, the SV graphene and the DV graphene on the Al (111) surface after the structural optimization. Reproduced under terms of the CC-BY license.[131] Copyright 2021, X. Zhang, S. Wang, published by MDPI. (b1) The models of tensile fracture position of the C-terminated interfaces with different point vacancy. (b2) The adhesion energy of the three interfaces at the Al side for the C-terminated interfaces. Reproduced with permission.[123] Copyright 2019, Elsevier.

### 3.1.2. Interfacial diffusion

Vacancies often act as fast pathways for interfacial diffusion.[132] Enhancing elemental diffusion through the creation of high-density defects offers innovative strategies to strengthen interfacial bonding

in MMCs. For instance, the challenging diffusion between Fe and Mg at the steel/Mg composite interface is attributed to the positive enthalpy of mixing process that hinders the formation of strong metallurgical bonds. As shown in **Figure 17**, by applying large plastic deformation and appropriate tempering process, Sun et al.[133] formed a high density of defects on a 20 steel side of a non-equilibrium interface in large deformation rolled 20 steel/Mg composites (Figure 16(d-i)). The presence of a large number of lattice defects (vacancies, dislocations, etc.) damages the spatial lattice ordering, which inevitably leads to an increase in the internal energy and entropy of the crystals. Defect-rich areas at grain boundaries facilitate the internal energy surpassing the Gibbs free energy necessary for creating Fe-based supersaturated solid solutions. These zones act as diffusion pathways for Mg and promote the alloying process between Fe and Mg at the interface.

For interfacial systems that are easy to diffuse (e.g., Cu-Cr),[134] a large number of vacancies are also generated at the Cu/Cr interface as well as in the Cr matrix. This is due to the large difference between the interdiffusion coefficients of Cu/Cr (**Figure 18**(a)). The existence of these vacancies provides various fast diffusion channels for O atoms to enter the Cr matrix that leads to the formation of $Cr_2O_3$ particles near the micropores. These nano-$Cr_2O_3$ particles enhance the interfacial mechanical properties through a dispersion strengthening mechanism. The diffusion of substitutional atoms via the vacancy mechanism requires alloy atoms to move through vacancies adjacent to them. The formation of vacancies invariably interferes with the bonds among adjacent atoms. When the bonds between the atoms of the alloy and the matrix are stronger than those linking the matrix to the base atoms, it simplifies the breaking of matrix atom bonds to generate vacancies.[39]

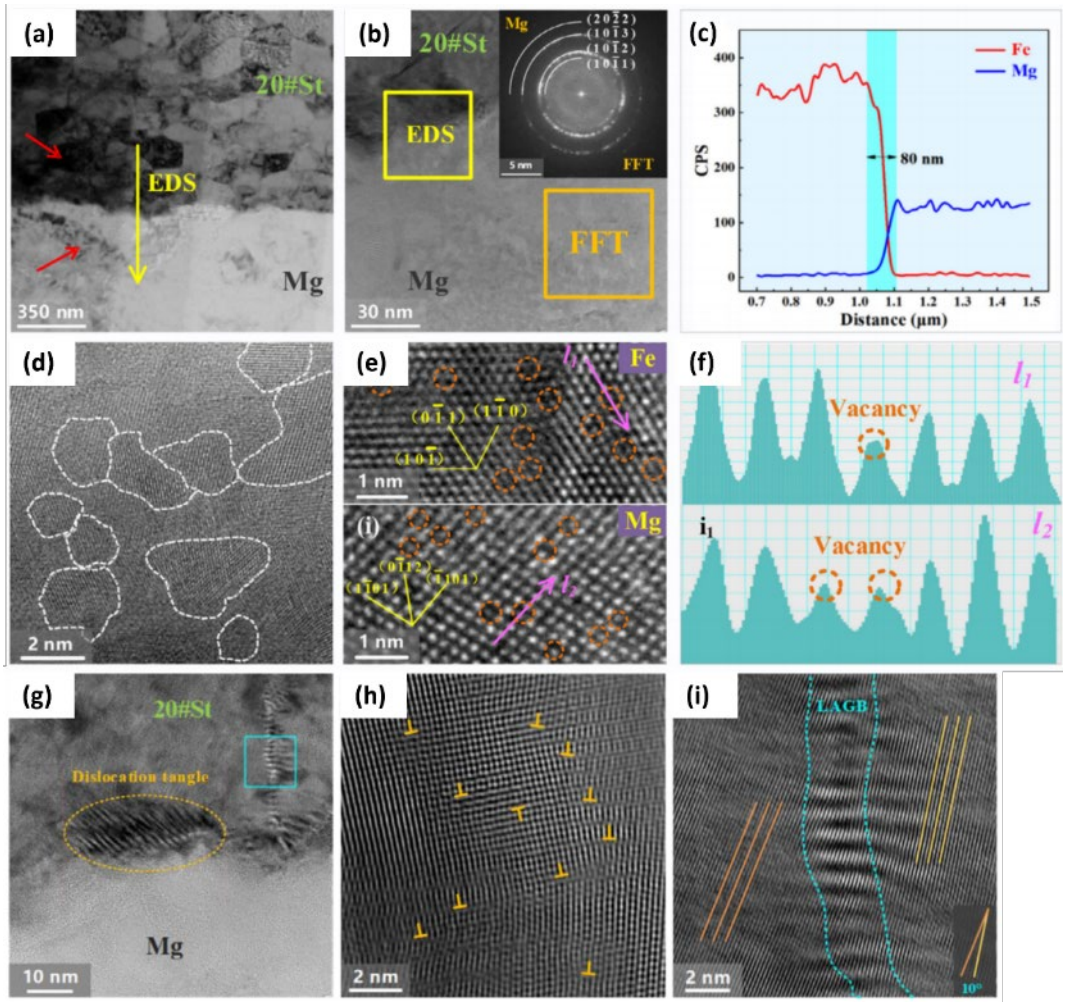


**Figure 17.** Large deformation rolled 20#steel/Mg composite interface: (a, b) Low and high magnification image showing interface morphology. (c) EDS line scan results. (d) Grain morphology and size of Mg; (e, f) Vacancy distribution in 20#steel and Mg grain. (g) Dislocation entanglement; (h) High density dislocations; (c) LAGB (enlarged view of box in (g). Reproduced with permission.[133] Copyright 2023, Elsevier.

Vacancies promote the diffusion of the alloying elements and at the same time make it easier for corrosive ions such as $Cl^-$ to enter the material (**Figure 18**(b)).[135] Oxygen vacancies and interstitial defects, characterized by their density and diffusion coefficients, primarily dictate the growth and deterioration kinetics of the alumina protective film. The early stage of corrosion caused by the adsorption and infiltration of corrosive electrolytes (such as chloride ions) into the film, stems from oxygen vacancies serving as electron donors. The generation of oxygen and aluminum vacancies within

oxide films is endothermic, with aluminum vacancies requiring approximately 30-60% more energy for formation than oxygen vacancies, indicating a predisposition to the easier formation of oxygen vacancies.[136] Due to the alternating distribution of Al and O in α-$Al_2O_3$, Cl atoms wanting to enter the oxide film must pass through Al vacancies, and the intrinsic characteristics of positively charged Al atoms and negatively charged O atoms make it easier for Cl atoms with strong electron affinity to enter the O vacancies. Contrary, the entry of Cl ions into the Al vacancies is less favorable. When C in graphene is doped into the oxide film by thermal diffusion or reaction, the formation energy of O vacancies and the entry barrier of Cl atoms increase significantly. The donor density decreases, and the reduction of carriers improves the corrosion resistance of the oxide film.[135]

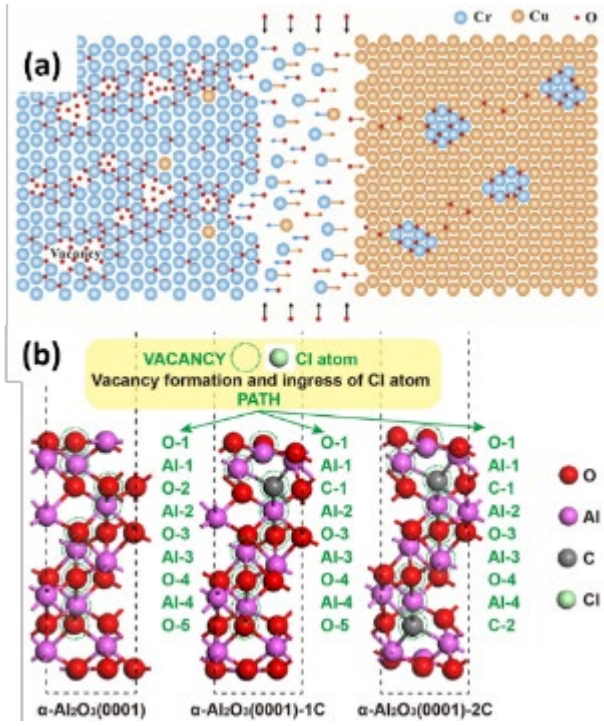


**Figure 18.** (a) Schematic diagram of Cu, Cr and O atomics diffusion at the Cu-Cr interface during the pressure sintering process. Reproduced with permission.[134] Copyright 2019, Elsevier. (b) Schematics of the α-$Al_2O_3$ (0001) slab, single-carbon-atom-doped α-$Al_2O_3$(0001)-1C slab, and dual-carbon-atom-doped α-$Al_2O_3$(0001)-2C slab. Reproduced with permission.[135] Copyright 2021, American Chemical Society.

### 3.1.3. Interfacial chemical reactivity

Interfacial defects significantly influence the occurrence and severity of interfacial reactions, with the reactivity, reaction type, and selectivity of chemical substrates depending on electron density, substrate kinetic stability, and unstable electron availability. Different types of interfacial defects also have different effects on the size, number, distribution and crystallographic characteristics of interfacial reaction products.[13, 115, 137]

Graphene defects can enhance chemical reactivity at the graphene/metal interface.[121] **Figure 19**(a1, a2) shows that Mg atoms not only fill graphene pores, providing electrons to re-establish their sp2 hybridization, but also react with oxygen in chemical groups, generating MgO particles at the graphene-Mg interface. Figure 19(a3) shows that the integration of Mg acts as a "penetrating" force in graphene, whereas MgO nanoparticles serve as "stitches," thereby creating a robust interfacial bond within the composite. Furthermore, in order to evaluate the redox reactivity of pure graphene and graphene with S-W defects, Jayaprakash et al.[138] found a significant enhancement in the region selectivity and reactivity of S-W-deficient graphene due to the resulting geometrical deviation. The Fukui results for S-W defected graphene are shown in the color iso-density plots in Figure 19(b1, b2). It can be clearly seen that the heptagonal and pentagonal regions in the S-W defects are the most active regions on the surface of graphene, and that the S-W defects can indeed promote the thermodynamic and kinetic reactivity of graphene.

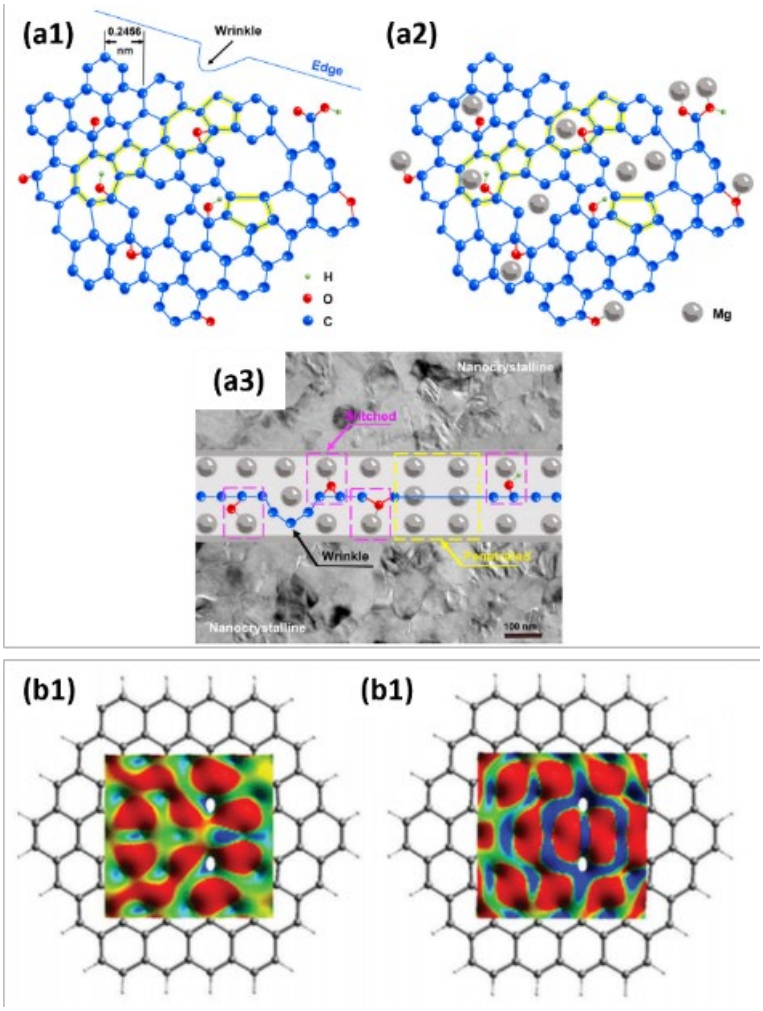


**Figure 19.** (a1) In-plane atomic structure of GNPs with defects, (a2) GNPs combined with Mg atoms, and (a3) interaction between defective GNPs and Mg matrix on cross section. Reproduced with permission.[139] Copyright 2019, Elsevier. (b1, b2) Fukui (DFT, the results for the SW-defected graphene, presented as colored isodensity. Reproduced with permission.[138] Copyright 2016, American Chemical Society.

### 3.1.4. Vacancy-dislocation interaction

As mentioned at the beginning of 2.1.2 Strain hardening, interface-dislocation interactions play a key role during plastic deformation. Trying to understand the effect of interfacial vacancy defects on the interfacial deformation mechanism is essentially an investigation of the interfacial vacancy-dislocation interaction mechanism.

For example, the plastic deformation behavior of nanolaminated composites (Al/Nb) is controlled by slip dislocation-interface interactions.[140] Atomistic simulations show that slip dislocations can effectively climb near and within the interface through vacancy emission and absorption at the dislocation cores,[141] and thus a high vacancy diffusivity and vacancy concentration at the interface will help to restore the dislocation content at the interface.[140]

### 3.2. Doping defect

Through surface modification of the reinforcement phase (e.g., defect and doping engineering) and alloying of the metal matrix to modulate the atomic and electronic structure of the reinforcement-matrix interface, the substitution of some of the atoms in the interfacial region can sometimes lead to unexpected effects, such as increasing the interfacial bond strength,[142] the oxidation resistance of the interfacial organization[143] and corrosion resistance of the interfacial organization.[135, 144]

The graphene structure can be modified by introducing foreign atoms at the graphene defects, and therefore, defective graphene or similar two-dimensional or three-dimensional graphene derivatives containing impurity atoms such as nitrogen, sulfur, phosphorus, silicon, etc., are becoming increasingly attractive.[117, 145, 146] As shown in **Figure 20**, the incorporation of Mg-alloyed F-GNPs can effectively improve the corrosion resistance of AMCs,[147] which is attributed to the insulating property induced by F doping and the molecular impermeability inherited from graphene that can improve the corrosion resistance of the composites, while the good double-sided metallurgical compatibility of Mg elements provides a strong interfacial bonding to avoid the peeling off of the protective layer and the corrosion-promotion activity effect.

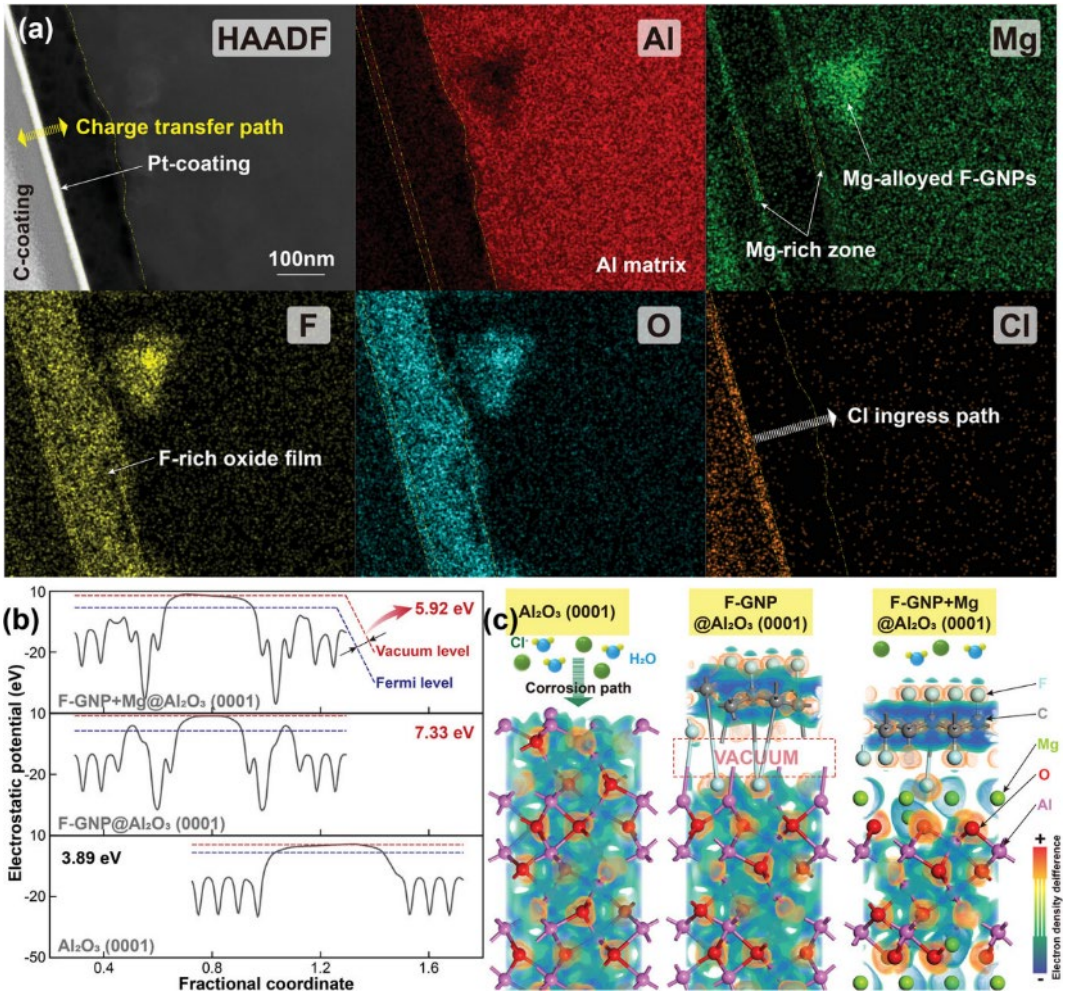


**Figure 20.** Experimental observation and theoretical calculation of the corrosion suppression activity: (a) elemental distribution of the corroded surface. (b) work functions and (c) electron density differences of three slabs. Reproduced under terms of the CC-BY license.[147] Copyright 2022, Y. Xie, X. Meng, Y. Chang, D. Mao, Z. Qin, L. Wan, Y. Huang, Wiley.

Wang et al.[142] calculated the effects of the substitution position of Zr atoms at the (111)Cu/(110)W interface on interfacial strength, interfacial energy, and electronic structure. The solid solution energy of a Zr atom substituting a W atom, or a Cu atom, at the Cu/W interface $E_{sol}$ can be expressed as:

$$E_{sol} = E_{Cu/W-Zr} - E_{Cu/W} + E_X - E_{Zr} \quad (3\text{-}3)$$

of which $E_{Cu/W-Zr}$ and $E_{Cu/W}$ are the total energies of the Cu/W interface with and without Zr substitution, respectively, $E_X$ is the total energy of a substituted W or Cu atom in BCC W or FCC Cu, $E_{Zr}$

is the total energy of each Zr atom in HCP Zr. The calculations of solid solution energy $E_{sol}$ and work of adhesion $W_{\mathrm{ad}}$ show that the substitution of W atoms by Zr is not only thermodynamically extremely favorable ($E_{sol}$ <-1.1 eV), but also significantly increases the interfacial strength of the Cu/W interface. Contrary the replacement of Cu atoms by Zr has little effect on the interfacial strength of the Cu/W interface. Therefore, W atoms, in the W lattice of the Cu/W interface, are technologically targeted to be replaced by Zr atoms, it would be expected that both the interfacial strength and the interfacial stability of the Cu/W interface would be enhanced. Zhang[148] theoretically calculated the effects of replacing Ni atoms by Cr cations, and at the Ni/C interface, and C atoms by B anions in graphene. This work suggests that these substitutions induced electronic coupling and chemical bonding at the Ni/C interface that increased the adsorption capability of the B-doped framework. (**Figure 21**). Such changes are pivotal for the robust interface formation between Gr(B) and Ni(Cr).

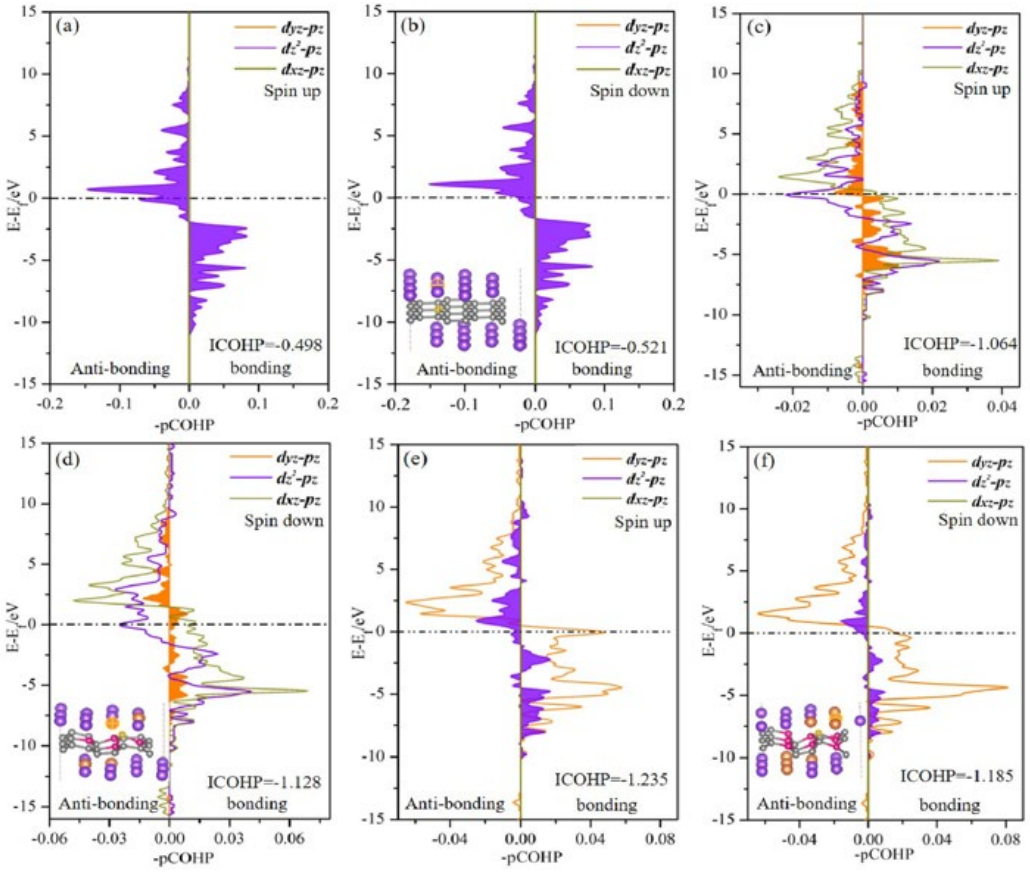

**Figure 21.** COHP (Crystal Orbital Hamilton Population) and Integrated COHP analysis of (a, b) the $Gr(B_0)$-$Ni(Cr_0)$ model, (c, d) the $Gr(B_4)$-$Ni(Cr_4)$ model, and (e, f) the $Gr(B_8)$-$Ni(Cr_8)$ model with the corresponding highlighted positions of Ni, Cr and C shown in the insets. Reproduced with permission.[148] Copyright 2022, Elsevier.

3.3. Topological defect

In materials science, a topological defect is a continuous but irreversible alteration of the internal structure of a material in some way, which is usually associated with breaking symmetry in the material.[121, 122] Stone-Wales defects are the most easily formed and typical topological point defects in graphene and carbon nanotubes, as they have the lowest formation energy compared to single- or double-vacancy defects.[40] Pristine graphene consists only of $sp^2$ hybridized state C atoms, and the physicochemical properties of the ideal graphene lattice such as chemical reactivity,[149] mechanical strength[150] and electron transport[151] etc., can be drastically changed by the presence of these topological defects. By generating specific defects in graphene nanomaterials in a controlled manner, desired specific functions can be achieved.[152]

Klein et al.[122] investigated the effect of topological defects such as Stone-Wales (S-W) on the graphene/Cu interface by constructing a molecular defect model and DFT calculations. **Figure 22**(a-c) show the independently optimized structures of ideal graphene lattice, embedded S-W defects and embedded 5-7 defects. The defect/metal interactions lead to a large amount of charge redistribution, and both defect structures exhibit additional strong localized charge transfer around the defects (Figure 22(d-i)). DFT can predict the interactions of a graphene-metal surface modified by induced defects. It also can predict how this modification affects the graphene-metal bond distances (Figure 22(j)). It has been shown that the S-W defects get the entire graphene lattice closer to the metal, shortening the bond distances,

increasing the interaction energy, enhancing electronic interactions, and significantly shifting the charge (Figure 22(e, h)). The difference in the interaction between the adsorption structure and bonding energy is essentially attributed to the difference in electronic structure. Investigations of the valence electron structure using ultraviolet photoelectron spectroscopy (UPS) shows that the monolayer azupyrene completely suppresses the surface state and the entire range between the Fermi energy ($E_F$ ). The Cu d-bands lead to an increase in intensity (exhibiting a completely different character than π-conjugated molecules physically adsorbed in the metal plane), confirming that hybridization of the molecular orbitals with the metal state in the presence of defects leads to an asymmetry of the C 1s peaks of the azupyrene (end-state effect[153]). Despite significant localized charge transfer, the interaction energy between graphene/Cu with Stone-Wales (S-W) defects increases by merely 6 kJ/mol over pristine graphene. This modest increase results from lattice distortion that impairs alignment, denying the benefits of enhanced bonding. Yet, this defect-driven boost in electronic coupling at the graphene/metal interface may still improve graphene-based electronic and optoelectronic device performance.

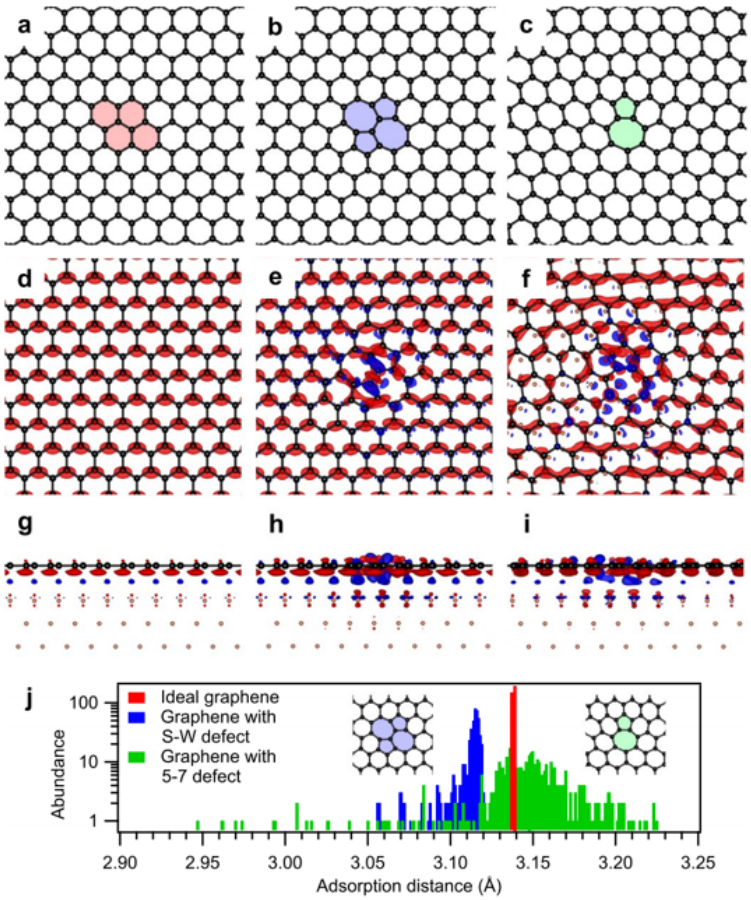


**Figure 22.** (a-j) Interaction of topological graphene defects with the Cu(111) surface. Reproduced with permission.[122] Copyright 2022, American Chemical Society.

However, the fact that the presence of defects is not necessarily favorable for bonding at the graphene/metal interface. Yang et al.[60] used first principles to determine the interfacial binding energies for three graphene/Ni models with defects, finding values of -91 meV, -41 meV, and -53 meV per carbon atom for Ni-GN-5-7-7-5 (S-W defects), Ni-GN-5-8-5, and Ni-GN-O2, respectively. These are significantly lower than the -150 meV per carbon atom for defect-free Ni-GN indicating that defects and oxygen content diminish the bond strength between Ni and graphene. Minimal electron transfer from Ni to defective graphene surfaces suggests that the interaction is weak, primarily due to electron polarization. Due to the presence of defects, the hybridized Ni and C orbital electrons at the interface of defective graphene and Ni are not as extensive and strong as those at the Ni-GN interface.

In conclusion, low-dimensional carbon nanostructures such as graphene, carbon nanotubes, and fullerenes, whether defective or defect-free, hold distinct significance. Devices based on strain extensively utilize graphene with defects. However, the primary influence of defective graphene is indirect, affecting electrical, optical, and vibrational characteristics rather than mechanical effects. The great influence of the presence of graphene defects on the properties of the graphene/metal interface has not only contributed to the great development of conventional graphene-reinforced MMCs (in the pursuit of higher mechanical properties), but also to a wider range of applications and research on functional MMCs (nanoelectronics, optoelectronics, sensing and energy storage applications).[113, 121, 122]

### 3.4. Stacking faults and nanotwins

Stacking faults (SFs) are planar crystal defects in metallic materials (FCC-type metals and alloys). Dissociation of <110>/2 full dislocations lead to the formation of two <112>/6 Shockley partial dislocations around the SFs, which not only reduces the mean free range of the sliding dislocations (by impeding dislocation motion) but also contributes to the accumulation of sliding dislocations (by acting as dislocation interactions and storage sites to facilitate dislocation accumulation). When dislocations meet stacking faults (SFs) on their slip plane, they may either segment or merge with them, creating new dislocations that either penetrate or cross-slip over the SFs.[154] These interactions need high activation stress enhancing the yield strength of the material. Furthermore, SFs can engage to form a Lomer-Cottrell (LC) lock through various mechanisms.[155] This typically results from the interaction of two leading partial dislocations on the close-packed surface, leading to the formation of cemented stepped dislocations on non-slip surfaces.[4] The cementation of these stepped-rod dislocations not only impedes dislocation motion but also serves as a Frank-Read source for further dislocation generation. Thus, akin to other planar defects like grain, twin boundaries, and heterogeneous interfaces, SFs concurrently increase both strength and plasticity in MMCs.[154, 156, 157]

The additional energy generated due to the formation of SFs zone is called staking fault energy

(SFE).[158] Since SFE represents the energy cost of shearing two atomic surfaces, and as SFs energy decreases, a higher density of deformation twins will form during stretching to take up the plastic deformation.[159] The magnitude of the SFE is related to the dislocation density, and increasing the dislocation density increases its effective SFE,[160] which in turn reduces the work-hardening ability of the composites.

For some pure metals or alloys with high levels of dislocation energy (e.g., Al), the formation of laminar dislocations or nanotwin crystals often requires harsh conditions such as low temperature or high strain deformation.[161] Recent studies have found that the presence of numerous heterogeneous interfaces in MMCs can promote the formation of layer dislocations and nanotwins in the metal matrix.[157, 162, 163] Yang et al.[164] discovered that the inclusion of SiC nanoparticles can encourage the creation of stacking faults in AMCs. They attributed the presence of these faults to the high density of nanointerfaces. Zhou et al.[157] found that the interfacial stresses due to the difference in CTE between two sides of the Al(Mg)/$Al_3Mg_2$ interface stimulate the emission of some dislocations at the interface, which promotes the formation of laminar dislocations inside the grains. Wu et al.[163] showed that the enrichment of Si atoms diffusing from the SiC/Al interface in the Al matrix reduced the SFE through first-principle calculations. As shown in **Figure 23**(a, b), Li[162] also found the SFE drastically decreases gradient elemental segregation towards the amorphous TiC interface, driven by residual stresses generated during laser powder bed fusion (LPBF) thermal cycling, resulted in low SFE and the formation of 9R-twin and transformation into nanotwins at the TiC interface with low SFE (Figure 23(d-e)).

In summary, the main reasons for heterogeneous interfaces to promote the generation of SFs and nanotwins can be attributed to two points; (1) Interfacial stresses generated during cooling and/or

straining processes promote partial dislocation emission,[29, 157] (2) Enrichment of heterogeneous elements reduces the SFE near the interface.[156, 162, 163, 165] Due to the localization of interfacial stresses, SFs mostly appear in the interface-affected zone (IAZ), and how to maximize the total amount of SFs in MMCs is a direction for future efforts.

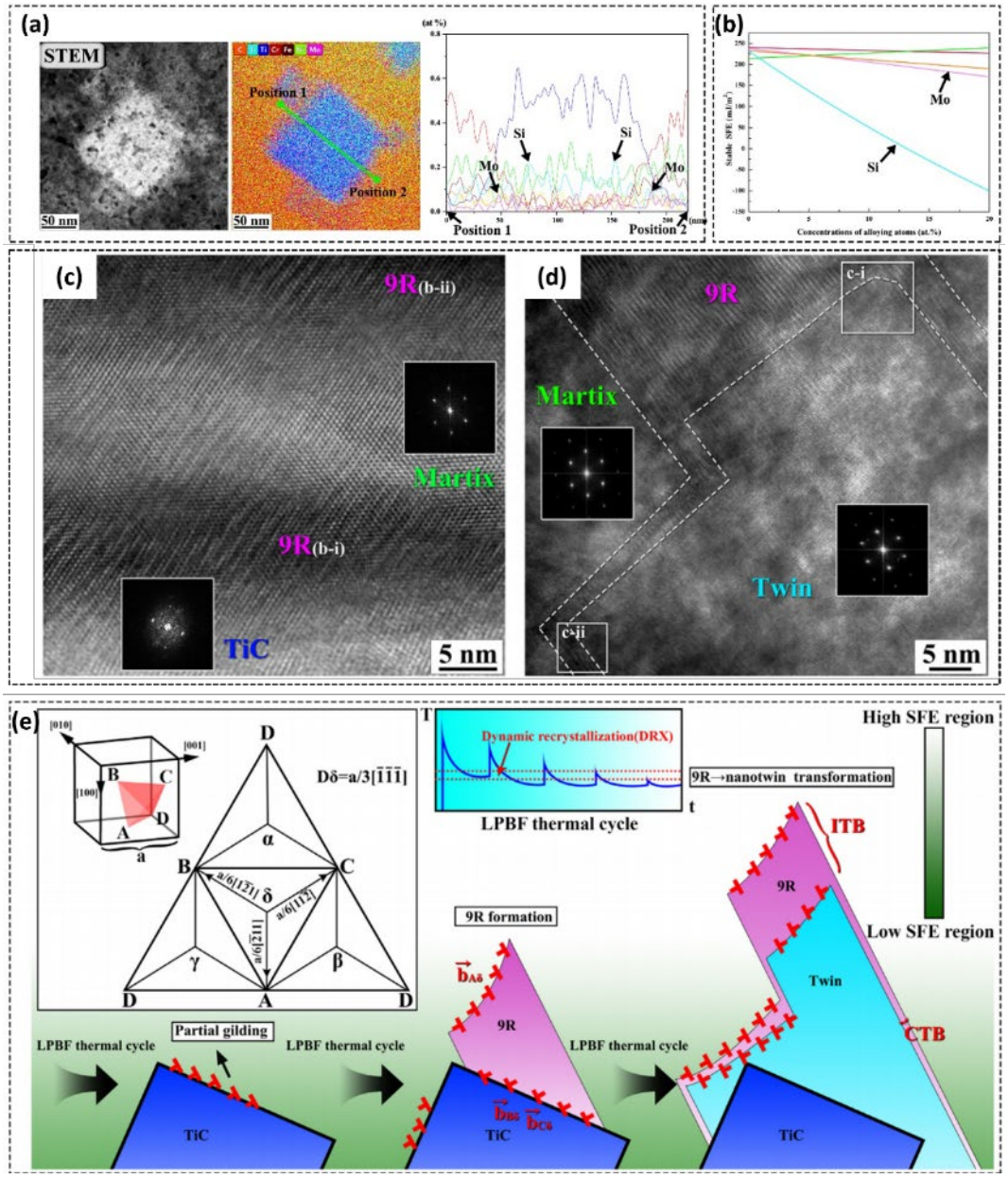


**Figure 23.** (a) STEM image and EDS line scanning of the TiC nanoparticles showing the concentrations changes of matrix elements in its vicinity. (b) The thermodynamic calculation diagram displaying the

influence of Si, Mo and other elements on the stacking fault energy of 316LSS. (c) HRTEM images showing discontinuous distorted 9R at the interface of TiC nanoparticle and matrix. (d) HRTEM images showing untransformed part perfect and imperfect 9R structure formation ITB and CTB, respectively. (e) The schematic of TiC nanoparticle inducing twin growth associated with dynamic recrystallization (DRX) during LPBF thermal cycling. Reproduced with permission.[162] Copyright 2022, Elsevier.

## 4. Thermodynamics and kinetics of interfacial reactions

The in-situ reaction strategy is capable of synthesizing fine-sized and uniformly dispersed nanoscale reinforcements in composites while generating a non-polluting and highly thermodynamically stable reinforcement/matrix interface,[70, 86, 105, 166-168] and thus are widely used in the preparation of MMCs. For in situ autogenously reinforced MMCs, the complex metal/reinforcement phase interface may undergo multiple chemical reactions,[86, 166, 168] which makes the traditional experimental trial-and-error type of study unreliable. Experimentally is challenging to characterize the thermophysical properties of the products generated by the interfacial reactions when they are small in scale. Any chemical reaction requires certain thermodynamic and kinetic conditions. Equilibrium thermodynamics can give the direction of the interfacial reaction transition, the magnitude of the driving force and the qualitative evaluation of the transition, while the kinetics gives the interfacial reaction rate and the influence of various physical and chemical factors on the chemical reaction rate. This makes the design of base alloys and reinforcing phases based on theoretical guidance.[35, 38, 169, 170]

To optimally design the ideal interface and minimize the inefficiencies and costs associated with conventional trial-and-error approaches is crucial to understand the chemically reactive nature of the interface. This includes the interfacial nucleation-growth characteristics, thermodynamic and kinetic mechanisms that provide strong theoretical guidance to regulate the interfacial reactions in designed

MMCs.

## 4.1. Reaction thermodynamics

### 4.1.1. Gibbs function criterion

The Gibbs function criterion is a key tool for understanding and predicting the spontaneity of chemical reactions. In the design of in-situ enhanced MMCs, the possibility of in-situ reactions occurring should first be explored, and only if the thermodynamic conditions for the reaction to occur are met then they can be extended to determine the reaction rate.[169] The Gibbs function is one of the thermodynamic functions of a reacting system, and the Gibbs free energy of a given system can be expressed as:[107]

$$G = H - TS \tag{4-1}$$

where $G$ denotes the Gibbs free energy of the reaction system, $H$ denotes the enthalpy of the system, $T$ denotes the reaction temperature, $S$ denotes the entropy of the system. Under isothermal and isobaric pressure, after the system changes from one state to another, the change of Gibbs free energy of the system $\Delta G$ can be expressed as:

$$\Delta G = \Delta H - T\Delta S \tag{4-2}$$

where $\Delta G$ is the Gibbs free energy variable of the system, $\Delta H$ is the enthalpy change of the system, and $\Delta S$ is the entropy change of the system. Thermodynamic studies show that whether a chemical reaction can take place in a system and the direction of the reaction can be determined by the Gibbs free energy variable of the system $\Delta G$. Under conditions of isothermal temperature and pressure and non-volumetric work, all changes that can occur automatically in a system are $\Delta G = 0$ (changes are reversible) and $\Delta G < 0$ (change proceeds spontaneously). In fact, since the reversible process is ideal when the $\Delta G = 0$ the

system is in equilibrium, only when $\Delta G < 0$ the process can occur. For a chemical reaction, the standard free energy change is given by:

$$\Delta G^0 = \sum v_i G_i \tag{4-3}$$

where $v_i$ is the stoichiometric coefficient of the monomer or compound, and $G_i$ is the free energy of the monomer or compound.

Interfacial reactions invariably involve the transfer of energy and mass.[107] The formation of new products at the interface impacts the bonding quality. Hence, understanding the mechanism of these reactions is crucial for steering them towards producing desirable outcomes. Here, a typical metal/ceramic interface in PRMMCs, i.e., the Al/$B_4C$ interface, is taken as an example. Although numerous studies have confirmed that the addition of Ti can improve the poor wettability and severe interfacial reactions at the Al/$B_4C$ interface,[171] an understanding is still missing regarding the thermodynamics of the reactions in the interfacial layer and the mechanisms behind the formation of products at the interface.[172] This was explored by Guo[172] using DFT calculations and thermodynamic analysis. The results summarized in **Figure 24**(a) show that the $\Delta G$ of reaction (3) and reaction (4) are more negative than those of reaction (1) and reaction (2), indicating that the interfacial reactions involving Ti are thermodynamically more favorable. The $\Delta G$ of chemical reactions at 720 ℃ are shown in Figure 24(b), in all reactions besides reaction 1, the Gibbs free energy change ($\Delta G$) values are negative, suggesting their theoretical spontaneity. Specifically, reaction (4) exhibits a $\Delta G$ of -939.68 kJ/mol-atom, highlighting its superior spontaneous potential. Thus, the optimal reaction pathway in the Al-Ti-$B_4C$ system is identified as: $6Al + 3Ti + 2B_4C \rightarrow 2Al_3BC + 3TiB_2$. Wang[173] attempted to inhibit the severe interfacial reactions between elements such as Ni, Fe and Co and SiC in SiC-reinforced high temperature alloy matrix composites by

alloying methods. The effect of elements such as Cr and Mo on the activity of Ni was calculated by Thermo-Calc. The reactive Gibbs free energy of the Ni element can be expressed as [174]:

$$\Delta_r G = \Delta_r G^0 - v_{\mathrm{Ni}} RT \ln a_{\mathrm{Ni}} \tag{4-4}$$

of which $\Delta_r G$ and $\Delta_r G^0$ are the Gibbs reaction free energies before and after alloying, respectively, $R$ is the gas constant, $T$ is the reaction temperature, $a_{\mathrm{Ni}}$ is the activity of Ni, and $v_{\mathrm{Ni}}$ is the stoichiometric constant of the chemical reaction. The $a^*_{\mathrm{Ni}}$ at $\Delta_r G = 0$ is called the critical activity, when $a_{\mathrm{Ni}} < a^*_{\mathrm{Ni}}$ ,the reaction will be completely inhibited, otherwise the reaction tendency still exists. Calculations showed that even in the 80Cr20Ni and 80Mo20Ni alloys, the activity of Ni still exceeds the critical activity $a^*_{\mathrm{Ni}}$, i.e., it is thermodynamically difficult to completely inhibit the reaction between Ni and SiC by alloying.

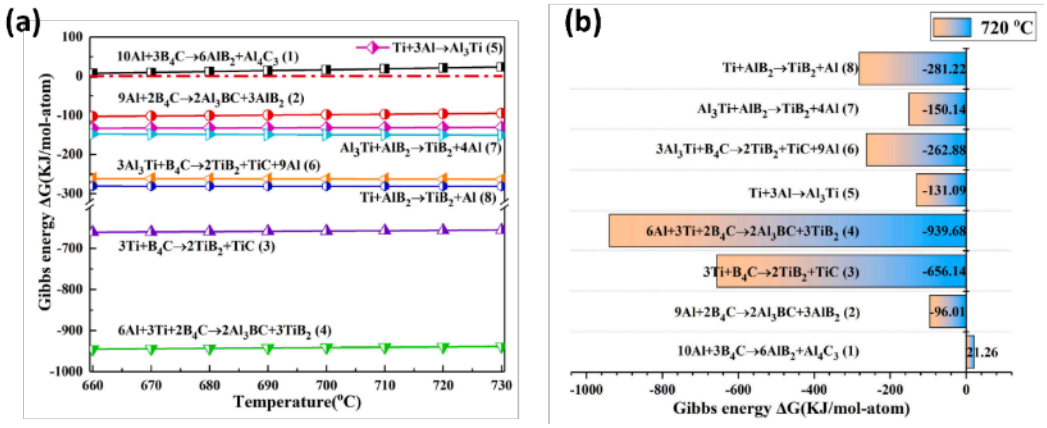


**Figure 24.** (a) Gibbs energy for each reaction at finite temperature; (b) Gibbs energy of different reactions at 720 ℃. Reproduced with permission.[172] Copyright 2022, Elsevier.

Segregation is a common phenomenon in metallic materials such as alloys. Solute atoms (Zn, Mg, and Cu, etc.) tend to segregate at grain boundaries to reduce the free energy of the system,[175] which favors the formation of earlier Guinier-Preston (GP) zones at grain boundaries instead that within the grain. The in-situ synthesis reinforcement/matrix interface belongs to a type of facet defects and is likewise an ideal location for elemental segregation. Numerous studies have shown that solute

segregation at grain and phase boundaries affects the interfacial bond strength.[65, 120] In MMCs, the control of the size of in-situ interfacial reaction products (e.g., in situ generation of ceramic phases, carbides, etc.) and the improvement of interfacial properties through elemental interfacial segregation and precipitation phase segregation have gradually attracted attention. Alloying element segregation at the reinforcement/matrix interface exhibits selectivity. For example, Wang et al.[120] observed that Fe atoms at the $MgAlB_4$/Al interface along the $\{10\bar{1}0\}$ planes result in significantly lower system free energy compared to that of the $\{0001\}$ planes, Fe atoms thus are more inclined to segregate at the $\{10\bar{1}0\}_{MgAlB_4}$/Al interface.

4.1.2. Interfacial energy and work of adhesion

Due to the irregular arrangement of atoms on the grain boundaries, a point distortion is produced, causing an elevation of energy, which is called the interface energy.[176-178] The formation of metal/ceramic interfaces is driven by free energy reduction upon close contact between metal and ceramic surfaces.[179] This reduction governs the atomic structure of the interface, aligning dense packing planes and orientations of the metal, ceramic, and reaction products parallel to the interface.[169] The change in energy $\Delta G$ per unit area of the interface formed can be expressed as:

$$\Delta G = \gamma_{\mathrm{m}} + \gamma_{\mathrm{c}} - \gamma_{\mathrm{mc}} \tag{4-5}$$

of which $\gamma_{\mathrm{m}}$ and $\gamma_{\mathrm{c}}$ are the surface energies of the metal and ceramic, respectively, $\gamma_{\mathrm{mc}}$ is the metal/ceramic interfacial energy. The ideal work of adhesion is defined as the reversible work required to separate the interface into two free surfaces. If only chemical bonding occurs at the interface and no plastic deformation of the metal or ceramic occurs at the time of interfacial separation, the change in

energy $\Delta G$ is the same as the work of adhesion $W_{\mathrm{ad}}$. The above equation can be rewritten as:

$$\gamma_{\mathrm{mc}} = \gamma_{\mathrm{m}} + \gamma_{\mathrm{c}} - W_{\mathrm{ad}} \tag{4-6}$$

The interfacial energy $\gamma_{\mathrm{mc}}$ increases as the interfacial adhesion work $W_{\mathrm{ad}}$ increases, so improving interfacial bonding (increasing $W_{\mathrm{ad}}$) will result in a decrease in interfacial energy. Metal-oxygen conformational interfaces are often more stable than metal-metal conformational interfaces. First-principles calculations of $Ni_3Ti/Al_2O_3$ interfaces show that the interfacial energy of Ni&Ti/Al1 and Ni&Ti/Al2 interfaces can vary in the range from 2.84 to 5.66 J/m$^2$,[38] which is much larger than that of Ni&Ti/O interfaces (1.49-2.55 J/m$^2$ ), suggesting that the bonding strength of Ni&Ti/O interfaces is higher than that of Ni&Ti/Al interfaces. Because of this, the internal oxidation effect with high thermodynamic driving force is a common strategy to improve the metal/reinforcement interfacial bonding in in-situ reinforced MMCs;[86] this will be described in detail in chapter 4.2.

### 4.1.3. Interfacial wetting behavior

MMCs systems commonly used in engineering applications are often multi-component complex systems involving stir casting,[172, 180, 181] squeeze casting,[182] vacuum pressure impregnation (unpressurised spontaneous infiltration, low-pressure infiltration or high-pressure infiltration),[183] liquid phase sintering for powder metallurgy.[184] The essence of these in-situ autogenous composite preparation processes for MMCs is the self-generation of reactive phases as reinforcement of composites through chemical reactions between elements within the liquid phase metal melt. In the preparation of discontinuously reinforced MMCs by these liquid-phase method, the wettability of the metal/ceramic interface is particularly important, which not only determines the degree of dispersion of the solid-phase

ceramic in matrix and the strength of interfacial bonding, but also determines the difficulty in the preparation of the composites ultimately affecting the material properties.[185-187] Investigating the wettability of metal/ceramic interfaces is crucial for advancing in the MMCs development. However, assessing these characteristics at elevated temperatures presents challenges due to the high melting points of alloys, low viscosities, and chemical reactivity.[188]

Currently metal/ceramic wettability is obtained by measuring the contact angle $\theta$ (calculated with the help of Young′s equation):

$$\cos\theta = \frac{\gamma_s - \gamma_{s/l}}{\gamma_l} \tag{4-7}$$

where $\gamma_s$ is the surface energy of the solid phase being wetted, $\gamma_{s/l}$ is the surface tension between the solid matrix and the liquid, $\gamma_l$ is the surface tension of the liquid, and $\theta$ is the solid-liquid interface contact angle. Therefore, a higher surface energy is required to obtain better wettability ($\gamma_s$ ). Among high-temperature wetting mechanisms, dissolution, adsorption, and reaction-driven wetting, the latter is the most crucial. For instance, introducing surface-active elements like sulfur or oxygen to iron-based alloys reduces surface tension and improves molten metal/ceramic wetting behavior.[189] The low surface energy of BN nanotubes (~27 mN/m) results in low wettability at the molten Al/BN interface, but when the interfacial reaction between Al and BN occurs, the extremely high surface tension (~660 mN/m) created results in good wettability of BN nanotubes in molten Al (**Figure 25**(a)).[187] As shown in Figure 24(b1), Fu[190] calculated the $W_{\mathrm{ad}}$ of Cu/graphite, Cu/TiC and Ti-adsorption interfaces with first-principle calculations. $W_{\mathrm{ad}}$ values of reacted interfaces are much higher than unreacted interfaces. Additionally, the adoption of Ti enhances the interfacial bonding with the hybridizations of Ti-d and C-p at ~ -2 eV, and Ti-p and C-p at ~ -3 eV (Figure 24(b2-b7)). Therefore, rather than simply adsorbing at the melt/graphite

interfaces, the addition of Ti is more effective in improving the wettability of Cu on graphite when it reacts with graphite to form TiC.

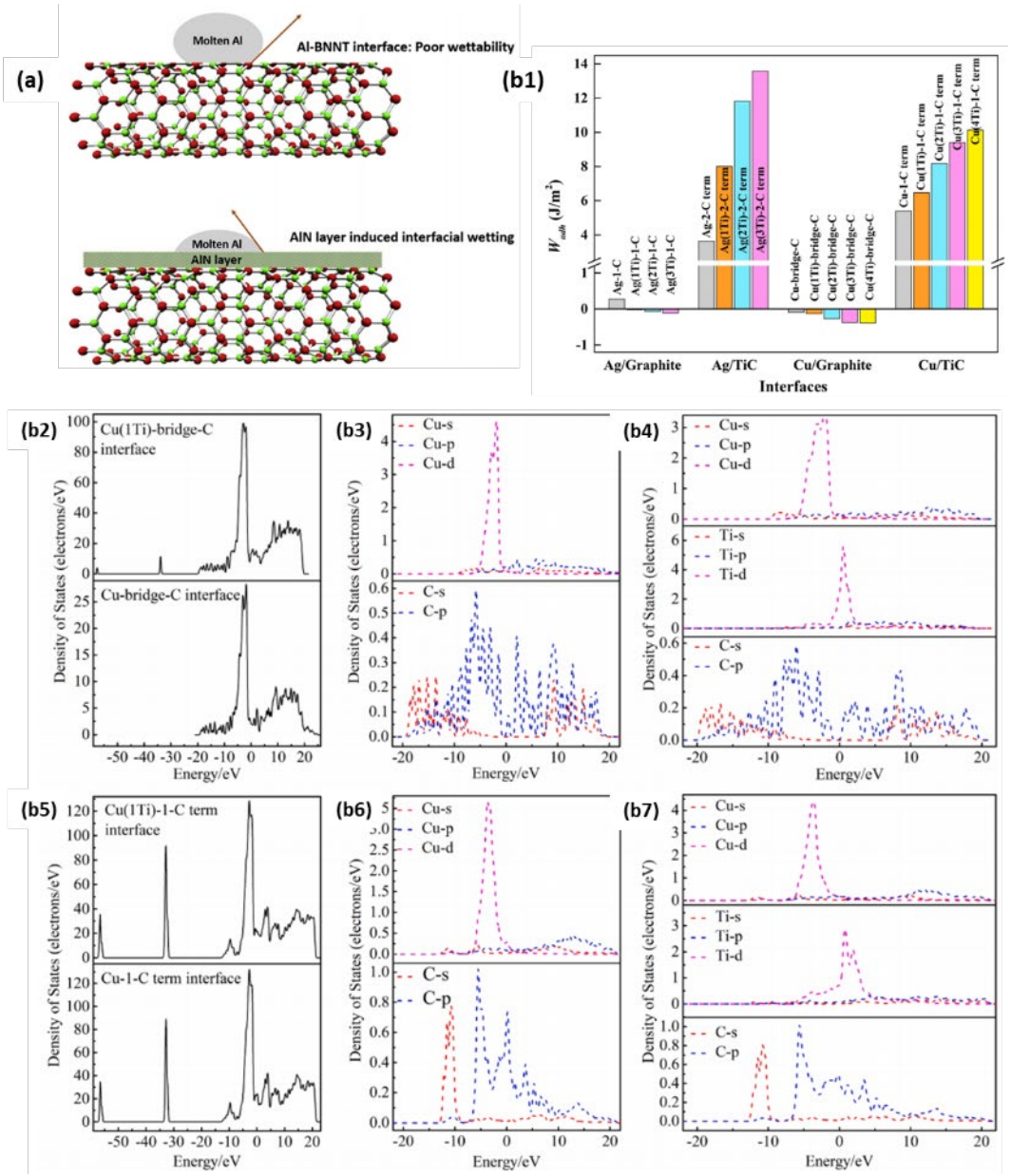


**Figure 25.** Interfacial reactions are effective in improving wettability. (a) Schematic representation of AlN induced wetting of BNNT by molten Al. Reproduced with permission.[187] Copyright 2017, Elsevier. (b1) Work of adhesion ($W_{ad}$) of Ag/graphite, Ag/TiC, Cu/graphite, Cu/TiC and Ti-adsorption interfaces; Density of state results of Cu/graphite and Cu/TiC interfaces. totals DOS of (b2) Cu/graphite and (b5) Cu/TiC and corresponding Ti-adsorption interfaces, PDOS results of (b3) Cu/graphite (b4) Cu(1Ti)/graphite (b6) Cu/TiC (b7) Cu(1Ti)/TiC. Reproduced with permission.[190] Copyright 2023,

Elsevier.

### 4.2. Reaction kinetics

Reactive sintering has been widely used as an in-situ reaction strategy for the preparation of AMCs.[166, 191, 192] The process of reactive sintering involves a thermite reaction between Al and metal oxides to produce in-situ aluminum oxide ($Al_2O_3$) and intermetallic compounds as reinforcements in AMCs. This approach is valued for its ability to create fine, evenly distributed reinforcements within composites, ensuring a clean interface with the matrix and exhibiting high thermodynamic stability. Any chemical reaction requires certain thermodynamic and kinetic conditions. It has been shown that controlling the thermodynamics and kinetics of interfacial reactions through matrix alloying,[86, 172] surface modification of reinforcements,[33] and improvement of the preparation process can inhibit the generation of deleterious interfaces and obtain beneficial functional interfaces.

On the one hand, although the energy changes of interfacial reaction systems satisfy the thermodynamic conditions, the kinetic conditions are often not satisfied due to the in-situ reaction process or process parameters, and thus the expected reaction products are not obtained. For example, the limited interfacial contact between the different composite powders, or the high activation energy of solid-state diffusion, restricts the exchange of substances between the reactants, making it difficult to carry out in-situ reactions. On the other hand, due to the limited solid-state diffusion coefficients, the in situ solid-phase reaction is often confined to the reactant interfaces.[193] Temperature is one of the main factors affecting the interfacial reaction rate, and the difference in the thermal effect of interfacial reaction will be reflected in the difference in the microstructure after the reaction. Furthermore, the strong thermal effect will accelerate the diffusion of elements promoting the nucleation and growth of interfacial and

intracrystalline reaction products, affecting the microstructure of the matrix (e.g., causing grain coarsening).[86, 194]

### 4.2.1. Distribution regulation of products of in-situ interfacial reaction

Intragranular in-situ nanoparticles are able to hinder dislocations and aggregate high-density dislocations within the grain, thereby greatly enhancing the strength and plasticity of MMCs.[86] Rong et al.[166] aimed to enhance the diffusion rate of elements via the intense thermal effect produced by the thermite reaction between Al and CuO achieving a uniform dispersion of $Al_2O_3$ nanoparticles within the Al grains using a diffusion-assisted nucleation mechanism (**Figure 25**(a)). Thermite reaction exotherm is mainly from the chemical reaction at 893 K:[195]

$$2Al + 3CuO \rightarrow Al_2O_3 + Cu;\ \Delta H = -1170kJ/mol(Al_2O_3/mol) \quad (4\text{-}19)$$

The intense thermal effect from the substitution reaction between Al and CuO significantly enhances the thermodynamic driving force for the ongoing in-situ reaction of Al-CuO composites during hot pressing. This allows O and Cu atoms at the reactive interface to persistently diffuse into the Al matrix, bonding with Al atoms to create intracrystalline $Al_2O_3$ and $CuAl_2$. In addition, due to the smaller atomic radius of the O atoms and the interstitial diffusion mechanism, the O atoms have larger diffusion coefficients in Al than in Cu. Thus, the diffused O and Al atoms may react and nucleate near the $CuO/Cu_2O$ particles or grow together with the formed $Al_2O_3$ to eventually form $Al_2O_3$ particles or whiskers. During the above sintering reaction, grain boundary migration will greatly occur during the Al grain coarsening process; and $Al_2O_3$ is likely to move from the grain boundary to the intragrain to achieve intragranular distribution. Likewise, in the sintering process of Cu-0.8Al and $Cu_2O$ composite powder

(Figure 25(b)),[86] the diffusion rate of O atoms within the Cu matrix significantly exceeds that of Al atoms under the influence of the thermodynamic driving force from internal oxidation.[196] On one hand, this allows the O and Al atoms to diffuse from $Cu_2O$ into the Cu-0.8Al powder meeting at the reaction front inside the Cu matrix to nucleate inside the Cu grains. On the other hand, the rapid coarsening of $Al_2O_3$ nanoparticles is greatly inhibited by this kinetic bottleneck, which maintains a remarkably uniform and homogeneous distribution of ultrafine sizes.[84]

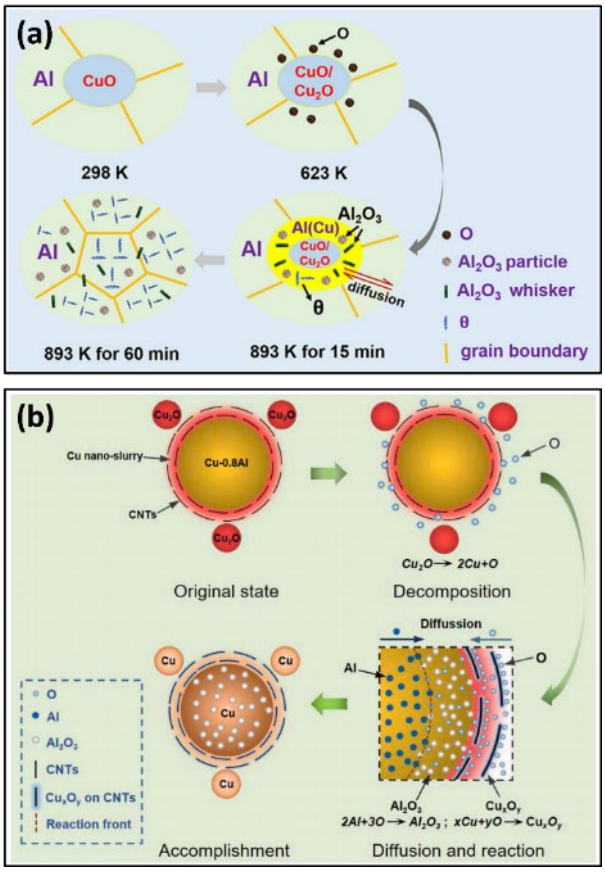


**Figure 26.** (a) The schematic of reaction mechanism for the Al-5CuO composite during sintering. Reproduced with permission.[166] Copyright 2021, Elsevier. (b) The schematic illustration of oxygen diffusion and in-situ solid-reaction for Cu-$Al_2O_3$-CNTs during internal oxidation. Reproduced with permission.[86] Copyright 2022, Elsevier.

4.2.2. Degree regulation of interfacial reactions

Despite the fulfillment of kinetic conditions, the excessive reaction heat of some reaction systems can make the reaction process difficult to control, and inappropriate process parameter settings can lead to overly vigorous interfacial reactions, which can deteriorate the interfacial properties.[8, 78] In such cases, appropriate measures must be taken to slow down the interfacial reaction.[78] The interfacial reaction process is controlled by diffusion, and the differences in diffusion coefficients of different elements in different substances, diffusion directions (parallel or perpendicular to grain and/or phase boundaries), diffusion temperatures and diffusion times, and other factors affecting diffusion behaviors will significantly influence the morphology and growth kinetics of interfacial products.[35, 194, 197] The varied growth patterns of products from the interfacial reaction can significantly alter morphology of the interface. When considering how these interfacial reaction products impact the strength and mechanical characteristics of the interfaces, factors such as bonding strength, preferential orientation, and growth defects in the relationship between the metal matrix become crucial. These aspects are intimately linked to the mesoscopic mechanical behavior and extend beyond the usual considerations of content, size, and morphology.[10, 33, 198]

1) Nucleation rate

As an example, the formation mechanism of the classical interfacial reaction product $Al_4C_3$ in nanocarbon-enhanced AMCs has been extensively studied.[13, 115, 198, 199] So far, there are two formation mechanisms for carbide formation, (1) nucleation and (2) epitaxy. In the nucleation mechanism, the carbons nucleate at the nanocarbon, which acts as a carbon source. In the epitaxy mechanism, the nanocarbon lattice serves as a template for metal atoms to diffuse into the nanocarbon through defects leading to the direct conversion of the nanocarbon to carbide. Corresponding to these two mechanisms,

the growth of carbide will show nucleation-growth and epitaxial growth modes, respectively.[198] Although the growth of $Al_4C_3$ is closely related to the diffusive behavior, the post-nucleation growth is always rod-like (with variations in the aspect ratio) unlike the oriented growth of the second phase in the alloy, which usually leads to a different phase morphology (rods, needles, flakes, etc.).[200] This suggests that the $Al_4C_3$ growth morphology is not influenced by the $Al_4C_3$/Al interface. With the gradual deepening of the study, it was found that the growth of the $Al_4C_3$/Al crystal structure and the diffusion rate along the typical C-axis $\langle 11\bar{2}0 \rangle$ is faster than that in the radial $\langle 0001 \rangle$. The faster diffusion rate along the typical C-axis than the radial C-axis leads to the growth of $Al_4C_3$ in the rod orientation.[201] The growth rate of $Al_4C_3$, results from a diffusion-controlled interfacial reaction of Al and C atoms and can be determined using the following expression:[202]

$$\frac{d_A}{d_t} = \left(\frac{A_0}{2t} exp\left(\frac{-Q}{RT}\right)\right)^{1/2} \quad (4\text{-}8)$$

where $A$, $t$, $A_0$ and $Q$ denote the generation amount, retention time, constant and activation energy, respectively. It is clear that the growth rate of $Al_4C_3$ increases with increasing high temperature and decreases with increasing the time at high temperature. Diagrams of $Al_4C_3$ nucleation on the sidewalls of CNT and planar GNR edges are shown in **Figure 27**.[198]

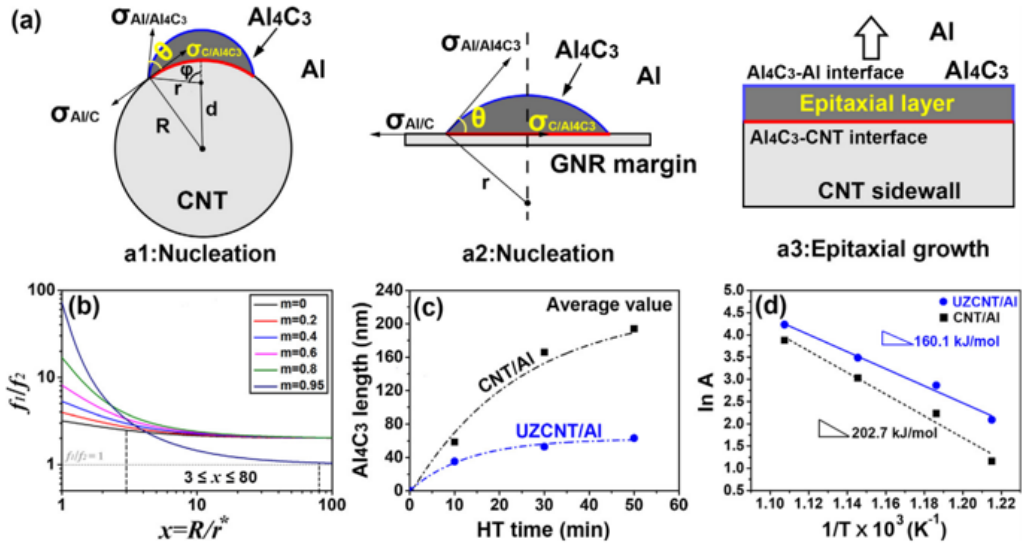


**Figure 27.** Schematic illustration of heterogeneous nucleation of $Al_4C_3$ on (a1) the sidewall of CNT and (a2) planar GNR margin, (a3) epitaxial growth of $Al_4C_3$ on the sidewall of CNT. (b) Plot of the value of $(f_1/f_2)$ versus the relative CNT radius $x = \frac{R}{r^*}$ by setting various m values. (c) the statistical average length of $Al_4C_3$ in the composites as a function of HT time at 873 K. (d) plot of ln A versus 1/T. Reproduced with permission.[198] Copyright 2022, Elsevier.

2) Growth rate

Due to the lower generation free energy of the Ti/C system (184 kJ mol at 298 $K^{-1}$ [203]), severe and uncontrollable interfacial reactions between Ti matrix and nanocarbon are commonly observed in the field of research on nanocarbon-enhanced TMCs.[33, 35] This results in the generation of TiC reaction products in the interfacial region and reduces the load transfer effect at the interface. In Al-Ti-C system, the explosive nucleation of TiC induced by the rapid increase in melt temperature also leads to the inability of the Al melt to cover completely the agglomerated ceramic particles. Furthermore, the continuity of the Al/TiC interface is disrupted, resulting in the inevitable appearance of porosity in the agglomerated ceramic particle region.[78] The evolution of the TiC morphology of the C/Ti interfacial reaction products for 120s, 300s and 600s from ex-situ heating experiments at 1123K is shown in **Figure 28**(a1-a3).[33] The

TiC layer gradually grows from the initial irregular particles in a directional manner along the C/Ti interface to form a continuous dense layer. This suggests that prior to the establishment of a continuous TiC layer, carbon atoms preferentially diffuse into the Ti substrate at both, the TiC microcrystals/Ti interface and the Ti substrate area near the C/Ti interface. Thus, there is not migration through the TiC microcrystals into the Ti substrate. The formation and bonding mechanisms at the interfaces of Al-Ti-C and Al-Ti-$B_4C$ systems are shown in Figure 28(b).[78] The Al-Ti-$B_4C$ system exhibits lower reaction intensity, and it is less exothermic than the Al-Ti-C system. The higher stability of $B_4C$ and the longer diffusion paths required for C and B elements to intermix result in a dampened reaction intensity and slower growth rate of ceramic particles within the metal matrix during synthesis. In the Al-Ti-$B_4C$ system, TiC and $TiB_2$ particles form slowly and steadily between $TiAl_3$ and $B_4C$. Due to the favorable high-temperature wettability of Al with the ceramic particles, TiC and $TiB_2$ are evenly spread and fully enveloped by the Al melt resulting in a cohesive and well-wetted ceramic/metal interface. Liu et al.[35] attempted to slow down the GNPs/Ti interfacial reaction by using B film modified GNPs and gave a detailed growth kinetic analysis of $TiB_w$. The interfacial reaction between a nanoscale B film on the surface of GNPs and Ti matrix is shown in Figure 28(c1-c6). B atoms diffuse through $TiB_w$ and react with Ti atoms at the $TiB_w$/Ti interface as follows:

$$B(diffusing) + Ti(surface) = TiB_w \tag{4-9}$$

The development of the TiC layer stems from the reaction diffusion at the interface between the Ti matrix and B-GNPs. The diffusion flux $J$ for chemical diffusion (the diffusion of C atoms through the TiC interface towards the Ti side) in the TiC layer can be expressed as:

$$J = -D \cdot S\frac{C_2 - C_1}{y} = -D \cdot S\frac{\Delta C}{y} \tag{4-10}$$

where $D$ is the diffusion coefficient of C atoms in the chemically reactive layer, $S$ is the contact area, and $C$ is the concentration of C atoms. The calculation results of activation energy of TiC growth inferred that the dense B-film-modified GNPs significantly slowed down the reaction tendency at the GNPs/Ti interface.

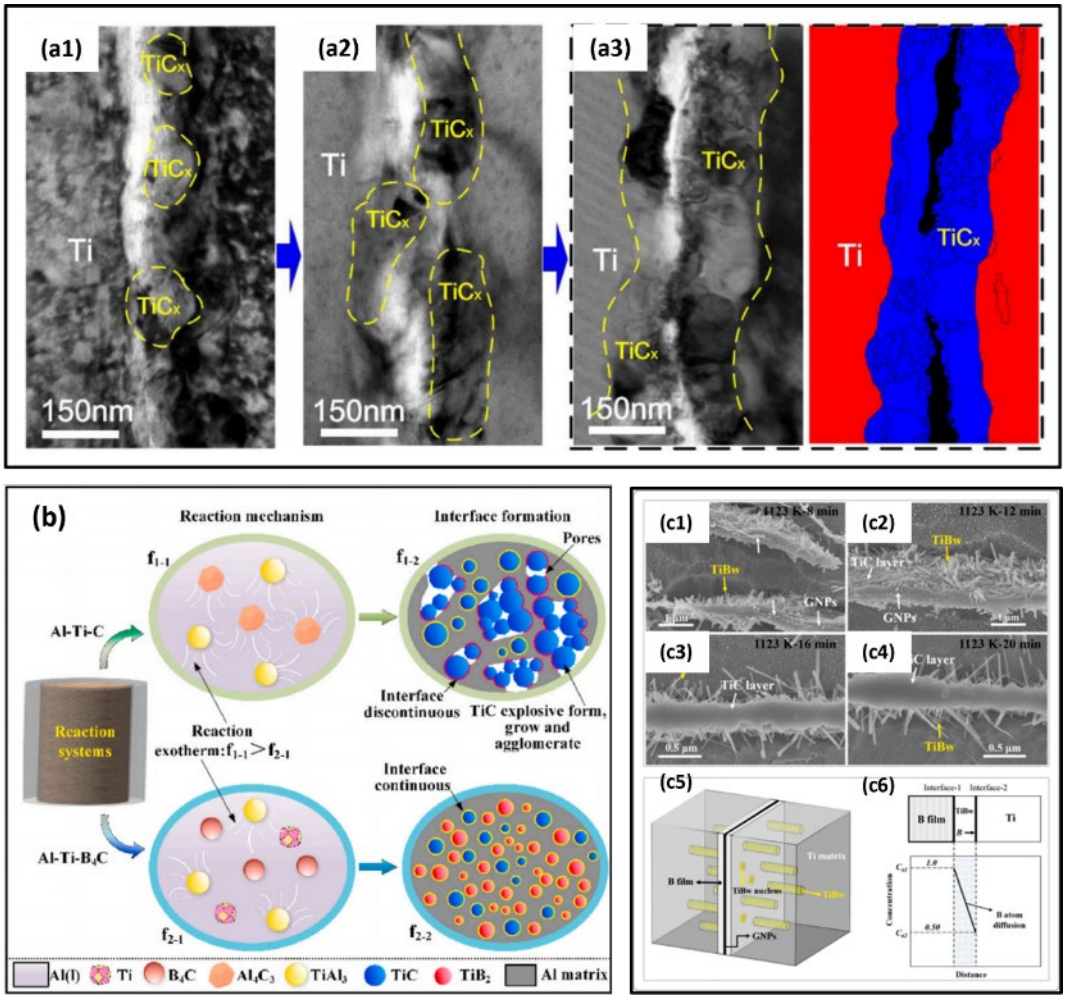


**Figure 28.** (a) Sequence of TEM micrographs of the in-situ $TiC_x$ layer growth in HT 1123K samples: (a1) 120s; (a2) 300s; (a3) 600. Reproduced with permission.[33] Copyright 2021, Elsevier. (b) Schematic diagram of interface formation in the Al-Ti-C and Al-Ti-$B_4$ C systems, respectively. Reproduced with permission.[78] Copyright 2021, Elsevier. (c) Interfacial morphologies of $TiB_w$ @GNPs/Ti composites after B-GNPs/Ti billets being heat treated (HT) at 1123 K for different times: (c1) 1123 K-8 min, (c2) 1123 K-12 min, (c3) 1123 K-16 min and (c4) 1123 K-20 min, (c5) illustration of the interfacial interaction between B coating and Ti matrix; (c6) reaction equation: B(diffusing)+Ti(surface) = $TiB_w$. Reproduced

with permission.[35] Copyright 2022, Elsevier.

### 4.3. Thermodynamics and kinetics modeling of interfacial reactions

In multi-component complex metal matrix composite systems, the elements involved in the interfacial reaction will inevitably be affected by other components: the type and content of other components will affect their activity, the interaction coefficients between the components and thus affect the reaction of the final formation of self-generated reinforcing phases. It is necessary to establish corresponding thermodynamic and diffusion kinetic models for the interfacial reaction process to achieve theoretical guidance and controllable design of the interface. So far, in the theoretical design of in-situ autogenous reinforced MMCs, thermodynamic and kinetic parameters (including the Gibbs free energy change of the autogenous reaction of the reinforced phase, the change of reaction enthalpy, and the diffusion coefficient) are often calculated by simple chemical equilibrium equations of pure matrix and single element basis to determine the plausibility/conditions to occur (temperature, etc.) and the nucleation/growth rate of interfacial reaction products. However, MMCs systems commonly used in engineering applications are often multi-component complex systems involving stir casting,[172, 180, 181] squeeze casting,[204] vacuum pressure impregnation[184] and liquid phase sintering for powder metallurgy.[184] The essence of these in-situ autogenous composite preparation processes for MMCs is the self-generation of reactive phases as reinforcing phases of composites through chemical reactions between elements within the liquid phase metal melt.

#### 4.3.1. Activity

The activity of the components in the melt is one of the main thermodynamic properties of metal

melts, which affects the melting, casting, and solidification processes as well as the final properties of the material. It is mainly used to predict and analyze the thermodynamic behavior of the components in the melt, which is particularly useful in the interfacial reaction mechanism of MMCs. Among the various theoretical models for predicting the activity, the most successful ones so far are based on the Miedema equation.[205] The Miedema model is used to predict the enthalpy of formation (formation energy) of metal alloys, especially for those metal alloys that cannot form compounds. The model evaluates the energy change when different metal elements combine to form an alloy based on factors such as atomic size, electronegativity, and electron density. Based on the Wilson equation[206] and the Miedema model,[205] Fan[170] proposed a method for calculating the activity of the alloy which has been demonstrated to be reliable from comparison with experimental values. The activity coefficient $\gamma_i$ of component $i$ in an infinitely dilute solution $j$ can be expressed as:

$$\ln \gamma_i^{x_i \to 0} = \frac{\alpha_{ij} f_{ij} [1 + u_i(\varphi_i - \varphi_j)]}{RTV_j^{2/3}} \tag{4-11}$$

where $x_i$ denotes the molar fraction of the component in the melt $i$, $\alpha_{ij} = x_i \times \gamma_i$ denotes the concentration of the component $i$ in an infinitely dilute solution $j$, $f_{ij}$ denotes an empirical parameter representing the interaction strength between component $i$ and $j$, $u_i$ denotes the electronic structure parameter associated with the component $i$, $\varphi$ denotes the electron density, $R$ denotes the gas constant, $T$ denotes the temperature of the melt, and $V$ denotes the molar volume. Fan et al.[170] predicted the effects of different alloying elements on the activity coefficients of Al and Si in high-temperature melts of Al-Si alloys at different temperatures and different compositional concentrations based on the established model for calculating the activity of the components in multivariate alloying melts, and deduced the effects of alloying element additions on the stability of the interfacial reaction between SiC particles and molten Al.

Therefore, based on the guidance of material thermodynamics, alloying elements can be targeted to effectively control the interfacial reaction between the reinforcing phase and the matrix.

#### 4.3.2. Diffusion coefficient

The migration of atoms (or molecules) through a medium due to thermal movement is called diffusion.[107] Diffusion is the only pathway for mass transfer in solids and is an important process factor influencing the microstructure and final properties of materials. The diffusion coefficient (also known as the diffusion constant) is a physical quantity that measures the rate of diffusion of a substance into another substance. It is a key parameter in Fick's first law, which describes the process of diffusion, and expresses the amount of material that passes through a unit area (perpendicular to the direction of diffusion) in a unit of time.[207] The unit of the diffusion coefficient is usually $m^2/s$ when the concentration gradient is a unit value. The study of diffusion at heterogeneous interfaces with molten metals is an important element in the field of material dynamics and plays a decisive role in the generation of reinforcing phases of in-situ autogenous metal MMCs. Currently, the main theoretical calculation models for the diffusion coefficient are the classical diffusion theory,[207] the Stokes-Einstein relation and its empirical extension,[208, 209] hard-sphere theory and its extended model etc.[210]

##### 4.3.2.1. Fick's law of diffusion

Classical diffusion theory based on Fick's first and second laws[207] describes the diffusion process under temperature and concentration gradients. This approach is usually used for simple diffusion cases but may not be accurate enough for fast dynamic processes in liquid metals. Fick's first and second laws are given below:

$$J = -D\frac{\partial c}{\partial x} \tag{4-12}$$

$$\frac{\partial c}{\partial t} = \frac{\partial}{\partial x}(D\frac{\partial c}{\partial x}) \tag{4-13}$$

where $J$ denotes the diffusion flux in the direction of the concentration gradient, and the scaling factor $D$ is the diffusion coefficient, $\frac{\partial c}{\partial x}$ is the concentration gradient, the negative sign indicates that the direction of diffusion is opposite to the direction of the concentration gradient, and $\frac{\partial c}{\partial t}$ denotes the change in concentration with time.

4.3.2.2. Stokes-Einstein equation and its empirical extension

The Stokes-Einstein relation considers the diffusive behavior of particles in fluids, especially in viscous media, which is particularly useful for diffusion calculations of larger particles in liquid metals, but the lack of data related to the viscosity of metals and their alloys, as well as the framework of purely metallic fluids, limits the application of the Stokes-Einstein equation.

$$D = \frac{k_B T}{6\pi\eta r} \tag{4-14}$$

where $D$ denotes the diffusion coefficient of the particle, $k_B$ denotes the Boltzmann constant, $T$ denotes the absolute temperature, $\eta$ denotes the solution viscosity, and $r$ denotes the particle radius.

4.3.2.3. Hard-sphere theory and its extended model

The application of hard-sphere theory to binary liquid alloys has been well documented. Schwitzgebel et al.[210] proposed the hard-sphere theory to calculate the group elements under a binary liquid ideal system $i$ of the self-diffusion coefficient:

$$D_i = \frac{l_i}{2}(\frac{\pi RT}{M_i})^{1/2}\frac{C(\eta)}{Z_x - 1} \tag{4-15}$$

where $l_i$ denotes the atomic radius, $M_i$ denotes the molar mass, $Z_x$ denotes the compression factor, $C(\eta)$ denotes a correction factor for the dependence on the convergence set rate $\eta$.

## 5. Numerical simulation

Understanding the intrinsic connection between interfacial microstructure and interfacial properties is crucial for designing MMCs with current and future bionic configurations. However, the conventional trial-and-error approach requires meticulous sample preparation, characterization of interfacial microstructure, and performance testing, which makes the whole process cumbersome and inefficient. The extreme complexity of the interfacial microstructural features (composition, orientation, defects, and strain states, etc.) makes it challenging to explore their effects on composite properties through traditional experimental methods.

The swift advancement of computer technology has significantly enhanced computational research and demonstrated substantial advantages in investigating the microstructural changes in material systems. Since the parameters of thermal/kinetic computational models are often optimized by fitting them to experimental values, they lack of a strong physical basis.[170] Instead, First-principle DFT calculations are able to predict the enthalpy/entropy of formation of the compounds involved in thermal/kinetic calculations.[39, 82, 211] MD simulations can predict atomic diffusion coefficients at heterogeneous interfaces[43] (**Figure 29**). The Phase-Field (PF) method, which does not require assumptions about microstructure, morphology, or tracking the location of interfaces, can be used for a variety of diffusive and non-diffusive phase transitions, but requires input information about thermodynamic and kinetic parameters.[44, 45, 47, 212-215] Further input of thermodynamic/kinetic calculations of the physical properties of the constituents and the properties of the phase-phase interface (simulated by the PF method into the FEA method) can simulate more realistically the macroscopic response of the interface to external excitations.[48-51] With reliable models and well-designed numerical algorithms, simulation and prediction

with AI/DL can effectively and inexpensively understand the fine microstructure-behavior relationship of interfaces.[52, 54, 56, 104] Numerical simulation is increasingly applied in the development of MMCs because it can be used to improve the material components, processing techniques, etc., based on the simulation and prediction results. So far, numerical simulation studies have covered a wide range of spatial and temporal scales, including DFT,[36-40] MD,[5, 18, 41-43] PFM,[44-47, 215] FEA[48-51] and DL[52-58] etc. Numerical simulations have facilitated the understanding of the interfaces of MMCs and the development of advanced MMCs.

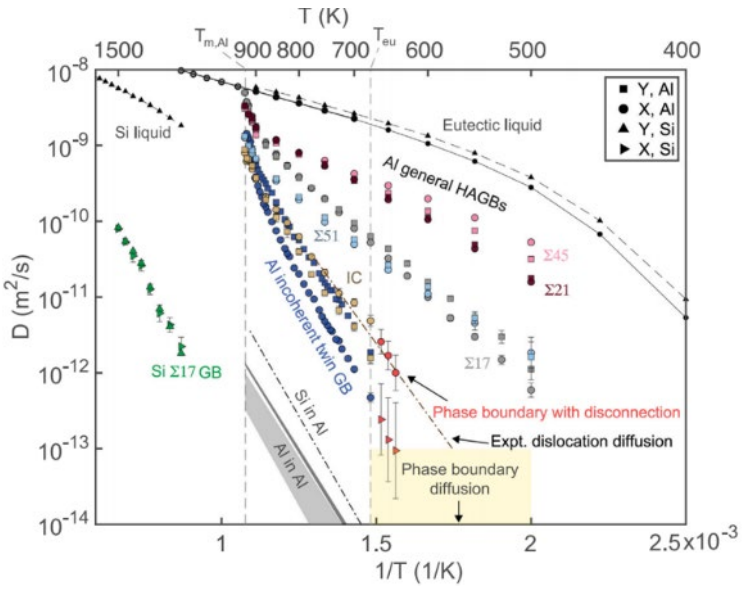


**Figure 29.** Arrhenius diagram of diffusion in Al, Si, and Al-Si systems. Reproduced with permission.[43] Copyright 2023, Elsevier.

5.1. Density functional theory

First-principles calculations consider the interaction between nuclei and electrons based on quantum mechanics and obtain the energies and states of the ground and excited states of the system by solving the Schrödinger equation, thus obtaining various physical and chemical properties of the material system. In interface studies, the fields of materials science and condensed matter physics refer to DFT-based

methods as first principles. The main contents of DFT in interface studies of MMCs include the initial/equilibrium configurations of the interfaces, the interfacial binding parameters (e.g., energies, distances, etc.), and the interfacial electronic structures (differential charge densities, projected electronic state densities), etc.[36, 82, 117, 211, 216-218] The research process usually starts by establishing the initial configuration of the interface to ensure that it can be fully relaxed, then use the DFT is used to screen out the equilibrium configurations of the interface and calculate binding energies, equilibrium distances, and electronic structures of the different interfacial configurations. DFT are able to analyze the interfacial binding energies, charge distributions, and electronic structures of the interface on the scales not accessible by the conventional experiments. These simulations can also screen out those with the highest interfacial binding energies and the highest electronic stability.[178] However, the existing first-principles calculations introduce assumptions and lack of independence of the model; they are not suitable for systems with poor crystal symmetry (non-compartmentalized interfaces) and large spatial scales; and the calculations cannot reach the accuracy required for engineering applications in multicomponent systems and at finite temperatures.

Taking the graphene/metal interface as an example, the interfacial binding parameters include interfacial binding energy $E_b$ , interfacial equilibrium spacing $d_{G-M}$ , minimum interatomic distance $d_{min}$ and maximum interatomic distance $d_{max}$ etc. The interfacial binding energy $E_b$ can be expressed as:

$$E_b = E_G + E_M - E_{G/M} \tag{5-1}$$

where the $E_G$ and $E_M$ denote the energies of isolated graphene and clean metal surfaces after structural optimization, respectively. $E_{G/M}$ denotes the energy of the equilibrium configuration of the graphene/metal interface, the larger $E_b$ is, the more stable interface structure is. Nanocarbon-reinforced

copper matrix composites are promising for thermal management and data transmission with interfaces characterized by defects, orientation, and binding energy.[41, 144, 219]

In the graphene/metal interface two main interfacial binding mechanisms prevail, the charge transfer mechanism and the orbital hybridization mechanism. Charge transfer due to repulsion between graphene π-electrons and the valence electrons of metal atoms results in the formation of a physical interface. Conversely, a chemical interface arises from orbital hybridization driven by covalent bonding between the same sets of electrons.[121, 122, 220] Differential charge density and electronic density of states (DOS) analyses are important tools for determining whether a chemical bond is formed between two atoms as the former allows for the visualization of the interfacial charge transfer, while the latter visualizes the coupling of the electronic density of states peaks. The differential charge density $\Delta_\rho$ can be expressed as:

$$\Delta_\rho = \rho_{G/M} - \rho_G - \rho_M \tag{5-2}$$

where $\rho_{G/M}$, $\rho_G$ and $\rho_M$ denote the charge densities of the graphene/metal interface equilibrium configuration, graphene, and metal slab models, respectively. An important sign of the formation of covalent bonds is the accumulation of large amounts of charge at the centers of two neighboring atoms, and vice versa. The coupling strength at the metal/non-metal interface is positively correlated with the interfacial electronic coupling.

**Figure 30**(a) illustrates the electronic structures of two Dia/Cu interfaces.[12] It shows that the (100)Dia/(100)Cu interface (1.549 Å) has closer equilibrium spacing than (111)Dia/(111)Cu (2.137 Å) with higher work of adhesion for (100)Dia/(100)Cu (4.204 J/m$^2$) over (111)Dia/(111)Cu (3.422 J/m$^2$). Generally, thermal boundary conductance and work of adhesion at metal/non-metal interfaces are positively correlated.[221] A better understanding of the $Ni_3Ti/Al_2O_3$ interfaces is considered to be essential

for the designing superior ceramic filler reinforced superalloys. As shown in Figure 30(b), Chen et al.[38] investigated the thermodynamic stability and mechanical strength of the $Ni_3Ti/\alpha\text{-}Al_2O_3$ interface by first-principles study. The valence charge density is mainly depleted at the interfacial region, indicating the mechanical failure may initiate at $Ni_3Ti/Al_2O_3$interface (Figure 30(b3)). However, the formation of strong interfacial Ti-O bonds causes the rapturing of Ti-Ni metallic bonds in the $Ni_3Ti$ phase very near the $Ni_3Ti/Al_2O_3$ interface (Figure 29(b4)).

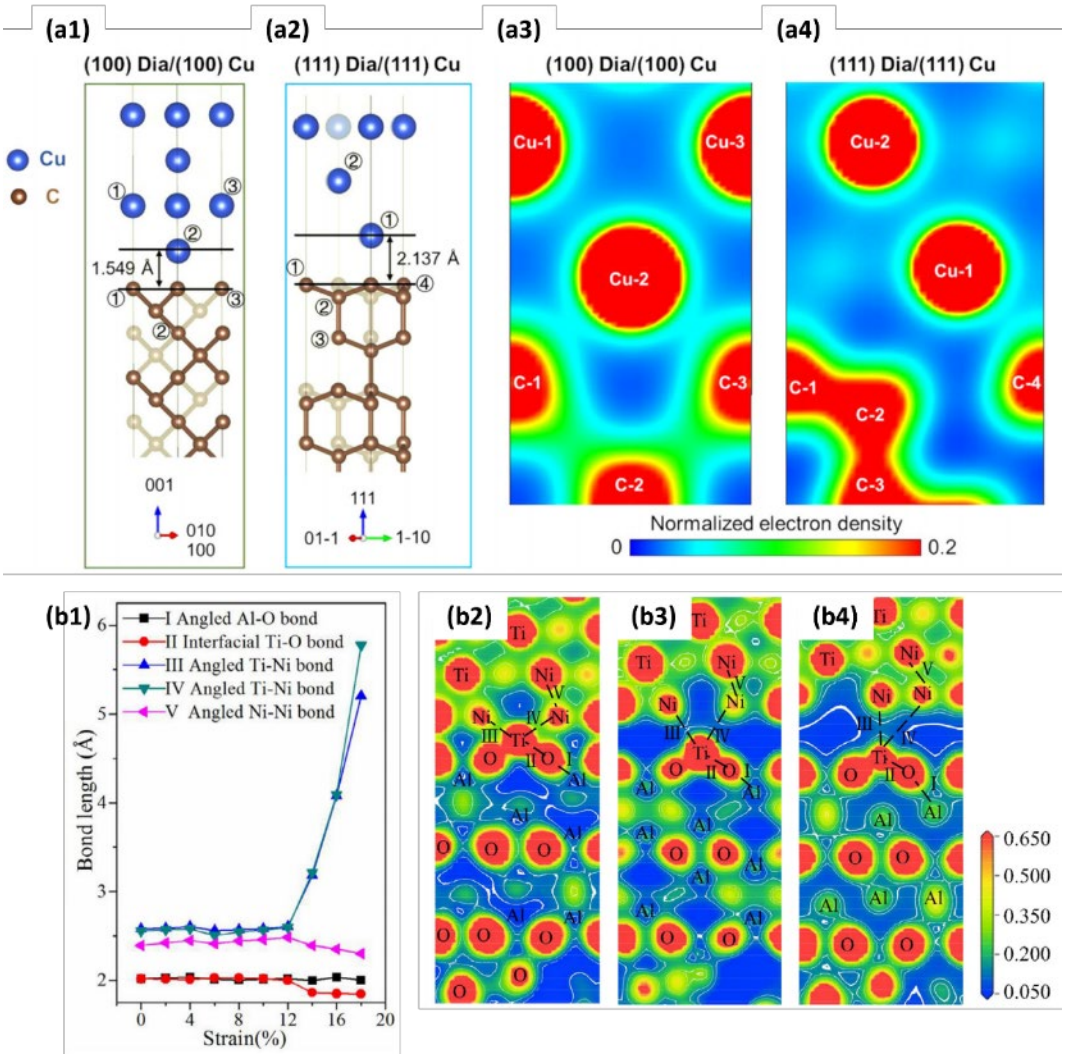


**Figure 30.** The electronic structure of the Dia/Cu interfaces. (a1) (100) Dia/(100) Cu interface, the interface equilibrium spacing is 1.549 Å (a2) (111) Dia/(111) Cu interface, the interface equilibrium spacing is 2.137 Å. Judging by the color depth, the electron density between (a3) C-1 and Cu-2 at the

(100) Dia/(100) Cu interface is higher than that between (a4) C-2 (or C-4) and Cu-1 at the (111) Dia/(111) Cu interface. Reproduced with permission.[12] Copyright 2021, Elsevier. (b1) Interfacial bond lengths of Ni&Ti-O-site11 interface as a function of applied uniaxial tensile strain. Valence charge density distributions through (110) slice intersecting Ni, Ti, O and Al atoms of the Ni&Ti-O-site11 interface at the different strain values: (b2) 0, (b3) 0.14, (b4) 0.16 respectively. Reproduced with permission.[38] Copyright 2021, Elsevier.

### 5.2. Molecular dynamics simulation

MD simulation characterizes the dynamics and interactions of microscopic entities within a system at an atomic or molecular level with the fidelity of the computational outcomes depending significantly on the selection of the potential function governing interatomic interactions. As a powerful theoretical computational tool, MD simulations have been widely used in the study of MMCs interfaces to help researchers understand the interfacial behaviors and mechanisms at the atomic scale. For ceramic/metal heterogeneous interfaces, MD simulations can obtain the diffusion coefficients at heterogeneous interfaces,[43] composite interfacial reactions,[5] interfacial stability,[21, 43, 222] interfacial defect evolution[18, 222] and interface deformation/failure[18, 42] etc. This is achieved by studying of systems in the range from tens to millions of atoms. However, the transferability of MD simulations is poor, different empirical potential functions and several coefficients to be determined for different composite systems and boundary conditions are required. Furthermore, materials are usually studied in a narrow range of scales, and the calculated deformation and strain rates of the materials are usually high under the consideration of the computational cost. Moreover, the parameters of the atomic simulation need to be based on experiments, and thus have certain limitations.

#### 5.2.1. Interface stability

High interfacial thermal stability and irradiation stability are important for MMCs to maintain good and stable thermo-mechanical and thermo-electrical properties under extreme conditions such as high temperature, high radiation and high stress levels. Interfacial stability is affected by interfacial properties such as composition, defects, orientation, adhesion energy and local strain, etc.[38, 143, 173, 223, 224] Therefore, it is important to understand the intrinsic link between microstructural features and interfacial stability for the design of MMCs.

As a typical metal-ceramic interface in composites, Chesser[43] investigated the atomic structure, thermal stability, and diffusion processes at the Al/Si interface using atomic computer simulations. In the Al-Si system, the diffusion mobility of Al and Si atoms at the stable Al-Si interface is much lower than their mobility at the Al grain boundaries (Figure 28); furthermore, the Si deviation leads to the disordering of the Al grain boundaries further accelerating the diffusion at grain boundaries. The nonequilibrium interface can be transformed into a more stable state by an interface-induced recrystallization mechanism.

It is widely recognized that irradiation with high-energy ions tends to introduce defects in metals. For example, helium (He) ion irradiation typically results in the formation of He bubbles in metals, while electron or heavy ion irradiation introduces point defects and clusters of defects.[222] The following are examples of defects introduced by electron or heavy ion irradiation. Under some extreme service conditions (e.g., nuclear radiation environments), the single-phase organization is susceptible to coarsening by short-range diffusion due to the low atomic packing density and high atomic mobility at GBs.[99] Utilizing phase boundaries in bionic layered composites made of incompatible elements can enhance thermal stability and radiation resistance. Gao et al.[21] studied interfacial radiation damage and He bubble formation by MD simulation, revealing that interfacial structure control is key to managing He

behavior. He atoms or clusters, owing to their two-dimensional diffusion, tend to accumulate more at sharp interfaces. In contrast, interfacial transitions and amorphous zones slow down the growth of larger He clusters due to the large free volume of three-dimensional interfaces and high He absorption capacity encouraging nucleation while limiting growth. Yang et al.[222] used MD simulations to calculate the stress fields of Gr/{100}Cu , Gr/{111}Cu and {111}Cu/{100}Cu interfaces prepared by different processes (ex-situ transferring, plasma enhanced chemical vapor deposition (PECVD), low pressure CVD) (**Figure 31**). At the T-Gr/{100}Cu interface, the lack of high-temperature deposition and C-Cu interaction results in zero average volume stress $\sigma$ at the interface. Conversely, for PECVD-Gr/{100}Cu and LPCVD-Gr/{111}Cu interfaces, stress extends into the Cu matrix with PECVD-Gr showing a significantly higher σ value (~303 MPa) than LPCVD-Gr (~102 MPa). Generally, interfaces with greater volumetric stresses tend to capture and hold more defects, making LPCVD-Gr/{111}Cu interfaces exhibit superior defect absorption and interfacial stability.[31, 225]

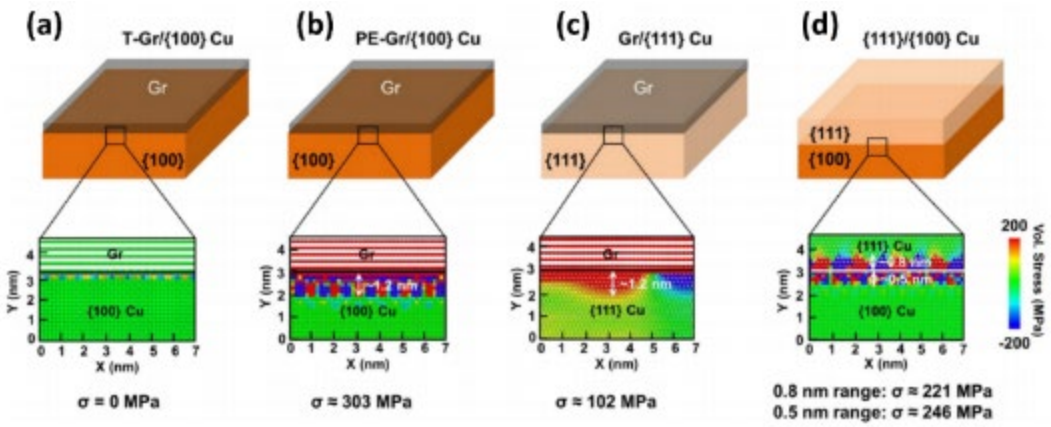


**Figure 31.** MD simulation results about the stress fields of the Gr/Cu interface and {111}/{100}Cu homogeneous interface. Reproduced with permission.[222] Copyright 2022, Elsevier.

5.2.2. Interfacial reaction kinetics

MD simulations are used to study the kinetic processes of interfacial reactions in MMCs, such as wetting and diffusion at the solid/liquid interface,[226] the formation of interfacial reaction layers and the stability of interfacial reaction products,[227] etc. They provide a theoretical basis (at atomic and molecular level) for optimizing the material preparation process and improving the material properties. MD simulations can reveal the pathways and microscopic mechanisms of interfacial reactions more intuitively, including activation energies, possible reaction pathways, and reaction rates,[227] which are essential for understanding and controlling the material synthesis process. Temperature and pressure are important factors that affect the kinetics of interfacial reactions. MD simulation allows researchers to model interfacial behavior at different temperatures and pressures, providing insight into how these external conditions affect interfacial reaction rates and products.

Nanoparticle thermite reactions encompass intricate interplays between phase changes and the diffusion of non-uniform atoms, particularly during initial phases at comparatively low temperatures where the system remains in a condensed state. Liu et al.[227] explored the redox reaction within a 2.2 nm Al/CuO multilayer nanofilm employing the ab initio MD simulation technique. A series of redox reactions with low activation potential barriers and high exotherm, occurring locally at the Al/$Al_2O_x$ interface and the $Al_2O_x$/$Cu_yO$ interface, are key to the occurrence of the whole thermite reaction, which promotes the decomposition of CuO and O to overcome the high energy barriers at the a-$Al_2O_x$ and Al/$Al_2O_x$ interfaces (~436.3 kJ-mol$^{-1}$, 208.8 kJ-mol$^{-1}$) to Al diffusion (**Figure 32**).

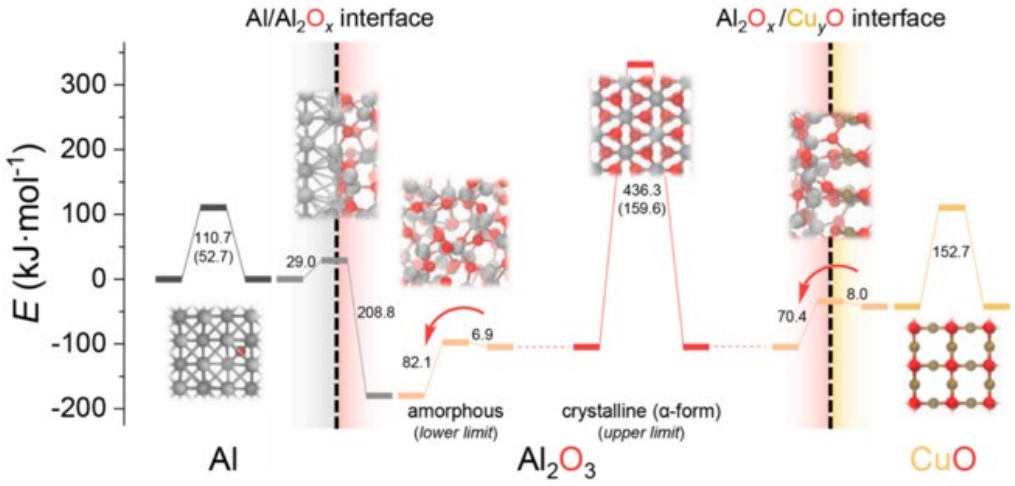


**Figure 32.** Barrier diagram of O migration through the Al/CuO nanolayers obtained by MD simulation. Reproduced with permission.[227] Copyright 2022, Elsevier.

5.3. Phase-field model

The term "phase field" (PF) was first created in the context of simulation studies of pure metal solidification.[213] With the development of materials science and modern computer technology, the PF model has been enriched and extended to many areas of materials research, e.g., solidification of binary/multiple alloys and their solid-state phase transitions,[214, 228] material defects,[229] MMCs[47] etc. The PF model assumes that the phase interface is a diffusion interface, and continuously introduces field variables describing the microstructure, such as composition, order parameter, phase distribution, magnetic domains, etc. PF simulates the multiphase organization evolution by numerically solving the evolution equations of the conservative field variables (e.g., compositions) and the non-conservative field variables (e.g., crystal orientations, long-range ordering, etc.). In contrast to methods such as DFT, MD and FEA, PF simulation bridges the gap between macroscopic and microscopic simulations and is a powerful computational method for describing and predicting the evolution of material microstructures.[230] One of the main advantages of the PF model, as a computational method for the study

of material dynamics, is that not only avoids complex interface tracking, but also facilitates the handling of various types of external factors (chemical, thermal, electrical, mechanical, magnetic, etc.). Therefore, PF can be used to analyze the influence of single or multiple factors on processes such as phase transformations, plastic deformations, chemical reactions, etc. The PF method has two principal limitations; (1) it requires input data on thermodynamic and kinetic parameters; (2) the PF approach is dependent on the description of continuous phenomena, and therefore does not allow access to detailed atomic mechanisms related to evolution.[212]

Common PF models include continuous phase-field, crystal phase-field, and microscopic phase-field (MPF) models.[231] In theoretical studies in the field of materials science, the MPF model is often applied to atomic scale analysis. Khachaturyan[232] created the microscopic lattice diffusion theory and constructed the MPF kinetic equation, which is actually a discrete lattice point form of the C-H equation. The MPF takes the discrete rigid lattice points as the basic unit of study on the spatial scale and takes the probability of occupancy of different elements (*S*) in all the single-crystalline lattice points ($\Phi_S(r,t)$ ) as the research object. In MPF, the dimensions of the study object are determined by the systematic calculation matrix ($n$) together with the cell parameters ($a$, $b$, $c$) of the alloy. The microscopic diffusion kinetic equation describing the atomic distribution is:

$$\frac{\mathrm{d}\Phi_S(r,t)}{\mathrm{d}t} = \sum_{r'} L_0(r,r') \frac{\delta\psi}{\delta(r',t)} \tag{5-3}$$

where $L_0(r,r')$ denotes the matrix of kinetic coefficients, and the subscript $S$ denotes the elemental species, $\psi$ denotes the free energy of the system under mean field theory, $r$ denotes the lattice coordinate position of the atom, and $t$ denotes the time. A specific introduction and detailed solution procedure of the MPF equations are described elsewhere.[45]

The study and simulation of MMCs interfaces are equally numerous for PF modeling. The in-situ reaction method for the preparation of MMCs has the advantages of no impurities between reinforcement and matrix, no contamination, and uniform particle distribution, and has become an important method for the preparation of MMCs. The current thermodynamic principles of in-situ reaction as well as the chemical reaction pathways of different composite systems have been fully revealed. However, since the reaction kinetics involves atomic long-range diffusion, interfacial reaction, liquid-solid phase transition, competitive nucleation, and grain growth, which is a complex problem with multi-scale and multi-physical field coupling, the reaction kinetics and mechanism still need to be further investigated. Thus, revealing the kinetic mechanism and law is of great theoretical and industrial value. The in-situ reaction process is characterized by short reaction time, random occurrence, high temperature, etc., and it is still difficult to observe the reaction process by in-situ experiments. Guo et al.[47] used the PF method to simulate the in-situ reaction process in metal melts, firstly, they established a PF model that describes the reaction nucleation at the interface of a two-beam metal melt, and then they used the model to simulate the reaction nucleation process at the phase boundary under different parameters. The results show that the nucleation rate increases with the increase of the radius of curvature and the noise intensity. The size distribution of the new phase particles is more homogeneous under the conditions of small radius of curvature and strong noise, and the nucleation rate initially increases and then decreases with the increase of the supercooling degree.

### 5.4. Finite element analysis

FEA is able to simulate complex structures and boundary conditions in real applications, including temperature variations, mechanical loads and contact problems; coupled problems of multi-physical fields,

such as thermal-force coupling and mechanical-electromagnetic coupling. Compared to atomic-level simulations such as DFT and MD, FEA can compute the behavior of large-scale models more efficiently. [48-51]

Recent studies[50, 141] have shown that the interfacial stability of Cu-Ag and Cu-Nb MNCs, which are typical representatives of the fcc/fcc and fcc/bcc MNCs systems, is affected not only by the intrinsic properties of the individual layers, but also by the neighboring phases and layers. With the aid of the crystal plasticity finite element analysis (FEA), Zhang[51] investigates the co-deformation and instability of heterophase interfaces in the classical MNCs system and predicts their local stress-strain fields under simple compressive deformation. The simulation results show that opposite stress states produce severe shear stresses at the heterogeneous interfaces, and the larger stress difference in the Cu-Nb system can provide higher tensile stresses and more severe shear strains than in the Cu-Ag system, thus accelerating the instability of the interface.

Despite the significant advantages of FEA in dealing with macroscale, complex boundary conditions and practical engineering applications, there are limitations in describing details at the microscale and atomic level.

### 5.5. Artificial intelligence and deep learning

The complex composition and topology of advanced MMCs leads to the existence of a huge design space that exceeds the computational limits of traditional design methods. Artificial intelligence (AI) offers solutions to these challenges, leveraging the intricate architecture of neural networks. Deep learning (DL), a technique within AI, can understand input data representations and deconstruct these into various layers, ranging from basic to complex components. The DL model learns from experience and

discovers correlations between input and output variables from large and often noisy datasets, and thus unseen data points to make predictions.[233] As a result, deep learning has shown promising applications in composite material performance prediction, optimal design, and intelligent manufacturing.[234] Among them, the key steps of DL-based advanced composite design are; collecting material datasets with good confidence, training efficiency from a large amount of experimental data, and numerical simulation results, and preprocessing the raw material database into appropriate numerical representations.[52] This requires a high level of expertise in materials science and artificial intelligence. In the field of composites, two methods, neural network and genetic algorithm, are most widely used, and some novel intelligent algorithms such as Firefly algorithm[235] and Particle swarm optimization[49] are also gradually applied to the optimization design of composite materials or neural network structures.[234] For example, Dieb et al.[58] applied a DL model to find the most stable structure of doped B atoms in graphene. With the help of reliable thermodynamic and kinetic data for DL training, combining PF simulation, image data construction and DL to optimize interfacial microstructures is a promising area for AI applications.[44]

In materials science, numerous DL-based applications focus on the discovery of molecular or crystal structures with desired properties.[236, 237] Application of DL on the design of complex structures of composite materials is reported elsewhere.[57] When subdivided into the field of interfaces in MMCs, the related research needs to be further strengthened, and research in similar fields can still provide references for the application of DL in the interfaces of MMCs. Junqueira[104] introduced a novel approach to address failure, defect, and damage evolution in laminated structural composites. This method employs DL regression techniques alongside Gaussian random field features to reconstruct heterogeneous defect fields across various interfaces and orientations in composite laminates. This is achieved by analyzing scattered

reflection field data obtained through ultrasonography. Xu[54] proposed a deep convolutional neural network-based model to explore the relationship between interface microstructure and behavior at the nanoscale (**Figure 33**). The author modeled and quantified the interfacial morphology of the reinforcement and the matrix through generated statistical correlation functions that represent interfacial units by using stochastic morphology reconstruction techniques, and used the interfacial elemental density fields and shear behaviors obtained from MD simulations to train the proposed DL model.

At present, the main method of applying AI to composite material performance prediction is to collect data through experiments or numerical simulations, use AI methods to assist mechanical modeling, or construct models directly from the data, and then run performance prediction after verifying the reliability of the AI model. The application of AI technology in composite materials currently is limited by dataset construction, processing and modelling. The accuracy of the prediction of high-precision artificial intelligence model (and uncertainty) is greatly affected by the dataset, which puts forward higher requirements for the construction of composite material database, and extracts the most critical feature parameters from the huge amount of data to reduce the amount of calculation.

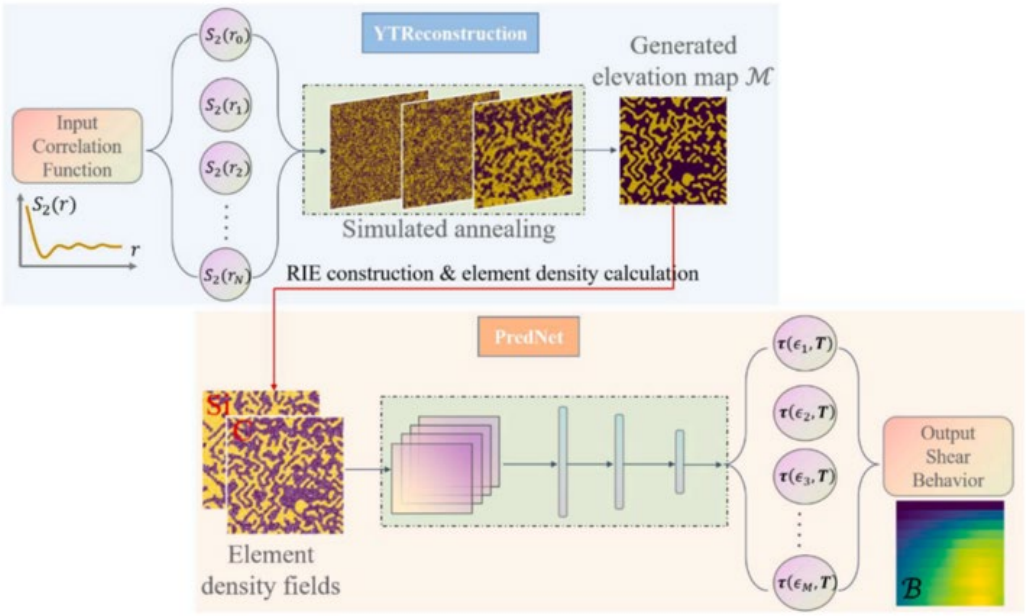


**Figure 33.** The overall architecture of the proposed model. Reproduced with permission.[54] Copyright 2022, Elsevier.

## 6. Summary

Numerous interfaces exist in MMCs, which is a key factor affecting both their mechanical properties and functionality. Being able to design MMCs has great advantages for the overall performance and functionality of composites. Proper design of interface structure can increase interfacial bond strength, improve physical and chemical compatibility, enhance stability, and promote phonon and electron transport. This paper reviews the recent advances and remaining problems in optimizing the interfacial structure and interfacial interaction mechanism of MMCs from four main aspects; (1) interfacial structure design, (2) interfacial defect control, (3) thermodynamics and kinetics of interfacial reactions, and (4) interfacial microstructure-property studies based on numerical simulation techniques.

MMCs failure is overwhelmingly attributed to interfacial damage as the interfacial deformation behavior dominates the plastic deformation of composites. An in-depth understanding of interfacial

microstructural features, such as interfacial atomic arrangement, distribution of interfacial dislocations, and evolution mechanisms, can help to deepen our understanding of the mechanisms of interface-mediated material deformation. By introducing bimodal grains, nanotwins, gradient grains, lamellar grains, and stacking defects into MMCs, we can promote the storage and transport of dislocations through the construction of heterogeneous interfaces to avoid stress concentration caused by dislocation stacking and to improve the work hardening that make the materials undergo stable and uniform plastic deformation. By designing novel interfacial structures and regulating the interfacial deformation behavior and failure mechanism in composites, the comprehensive properties of MMCs can be effectively improved.

Interfacial defects in MMCs are mainly point defects, including vacancy defects, doping defects, and topological defects, etc., and the types, locations (metal matrix or reinforcement side, close to or far away from interfaces), and numbers of defects significantly affect the interfacial bonding strength, interfacial phonon-electron transport and interfacial chemical reactivity. Interfacial defects can either diminish the bonding strength at the interface, resulting in inadequate load transfer and low mechanical properties of the composites. Contrary, they can enhance the interfacial bonding, such as vacancies on graphene that facilitate the creation of C-Al chemical bonds. Interfacial defects can affect thermal properties, e.g., increasing the density of interfacial vacancies or the density of dislocations near the interface introduces additional phonon scattering, which increases the interfacial thermal resistance. Interfacial defects can also affect the thermal diffusion behavior, the bias and precipitation of solute or impurity atoms, and the recovery of radiation-induced defects.

Complex multi-component metal reinforced phase interfacial systems may undergo a variety of

chemical reactions. Accurate thermodynamic/kinetic calculations of the Gibbs free energy, activity, self-diffusion-mutual diffusion coefficients, and interfacial energy and adhesion work of each component can greatly improve the precise control of the types of interfacial reaction products, nucleation rates, growth rates, and their distributions, and thus improve the physical and chemical compatibility of reinforcing body and substrate interfaces.

Interfacial microstructure modeling and prediction through numerical simulation for the design of advanced composites has received increasing attention and important advances have been made in this field. With the help of numerical simulation techniques, such as DFT, MD simulation, and PF modeling, we have been able to gain a more comprehensive and systematic understanding of the effects of interfacial microstructural features, such as interfacial atomic and electronic configurations, interfacial defects (vacancies, substitution atoms, etc.), on interfacial bonding parameters (interfacial bonding energies, equilibrium interfacial distances, etc.), interfacial physical and chemical compatibility, interfacial thermodynamic and kinetic parameters, interfacial-defect. While MD and PF methods focus on real-time dynamic tracking of material microevolution, first principles emphasize on static calculation of material physical parameters, and DL is used to predict performance prediction and optimal design through processing and modeling of existing datasets. With the help of several datasets consisting of thermodynamic and kinetic computational data and numerical simulation results with good credibility and training efficiency, which are used for the learning and training of AI models such as DL, the microstructure and performance prediction of MMCs interfaces can be guided more efficiently.

## 7. Outlook

The fundamental theory of new interfacial structures represented by heterogeneous interfaces and its

processing technology, interfacial defect engineering, thermodynamic and kinetic theory of interfacial reactions (computation and modeling), and simulation prediction of interfacial microstructures-properties based on numerical simulation techniques will be the focus in the development of MMCs in the future. However, the interfacial problem is still one of the main challenges to be solved in the composite system, and in particular to study the intrinsic relationship between the interface configuration of composites and their properties. We need to (1) reveal the coordinated deformation mechanism and toughening mechanism of the components in the multiphase and multiscale configurational composite system; (2) investigate how to accurately monitor the variety, number and distribution of interfacial defects through the defects engineering; when defects are not required, the repair means and mechanism related to defects need to be further investigated; (3) it is still demanding to accurately control the nature of the interfacial reaction interlayer (thickness, homogeneity, etc.), and the interfacial thermal and kinetic modeling of complex MMCs. The design of the composite microstructure primarily focuses on the geometric configuration and optimization of the matrix and reinforcing phases; however, the development of the microstructure design at the reinforcement/matrix interface requires further development. Although numerical simulations can deepen our understanding of the interface to a certain extent, their accuracy depends on accurate and reliable models and needs the support and verification of experimental data. Thus, it is crucial to find the key characteristic parameters from the large amount of data and to quantify the uncertainties of the parameters in the model and their impacts. The integrated computation and intelligent design of composites through multi-scale computational simulation with the guidance of "interface design-property prediction" will be the key area of MMCs interface research in the future.

**Conflict of interest**

The authors declare that they have no conflict of interest.

**Acknowledgments**

This work was supported by Key Laboratory of Infrared Imaging Materials and Detectors, Shanghai Institute of Technical Physics, Chinese Academy of Sciences (No. IIMDKFJJ-21-10).

**Data Availability statement**

The data used to support the findings of this study are available from the corresponding author upon request.

**References**

[1] R. Shu, X. Jiang, H. Sun, Z. Shao, T. Song, Z. Luo, *Composites Part A: Applied Science and Manufacturing* **2020**, *131*, 105816.

[2] Z. Zhang, G. Fan, Z. Tan, H. Zhao, Y. Xu, D. Xiong, Z. Li, *Composites Part B: Engineering* **2021**, *217*, 108916.

[3] F. Luo, X. Jiang, H. Sun, D. Mo, Y. Zhang, R. Shu, X. Li, *Journal of Alloys and Compounds* **2022**, *925*, 166710.

[4] P. Liu, B. Hou, A. Wang, J. Xie, Z. Wang, F. Ye, *Journal of Materials Science & Technology* **2023**, *159*, 21.

[5] Z. Liu, H. Yang, Y. Wang, Z. Xu, K. Zhang, R. Li, *Composites Part A: Applied Science and Manufacturing* **2023**, *175*, 107815.

[6] X. Zhang, D. Zhao, R. Shi, S. Zhu, L. Ma, C. He, N. Zhao, *Acta Materialia* **2022**, *240*, 118363.

[7] X. Ding, Z. Yang, *Electronic Commerce Research* **2022**, 1.

[8] Y. Jiang, Z. Tan, G. Fan, L. Wang, D. Xiong, Q. Guo, Y. Su, Z. Li, D. Zhang, *Carbon* **2020**, *158*, 449.

[9] B. Chen, J. Shen, X. Ye, H. Imai, J. Umeda, M. Takahashi, K. Kondoh, *Carbon* **2017**, *114*, 198.

[10] Z. Yu, Z. Tan, R. Xu, G. Ji, G. Fan, D. Xiong, Q. Guo, Z. Li, D. Zhang, *Carbon* **2019**, *146*, 155.

[11] K.M. Yang, Y.C. Ma, Z.Y. Zhang, J. Zhu, Z.B. Sun, J.S. Chen, H.H. Zhao, J. Song, Q. Li, N.Q. Chen, H.Y. Ma, J. Zhou, Y. Liu, T.X. Fan, *Acta Materialia* **2020**, *197*, 342.

[12] K. Yang, Z. Zhang, H. Zhao, B. Yang, B. Zhong, N. Chen, J. Song, C. Chen, D. Tang, J. Zhu, Y. Liu, T. Fan, *Acta Materialia* **2021**, *220*, 117283.

[13] W. Zhou, T. Yamaguchi, K. Kikuchi, N. Nomura, A. Kawasaki, *Acta Materialia* **2017**, *125*, 369.

[14] R. Shu, X. Jiang, Y.X. Zhang, R. Wuhrer, B. Liu, H. Sun, Z. Shao, Z. Luo, *Carbon* **2021**, *179*, 227.

[15] R.O. Ritchie, *Nature Materials* **2011**, *10(11)*, 817.

[16] X. Luo, K. Zhao, X. He, Y. Bai, V. De Andrade, M. Zaiser, L. An, J. Liu, *Acta Materialia* **2022**, *228*, 117730.

[17] W. Li, Y. Li, Y. Xiao, H. Zhang, X. Hu, F. Xu, *Composites Part A: Applied Science and Manufacturing* **2023**, *164*, 107282.

[18] T. Shimokawa, T. Niiyama, M. Okabe, J. Sawakoshi, *Acta Materialia* **2019**, *164*, 602.

[19] J. Wang, Q. Zhou, S. Shao, A. Misra, *Materials Research Letters* **2016**, *5(1)*, 1.

[20] Y. Chen, K.Y. Yu, Y. Liu, S. Shao, H. Wang, M.A. Kirk, J. Wang, X. Zhang, *Nature Communications* **2015**, *6*, 7036.

[21] R. Gao, M. Jin, F. Han, B. Wang, X. Wang, Q. Fang, Y. Dong, C. Sun, L. Shao, M. Li, J. Li, *Acta Materialia* **2020**, *197*, 212.

[22] Y.N. Zan, Y.T. Zhou, Z.Y. Liu, G.N. Ma, D. Wang, Q.Z. Wang, W.G. Wang, B.L. Xiao, Z.Y. Ma, *Materials & Design* **2019**, *166*, 107629.

[23] S. Wang, L. Huang, R. Zhang, B. Liu, X. Cui, L. Geng, H.-X. Peng, *Scripta Materialia* **2019**, *170*, 161.

[24] L. Lu, X. Chen, X. Huang, K. Lu, *Science* **2009**, *323(5914)*, 607.

[25] F. Yuan, D. Yan, J. Sun, L. Zhou, Y. Zhu, X. Wu, *Materials Research Letters* **2019**, *7(1)*, 12.

[26] F. Han, Y. Jiang, F. Cao, L. Cai, H. Zhang, S. Liang, *Materials Science and Engineering: A* **2023**, *885*, 145613.

[27] Y. Yang, Z. Jiang, X. Liu, J. Sun, W. Wang, *Journal of Materials Research and Technology* **2022**, *18*, 4846.

[28] Z. Cheng, H. Zhou, Q. Lu, H. Gao, L. Lu, *Science* **2018**, *362(6414)*, eaau 1925.

[29] F. Saba, H. Sun, G. Fan, Z. Tan, D. Xiong, Z. Li, Z. Li, *Composites Part A: Applied Science and Manufacturing* **2023**, *173*, 107700.

[30] K. Lu, L. Lu, S. Suresh, *Science* **2009**, *324(5925)*, 349.

[31] I.J. Beyerlein, M.J. Demkowicz, A. Misra, B.P. Uberuaga, *Progress in Materials Science* **2015**, *74*, 125.

[32] L. Jiang, K. Ma, H. Yang, M. Li, E.J. Lavernia, J.M. Schoenung, *Jom* **2014**, *66(6)*, 898.

[33] X.N. Mu, H.M. Zhang, P.W. Chen, X.W. Cheng, L. Liu, Y.X. Ge, N. Xiong, Y.C. Zheng, *Carbon* **2021**, *175*, 334.

[34] Z. Zhang, G. Fan, Z. Tan, H. Zhao, Y. Xu, D. Xiong, Z. Li, *Composites Part B: Engineering* **2021**, *224*, 109251.

[35] L. Liu, Y. Li, H. Zhang, X. Cheng, Q. Fan, X. Mu, *Composites Part B: Engineering* **2022**, *247*, 110237.

[36] Q. Hong, P. Bai, Z. Zhao, J. Wang, *Coatings* **2023**, *13(4)*, 680.

[37] M. Wang, Y. Zhang, H. Zheng, Z. Ru, X. Yang, *Materials Research Express* **2023**, *10(9)*, 096509.

[38] L. Chen, Y. Li, B. Xiao, Y. Gao, J. Wang, D. Yi, Z. Wang, S. Zhao, *Scripta Materialia* **2021**, *190*, 57.

[39] J. Huang, M. Li, J. Chen, Y. Cheng, Z. Lai, J. Hu, F. Zhou, N. Qu, Y. Liu, J. Zhu, *Surfaces and Interfaces* **2023**, *38*, 102825.

[40] L. Li, S. Reich, J. Robertson, *Physical Review B* **2005**, *72(18)*, 184109.

[41] S. Guo, X. Zhang, C. Shi, D. Zhao, C. He, N. Zhao, *Composites Part A: Applied Science and Manufacturing* **2023**, *169*, 107525.

[42] J. Zhang, Q. Xu, L. Gao, T. Ma, M. Qiu, Y. Hu, H. Wang, J. Luo, *Applied Surface Science* **2020**, *511*, 145620.

[43] I. Chesser, R.K. Koju, A. Vellore, Y. Mishin, *Acta Materialia* **2023**, *257*, 119172.

[44] J. Zhang, S.O. Poulsen, J.W. Gibbs, P.W. Voorhees, H.F. Poulsen, *Acta Materialia* **2017**, *129*, 229.

[45] L.Q. Chen, Y.H. Zhao, *Progress in Materials Science* **2022**, *124*, 100868.

[46] L. Zhao, T. Lee, S. Ryu, Y. Oshima, Q. Guo, D. Zhang, *Nano Letters* **2021**, *21(13)*, 5706.

[47] C. Guo, C. Kang, Y. Gao, Y. Zhang, Y. Deng, C. Ma, C. Xu, S. Liang, *Acta Physica Sinica* **2022**, *71(9)*.

[48] J. Zhang, Q. Ouyang, Q. Guo, Z. Li, G. Fan, Y. Su, L. Jiang, E.J. Lavernia, J.M. Schoenung, D. Zhang, *Composites Science and Technology* **2016**, *123*, 1.

[49] A.R. Vosoughi, A. Darabi, H.D. Forkhorji, *Composite Structures* **2017**, *159*, 361.

[50] N. Jia, F. Roters, P. Eisenlohr, D. Raabe, X. Zhao, *Acta Materialia* **2013**, *61(12)*, 4591.

[51] Y.B. Zhang, S.J. Song, F. Liu, *Journal of Materials Science & Technology* **2024**, *169*, 53.

[52] K. Guo, Z. Yang, C.H. Yu, M.J. Buehler, *Materials Horizons* **2021**, *8(4)*, 1153.

[53] S. Chen, N. Xu, *Composite Structures* **2023**, *318*, 117118.

[54] N. Xu, S. Chen, *Acta Materialia* **2023**, *244*, 118582.

[55] E. Maleki, O. Unal, S.M. Seyedi Sahebari, K. Reza Kashyzadeh, *Materials* **2023**, *16(13)*, 4693.

[56] K. Choudhary, B. DeCost, C. Chen, A. Jain, F. Tavazza, R. Cohn, C.W. Park, A. Choudhary, A. Agrawal, S.J.L. Billinge, E. Holm, S.P. Ong, C. Wolverton, *npj Computational Materials* **2022**, *8(1)*, 59.

[57] C. Chen, G.X. Gu, *MRS Communications* **2019**, *9(2)*, 556.

[58] T.M. Dieb, Z. Hou, K. Tsuda, *Journal of Chemical Physics* **2018**, *148(24)*.

[59] Z. Wu, X. Jiang, H. Sun, Z. Shao, R. Shu, Y. Zhang, Y. Fang, *Composites Part A: Applied Science and Manufacturing* **2022**, *163*, 107184.

[60] L. Yang, B. Zhou, L. Ma, G. Liu, S. Qian, Z. Xu, E. Liu, X. Zhang, C. He, N. Zhao, *Carbon* **2021**, *183*, 685.

[61] X. Jiang, W. Liu, Y. Li, Z. Shao, Z. Luo, D. Zhu, M. Zhu, *Composites Part B: Engineering* **2018**, *141*, 203.

[62] Y. Zhu, X. Wu, *Progress in Materials Science* **2023**, *131*, 101019.

[63] X. Luo, L. Zhang, X. He, J. Liu, K. Zhao, L. An, *Journal of Alloys and Compounds* **2021**, *855*.

[64] X. Zhang, T. Chen, S. Ma, H. Qin, J. Ma, *Composites Part B: Engineering* **2021**, *206*, 108541.

[65] Y. Ma, H. Chen, M.X. Zhang, A. Addad, Y. Kong, M.B. Lezaack, W.M. Gan, Z. Chen, G. Ji, *Acta Materialia* **2023**, *242*, 118470.

[66] M. Chen, G. Fan, Z. Tan, C. Yuan, Q. Guo, D. Xiong, M. Chen, Q. Zheng, Z. Li, D. Zhang, *Materials Characterization* **2019**, *153*, 261.

[67] X. Feaugas, *Acta Materialia* **1999**, *47(13)*, 3617.

[68] X. Wu, M. Yang, F. Yuan, G. Wu, Y. Wei, X. Huang, Y. Zhu, *Proceedings of the National Academy of Sciences of the United States of America* **2015**, *112(47)*, 14501.

[69] J. Wang, R.G. Hoagland, J.P. Hirth, A. Misra, *Acta Materialia* **2008**, *56(19)*, 5685.

[70] L. Liu, Y. Li, H. Zhang, X. Cheng, Q. Fan, X. Mu, S. Guo, *Ceramics International* **2021**, *47(3)*, 4338.

[71] J. Wang, A. Misra, R.G. Hoagland, J.P. Hirth, *Acta Materialia* **2012**, *60(4)*, 1503.

[72] Z. Li, L. Zhao, Q. Guo, Z. Li, G. Fan, C. Guo, D. Zhang, *Scripta Materialia* **2017**, *131*, 67.

[73] J. Wang, R.G. Hoagland, J.P. Hirth, A. Misra, *Acta Mater.* **2008**, *56(19)*, 5685.

[74] Y. Jiang, R. Xu, Z. Tan, G. Ji, G. Fan, Z. Li, D. Xiong, Q. Guo, Z. Li, D. Zhang, *Carbon* **2019**, *146*, 17.

[75] H. Gao, Y. Huang, W.D. Nix, J.W. Hutchinson, *Journal of the Mechanics and Physics of Solids* **1999**, *47(6)*, 1239.

[76] I.A. Ovid'ko, R.Z. Valiev, Y.T. Zhu, *Progress in Materials Science* **2018**, *94*, 462.

[77] X. Tong, J.M. Gibson, *Applied Physics Letters* **1994**, *65(2)*, 168.

[78] H.Y. Yang, Z. Wang, L.Y. Chen, S.L. Shu, F. Qiu, L.C. Zhang, *Composites Part B: Engineering* **2021**, *209*, 108605.

[79] M. Cao, D. Xiong, L. Yang, S. Li, Y. Xie, Q. Guo, Z. Li, H. Adams, J. Gu, T. Fan, X. Zhang, D. Zhang, *Advanced Functional Materials* **2019**, *29(17)*, 1806792.

[80] L.M. Liu, S.Q. Wang, H.Q. Ye, *Surface Science* **2004**, *550(1-3)*, 46.

[81] L.M. Liu, S.Q. Wang, H.Q. Ye, *Journal of Physics-Condensed Matter* **2004**, *16(32)*, 5781.

[82] Y. Han, Y. Dai, D. Shu, J. Wang, B. Sun, *Applied Physics Letters* **2006**, *89(14)*.

[83] C. Deng, B. Xu, P. Wu, Q. Li, *Applied Surface Science* **2017**, *425*, 639.

[84] S. Jiang, H. Wang, Y. Wu, X. Liu, H. Chen, M. Yao, B. Gault, D. Ponge, D. Raabe, A. Hirata, M. Chen, Y. Wang, Z. Lu, *Nature* **2017**, *544(7651)*, 460.

[85] L.M. Brown, G.R. Woolhouse, *The Philosophical Magazine: A Journal of Theoretical Experimental and Applied Physics* **1970**, *21(170)*, 329.

[86] F. Long, X. Guo, K. Song, J. Liu, X. Wang, Y. Yang, S. Li, *Composites Part B: Engineering* **2022**, *229*, 109455.

[87] J. Wang, A. Misra, *Current Opinion in Solid State & Materials Science* **2011**, *15(1)*, 20.

[88] S. Peng, Y. Wei, H. Gao, *Proceedings of the National Academy of Sciences of the United States of America* **2020**, *117(10)*, 5204.

[89] Y. Zhu, X. Wu, *Materials Research Letters* **2019**, *7(10)*, 393.

[90] L. Lu, Y.F. Shen, X.H. Chen, L.H. Qian, K. Lu, *Science* **2004**, *304(5669)*, 422.

[91] Y. Liu, J. Song, G. Liu, J. Chen, C. Wang, H. Wang, J. Wang, X. Zhang, *Nano Letters* **2021**, *21(15)*, 6480.

[92] S. Zheng, Z. Yan, X. Kong, R. Zhang, *Acta Metallurgica Sinica* **2022**, *58(6)*, 709.

[93] A. Misra, J.P. Hirth, R.G. Hoagland, *Acta Materialia* **2005**, *53(18)*, 4817.

[94] J. Languillaume, G. Kapelski, B. Baudelet, *Acta Materialia* **1997**, *45(3)*, 1201.

[95] T. Ohashi, L. Roslan, K. Takahashi, T. Shimokawa, M. Tanaka, K. Higashida, *Materials Science and Engineering: A* **2013**, *588*, 214.

[96] B. Ji, H. Gao, *Annual Review of Materials Research* **2010**, *40*, 77.

[97] S. Zheng, I.J. Beyerlein, J.S. Carpenter, K. Kang, J. Wang, W. Han, N.A. Mara, *Nature*

*Communications* **2013**, *4*, 1696.

[98] Y. Wang, J. Li, A.V. Hamza, T.W. Barbee, Jr., *Proceedings of the National Academy of Sciences of the United States of America* **2007**, *104(27)*, 11155.

[99] W.B. Liu, C. Zhang, Y.Z. Ji, Z.G. Yang, H. Zang, T.L. Shen, L.Q. Chen, *Applied Physics Letters* **2014**, *105(12)*.

[100] X.F. Kong, N. Gao, I.J. Beyerlein, B.N. Yao, S.J. Zheng, X.L. Ma, D. Legut, T.C. Germann, H.J. Zhang, R.F. Zhang, *Acta Materialia* **2020**, *188*, 623.

[101] W. Yang, M. Gong, J. Yao, J. Wang, S. Zheng, X. Ma, *Scripta Materialia* **2021**, *200*, 113917.

[102] Z.Y. Hu, Z.H. Zhang, H. Wang, S.L. Li, S.P. Yin, S. Qi, X.W. Cheng, *Materials Science and Engineering: A* **2018**, *721*, 61.

[103] Y. Wang, Z. Zhang, F. Xiao, *Materials Science and Engineering: A* **2017**, *705*, 160.

[104] B.F. Junqueira, R. Leiderman, D.A. Castello, *Composite Structures* **2023**, *314*, 116985.

[105] Y. Liu, X.H. Tang, S.F. Zhou, B.S. Guo, Z.G. Zhang, W. Li, *Materials Science and Engineering: A* **2022**, *834*, 142615.

[106] G. Li, M. Liu, S. Lyu, M. Nakatani, R. Zheng, C. Ma, Q. Li, K. Ameyama, *Scripta Materialia* **2021**, *191*, 196.

[107] G.N. Lewis, M. Randall, K.S. Pitzer, L. Brewer, *Thermodynamics*, Courier Dover Publications, **2020**.

[108] Y. Xiong, W. Hu, Y. Shu, X. Luo, Z. Zhang, J. He, C. Yin, K. Zheng, *Journal of Materials Science & Technology* **2022**, *123*, 1.

[109] V. Soleimanian, M. Mojtahedi, M. Goodarzi, M.R. Aboutalebi, *Journal of Alloys and Compounds*

**2014**, *590*, 565.

[110] M. Mhadhbi, M. Khitouni, L. Escoda, J.J. Sunol, M. Dammak, *Journal of Nanomaterials* **2010**, *2010*, 1.

[111] K. Edalati, H. Shao, H. Emami, H. Iwaoka, E. Akiba, Z. Horita, *International Journal of Hydrogen Energy* **2016**, *41(21)*, 8917.

[112] D.J. Lee, E.Y. Yoon, D.H. Ahn, B.H. Park, H.W. Park, L.J. Park, Y. Estrin, H.S. Kim, *Acta Materialia* **2014**, *76*, 281.

[113] K. Chu, J. Wang, Y.P. Liu, Z.R. Geng, *Carbon* **2018**, *140*, 112.

[114] B. Guo, X. Zhang, X. Cen, B. Chen, X. Wang, M. Song, S. Ni, J. Yi, T. Shen, Y. Du, *Carbon* **2018**, *139*, 459.

[115] W. Zhou, S. Bang, H. Kurita, T. Miyazaki, Y. Fan, A. Kawasaki, *Carbon* **2016**, *96*, 919.

[116] Y. Dong, X. Lin, D. Wang, R. Yuan, S. Zhang, X. Chen, L.G. Bulusheva, A.V. Okotrub, H. Song, *Energy Storage Materials* **2020**, *30*, 287.

[117] Y. Mei, B. Ju, W. Yang, Z. Xiu, B. Zhao, G. Wu, *Applied Composite Materials* **2021**, *28(6)*, 1845.

[118] K. Chu, F. Wang, Y.B. Li, X.H. Wang, D.J. Huang, Z.R. Geng, *Composites Part A: Applied Science and Manufacturing* **2018**, *109*, 267.

[119] H. Gleiter, *Acta Metallurgica* **1979**, *27(2)*, 187.

[120] F. Wang, J. Zhang, K. Sun, L. Quan, J. Wang, N. Zhao, C. Shi, S. Zheng, *Composites Part B: Engineering* **2022**, *246*, 110267.

[121] S.K. Tiwari, S.K. Pandey, R. Pandey, N. Wang, M. Bystrzejewski, Y.K. Mishra, Y. Zhu, *Small* **2023**, *19(44)*, 2303340.

[122] B.P. Klein, A. Ihle, S.R. Kachel, L. Ruppenthal, S.J. Hall, L. Sattler, S.M. Weber, J. Herritsch, A. Jaegermann, D. Ebeling, R.J. Maurer, G. Hilt, R. Tonner-Zech, A. Schirmeisen, J.M. Gottfried, *ACS Nano* **2022**, *16(8)*, 11979.

[123] Q. Wu, J. Xie, A. Wang, C. Wang, A. Mao, *Computational Materials Science* **2019**, *158*, 110.

[124] Q. Yang, J.X. Cao, Y. Ma, Y.C. Zhou, L.M. Jiang, X.L. Zhong, *Journal of Applied Physics* **2013**, *113(18)*.

[125] B.Y. Ju, W.S. Yang, Q. Zhang, M. Hussain, Z.Y. Xiu, J. Qiao, G.H. Wu, *International Journal of Minerals, Metallurgy and Materials* **2020**, *27(9)*, 1179.

[126] M.S.A. Bhuyan, M.N. Uddin, M.M. Islam, F.A. Bipasha, S.S. Hossain, *International Nano Letters* **2016**, *6(2)*, 65.

[127] M.C. Wang, C. Yan, L. Ma, N. Hu, M.W. Chen, *Computational Materials Science* **2012**, *54*, 236.

[128] A.M. Valencia, M.J. Caldas, *Physical Review B* **2017**, *96(12)*, 125431.

[129] I.A. Popov, K.V. Bozhenko, A.I. Boldyrev, *Nano Research* **2012**, *5(2)*, 117.

[130] F. Banhart, J. Kotakoski, A.V. Krasheninnikov, *ACS Nano* **2011**, *5(1)*, 26.

[131] X. Zhang, S. Wang, *Nanomaterials* **2021**, *11(3)*, 738.

[132] R. Xie, S. Lu, W. Li, Y. Tian, L. Vitos, *Acta Materialia* **2020**, *191*, 43.

[133] Y. Sun, X. Liu, W. Wang, Y. Yang, W. Zhang, *Journal of Materials Science & Technology* **2023**, *144*, 150.

[134] T. Gong, P. Yao, X. Xiong, H. Zhou, Z. Zhang, Y. Xiao, L. Zhao, M. Deng, *Journal of Alloys and Compounds* **2019**, *786*, 975.

[135] Y. Xie, X. Meng, D. Mao, Z. Qin, L. Wan, Y. Huang, *ACS Applied Materials & Interfaces* **2021**,

*13(27)*, 32161.

[136] J. Carrasco, J.R.B. Gomes, F. Illas, *Physical Review B* **2004**, *69(6)*, 064116.

[137] B. Guo, B. Chen, X. Zhang, X. Cen, X. Wang, M. Song, S. Ni, J. Yi, T. Shen, Y. Du, *Carbon* **2018**, *135*, 224.

[138] G. Kudur Jayaprakash, N. Casillas, P.D. Astudillo-Sanchez, R. Flores-Moreno, *J. Phys. Chem. A* **2016**, *120(45)*, 9101.

[139] X. Du, W. Du, Z. Wang, K. Liu, S. Li, *Applied Surface Science* **2019**, *484*, 414.

[140] N. Li, J. Wang, J.Y. Huang, A. Misra, X. Zhang, *Scripta Materialia* **2010**, *63(4)*, 363.

[141] J. Wang, R.G. Hoagland, A. Misra, *Applied Physics Letters* **2009**, *94(13)*.

[142] J.W. Wang, J.L. Fan, H.R. Gong, *Journal of Alloys and Compounds* **2016**, *661*, 553.

[143] Q. Wang, Z. Zhao, P. Bai, W. Du, H. Liao, Y. Li, M. Liang, P. Huo, L. Zhang, D. Tie, *Advanced Composites and Hybrid Materials* **2021**, *4(1)*, 195.

[144] Z. Li, L. Liu, R. Bao, J. Yi, C. Li, X. Chen, C. Liu, *Composites Part A: Applied Science and Manufacturing* **2024**, *177*, 107885.

[145] E. Dervishi, Z. Ji, H. Htoon, M. Sykora, S.K. Doorn, *Nanoscale* **2019**, *11(35)*, 16571.

[146] W. Ahmad, Z. Ullah, N.I. Sonil, K. Khan, *Journal of Materials Science-Materials in Electronics* **2021**, *32(15)*, 19991.

[147] Y. Xie, X. Meng, Y. Chang, D. Mao, Z. Qin, L. Wan, Y. Huang, *Adv Sci (Weinh)* **2022**, *9(23)*, e2104464.

[148] B. Zhang, P. Han, J. Mei, *Applied Surface Science* **2022**, *593*, 153356.

[149] Y. Ito, Y. Shen, D. Hojo, Y. Itagaki, T. Fujita, L. Chen, T. Aida, Z. Tang, T. Adschiri, M. Chen,

*Advanced Materials* **2016**, *28(48)*, 10644.

[150] A. Shekhawat, R.O. Ritchie, *Nature Communications* **2016**, *7*, 10546.

[151] O.V. Yazyev, S.G. Louie, *Nature Materials* **2010**, *9(10)*, 806.

[152] N.M. Santhosh, G. Filipic, E. Kovacevic, A. Jagodar, J. Berndt, T. Strunskus, H. Kondos, M. Hori, E. Tatarova, U. Cvelbar, *Nano-Micro Letters* **2020**, *12(1)*, 1.

[153] S. Doniach, M. Sunjic, *Journal of Physics C: Solid State Physics* **1970**, *3(2)*, 285.

[154] W.W. Jian, G.M. Cheng, W.Z. Xu, H. Yuan, M.H. Tsai, Q.D. Wang, C.C. Koch, Y.T. Zhu, S.N. Mathaudhu, *Materials Research Letters* **2013**, *1(2)*, 61.

[155] X.L. Wu, Y.T. Zhu, Y.G. Wei, Q. Wei, *Physical Review Letters* **2009**, *103(20)*, 205504.

[156] B. Guo, M. Song, X. Zhang, Y. Liu, X. Cen, B. Chen, W. Li, *Composites Part B: Engineering* **2021**, *211*, 108646.

[157] D. Zhou, X. Zhang, A. Tehranchi, J. Hou, W. Lu, T. Hickel, D. Ponge, D. Raabe, D. Zhang, *Composites Part B: Engineering* **2022**, *245*, 110211.

[158] M. Shih, J. Miao, M. Mills, M. Ghazisaeidi, *Nature Communications* **2021**, *12(1)*, 3590.

[159] Anxianghai, S. Wu, Z. Zhang, *Acta Metallurgica Sinica* **2014**, *50(2)*, 191.

[160] Z. Zhang, K. Li, T. Cai, P. Li, Z. Zhang, R. Liu, J. Yang, P. Zhang, *Acta Metallurgica Sinica* **2023**, *59(4)*, 467.

[161] Y.T. Zhu, X.Z. Liao, X.L. Wu, *Progress in Materials Science* **2012**, *57(1)*, 1.

[162] J. Li, H. Qu, J. Bai, *Acta Materialia* **2022**, *226*.

[163] Y. Wu, C. Zhou, R. Wu, L. Sun, C. Lu, Y. Xiao, Z. Su, M. Gong, K. Ming, K. liu, C. Gu, W. Yang, J. Wang, G. Wu, *Composites Part B: Engineering* **2023**, *250*, 110458.

[164] W. Yang, R. Dong, L. Jiang, G. Wu, M. Hussain, *Vacuum* **2015**, *122*, 1.

[165] H.Q. Duan, H.M. Zhang, X.N. Mu, Q.B. Fan, X.W. Cheng, N. Xiong, K. Feng, *Materials Characterization* **2023**, *201*, 112965.

[166] X. Rong, D. Zhao, C. He, C. Shi, E. Liu, N. Zhao, *Acta Materialia* **2021**, *204*, 116524.

[167] B. Chen, K. Kondoh, J. Umeda, S. Li, L. Jia, J. Li, *Journal of Alloys and Compounds* **2019**, *789*, 25.

[168] X. Rong, D. Zhao, X. Chen, X. Zhang, D. Wan, C. Shi, C. He, N. Zhao, *Acta Materialia* **2023**, *256*, 119110.

[169] J.M. Howe, *International Materials Reviews* **1993**, *38(5)*, 233.

[170] T. Fan, G. Yang, D. Zhang, *Materials Science and Engineering: A* **2005**, *394(1-2)*, 327.

[171] D. Kocaefe, A. Sarkar, X.G. Chen, *International Journal of Materials Research* **2012**, *103(6)*, 729.

[172] W. Guo, Q. Hu, P. Xiao, Y. Deng, *Applied Surface Science* **2022**, *584*, 152619.

[173] F. Wang, H. Jiang, Z. Yao, J. Dong, *Journal of Alloys and Compounds* **2022**, *917*, 165218.

[174] F. Qin, T. Fan, D. Zhang, *Metallurgical and Materials Transactions a-Physical Metallurgy and Materials Science* **2009**, *40A(2)*, 462.

[175] D. Shin, A. Shyam, S. Lee, Y. Yamamoto, J.A. Haynes, *Acta Materialia* **2017**, *141*, 327.

[176] S. Kovacevic, R. Pan, D.P. Sekulic, S.D. Mesarovic, *Acta Materialia* **2020**, *186*, 405.

[177] A. Chen, Q. Su, H. Han, E. Enriquez, Q. Jia, *Adv Mater* **2019**, *31(4)*, 1803241.

[178] X. Tang, J. Zhang, T. Ma, *China Surface Engineering* **2022**, *35(3)*, 16.

[179] X. Zhang, T. Hu, J.F. Rufner, T.B. LaGrange, G.H. Campbell, E.J. Lavernia, J.M. Schoenung, K. van Benthem, *Acta Materialia* **2015**, *95*, 254.

[180] X. Kai, L. Wu, Y. Peng, Z. Tan, G. Li, G. Chen, X. Xu, Z. Li, Y. Zhao, *Composites Part B:*

*Engineering* **2021**, *224*, 109156.

[181] S. Ranjan, P.K. Jha, *Journal of Manufacturing Processes* **2023**, *95*, 14.

[182] Z.L. Chao, L.T. Jiang, G.Q. Chen, J. Qiao, Q. Z, Z.H. Yu, Y.F. Cao, G.H. Wu, *Composites Part B: Engineering* **2019**, *161*, 627.

[183] A.B. Li, X.P. Cui, G.S. Wang, W. Qu, F. Li, X.X. Zhang, W.C. Gan, L. Geng, S.H. Meng, *Materials Letters* **2016**, *185*, 351.

[184] Z. Ni, Y. Zhang, P. Li, Y. Cheng, *Hot Working Technology* **2015**, *44(10)*, 34.

[185] X. Wang, L. Wang, L. Luo, H. Yan, X. Li, R. Chen, Y. Su, J. Guo, H. Fu, *Materials & Design* **2017**, *121*, 335.

[186] S. Ploetz, R. Nowak, A. Lohmueller, N. Sobczak, R.F. Singer, *Advanced Engineering Materials* **2016**, *18(11)*, 1884.

[187] P. Nautiyal, A. Gupta, S. Seal, B. Boesl, A. Agarwal, *Acta Materialia* **2017**, *126*, 124.

[188] W. Qu, T. Fan, *Materials Reports* **2019**, *33(11A)*, 3606.

[189] K.C. Mills, Y.C. Su, *International Materials Reviews* **2006**, *51(6)*, 329.

[190] W. Fu, Y. Xue, J. Dai, X. Song, S. Hu, H. Bian, D. Lin, *Surfaces and Interfaces* **2023**, *38*, 102840.

[191] G. Zhao, Z. Shi, N. Ta, G. Ji, R. Zhang, *Materials & Design* **2015**, *66*, 492.

[192] X. Rong, X. Zhang, D. Zhao, C. He, C. Shi, E. Liu, N. Zhao, *Scripta Materialia* **2021**, *198*, 113825.

[193] C. Cai, S. He, L. Li, Q. Teng, B. Song, C. Yan, Q. Wei, Y. Shi, *Composites Part B-Engineering* **2019**, *164*, 546.

[194] X. Rong, X. Chen, D. Zhao, X. Zhang, C. He, C. Shi, N. Zhao, *Composites Part A: Applied Science and Manufacturing* **2023**, *173*, 107630.

[195] T. Venugopal, K.P. Rao, B.S. Murty, *Materials Science and Engineering: A* **2005**, *393(1-2)*, 382.

[196] K.X. Song, J.D. Xing, Q.M. Dong, P. Liu, B.H. Tian, X.J. Cao, *Materials Science and Engineering: A* **2004**, *380(1-2)*, 117.

[197] X. Chen, J. Tao, Y. Liu, R. Bao, F. Li, C. Li, J. Yi, *Carbon* **2019**, *146*, 736.

[198] X. Chen, F. Qian, X. Bai, D. Zhao, X. Zhang, J. Li, C. He, C. Shi, J. Tao, N. Zhao, *Acta Materialia* **2022**, *228*, 117758.

[199] Y. Jiang, Z. Tan, G. Fan, Z. Zhang, D. Xiong, Q. Guo, Z. Li, D. Zhang, *Carbon* **2020**, *161*, 17.

[200] T.F. Chung, Y.L. Yang, M. Shiojiri, C.N. Hsiao, W.C. Li, C.S. Tsao, Z. Shi, J. Lin, J.R. Yang, *Acta Materialia* **2019**, *174*, 351.

[201] Z. Che, Y. Zhang, J. Li, H. Zhang, X. Wang, C. Sun, J. Wang, M.J. Kim, *Journal of Alloys and Compounds* **2016**, *657*, 81.

[202] A. Okura, K. Motoki, *Composites Science and Technology* **1985**, *24(4)*, 243.

[203] X.N. Mu, H.M. Zhang, H.N. Cai, Q.B. Fan, Z.H. Zhang, Y. Wu, Z.J. Fu, D.H. Yu, *Materials Science and Engineering: A* **2017**, *687*, 164.

[204] Z.L. Chao, L.T. Jiang, G.Q. Chen, J. Qiao, Q. Z, Z.H. Yu, Y.F. Cao, G.H. Wu, *Composites Part B-Engineering* **2019**, *161*, 627.

[205] A. Miedema, P. De Chatel, F. De Boer, *Physica B+C* **1980**, *100(1)*, 1.

[206] G.M. Wilson, *Journal of the American Chemical Society* **1964**, *86(2)*, 127.

[207] A. Fick, *Annalen der Physik* **1855**, *170(1)*, 59.

[208] X.J. Han, M. Chen, Y.J. Lue, *International Journal of Thermophysics* **2008**, *29(4)*, 1408.

[209] E. Fodor, C. Nardini, M.E. Cates, J. Tailleur, P. Visco, F. van Wijland, *Physical Review Letters* **2016**,

*117(3)*, 038103.

[210] G. Schwitzgebel, G. Langen, *Zeitschrift für Naturforschung A* **1981**, *36(11)*, 1225.

[211] H. Chun, D. Choi, J. Kang, J.S. Park, B. Han, *Applied Surface Science* **2020**, *509*, 144861.

[212] L.Q. Chen, *Journal of the American Ceramic Society* **2008**, *91(6)*, 1835.

[213] L.Q. Chen, *Annual Review of Materials Research* **2002**, *32*, 113.

[214] E. Alster, K.R. Elder, J.J. Hoyt, P.W. Voorhees, *Physical Review E* **2017**, *95(2)*, 022105.

[215] T.Q. Bui, X. Hu, *Engineering Fracture Mechanics* **2021**, *248*, 107705.

[216] X. Zhang, Y. Ji, L.-Q. Chen, Y. Wang, *Acta Materialia* **2023**, *252*, 118786.

[217] H.Z. Fang, S.L. Shang, Y. Wang, Z.K. Liu, D. Alfonso, D.E. Alman, Y.K. Shin, C.Y. Zou, A.C.T. van Duin, Y.K. Lei, G.F. Wang, *Journal of Applied Physics* **2014**, *115(4)*.

[218] T. Sun, W. Xu, X. Wu, Y. Jiang, X. Qu, *Physics Letters A* **2023**, *471*, 128786.

[219] S. Ali, F. Ahmad, P.S.M.M. Yusoff, N. Muhamad, E. Onate, M.R. Raza, K. Malik, *Composites Part A: Applied Science and Manufacturing* **2021**, *144*, 106357.

[220] C. Gong, G. Lee, B. Shan, E.M. Vogel, R.M. Wallace, K. Cho, *Journal of Applied Physics* **2010**, *108(12)*.

[221] C. Monachon, G. Schusteritsch, E. Kaxiras, L. Weber, *Journal of Applied Physics* **2014**, *115(12)*.

[222] K.M. Yang, Q. Li, Q. Zhang, G.S. Liu, J.J. Wang, Y.F. Yang, C.X. Guo, J.M. Ni, J. Song, J. Zhang, Y. Liu, T.X. Fan, *Acta Materialia* **2022**, *226*, 117638.

[223] W.Z. Han, M.J. Demkowicz, E.G. Fu, Y.Q. Wang, A. Misra, *Acta Materialia* **2012**, *60(18)*, 6341.

[224] I.J. Beyerlein, J.R. Mayeur, S. Zheng, N.A. Mara, J. Wang, A. Misra, *Proceedings of the National Academy of Sciences of the United States of America* **2014**, *111(12)*, 4386.

[225] K.M. Yang, P.Z. Tang, Q. Zhang, H.Y. Ma, E.Q. Liu, M. Li, X. Zhang, J. Li, Y. Liu, T.X. Fan, R. Namakian, *Scripta Materialia* **2021**, *203*, 114001.

[226] Q. Lin, K. Xie, R. Sui, D. Mu, R. Cao, J. Chang, F. Qiu, *Advances in Colloid and Interface Science* **2022**, *305*, 102698.

[227] Z. Liu, J.Z. Wen, *Chemical Engineering Journal Advances* **2022**, *11*, 100322.

[228] X. Wu, Y. Li, M. Huang, W. Liu, Z. Hou, *Materials Chemistry and Physics* **2016**, *182*, 125.

[229] Z. Yan, S. Shi, Y. Li, J. Chen, S. Maqbool, *Physical Chemistry Chemical Physics* **2020**, *22(6)*, 3611.

[230] G. Zhang, Q. Wang, L.T. Sha, Y.J. Li, D. Wang, S.Q. Shi, *Acta Physica Sinica* **2020**, *69(22)*.

[231] K. Wang, Y. Wang, P. Wei, Y. Lu, J. Zhang, Z. Chen, *Rare Metal Materials and Engineering* **2019**, *48(11)*, 3770.

[232] A.G. Khachaturyan, *Theory of structural transformations in solids*, Courier Corporation, **2013**.

[233] I. Goodfellow, Y. Bengio, A. Courville, *Deep learning*, MIT press, **2016**.

[234] J. Zhang, W. Yang, Y. Li, *Advances in Mechanics* **2021**, *51(4)*, 865.

[235] G.D. Gautam, D.R. Mishra, *Composites Part B: Engineering* **2019**, *176*, 107340.

[236] F. Faber, A. Lindmaa, O.A. von Lilienfeld, R. Armiento, *International Journal of Quantum Chemistry* **2015**, *115(16)*, 1094.

[237] K.T. Schuett, H. Glawe, F. Brockherde, A. Sanna, K.R. Mueller, E.K.U. Gross, *Physical Review B* **2014**, *89(20)*, 205118.

**Table of Contents**

This paper examines recent scientific advances and issues related to MMCs interfaces from four different perspectives: interfacial structural design, interfacial defect control, thermodynamics and kinetics of interfacial reactions, and interfacial microstructure-properties based on numerical simulation techniques. This paper provides some useful references for the future development of advanced metal matrix composites.

*Zheng Zhong[a,b], Xiaosong Jiang[a,b*], Hongliang Sun[a,b], Zixuan Wu[c], Liu Yang[d], Adriana Matamoros-Veloza[e*]*

**Recent Research on the Optimization of Interfacial Structure and Interfacial Interaction Mechanisms of Metal Matrix Composites: A Review**